

Investigating Line Defects in Molybdenum Disulphide Monolayers using Machine Learning



Helen Leung

Corpus Christi College

University of Oxford

A thesis submitted for the degree of

Materials Science, MEng Part II

Trinity 2021

Abstract

Monolayer molybdenum disulphide (MoS_2) is a promising candidate for next-generation electronic devices, which may lead to significant advances in a range of applications: notably batteries and photovoltaics. Defects in MoS_2 have a significant effect on its electronic properties and their behaviour is not yet sufficiently understood to support the use of MoS_2 in industrial applications. This project uses a convolutional neural network (CNN), a type of machine learning, to investigate the nature of line defect dynamics in monolayer MoS_2 from High Resolution Transmission Electron Microscopy (HRTEM) data.

Firstly, a model of MoS_2 was developed to generate simulated data, from which a CNN was trained to recognise defects. After experimental HRTEM data were applied to the CNN, a method to automate sequential analysis of defect behaviour in the output data was designed and implemented. Next, strain mapping was used to quantify atomic displacement around a line-defect. Finally, the effects of electron dose rate, accumulated electron dose, and defect density on defect growth were investigated.

This study shows that growth of line defects shorter than 60 nm is linear under constant electron irradiation and is linked to the sputtering rate of sulphur atoms. Any possible changes in behaviour past this length have not been investigated. It has also been demonstrated that the CNN can be used to extract a physical property, a strain tensor, from the data. In addition, the rate of electron irradiation is found to have no effect on sulphur vacancy generation above a specific dose rate, as long as accumulated dose is consistent. Finally, it is found that an increased defect density slows the rate of defect generation, likely due to the creation of pores and amorphous regions which disrupt the crystalline lattice.

Acknowledgements

I would like to thank:

Dr. Chen Huang for his invaluable guidance and for taking the time each week to discuss my progress. In particular, for his patience and support when things inevitably did not always go to plan.

Professor Angus Kirkland for welcoming me into his group. I benefited from his expertise and his advice was important for the direction of the project.

Mr. Kevin Treder for helping me to adapt to working remotely under the circumstances of the pandemic and for offering wider support.

Mr. Xiaonan Luo and Dr. Jun Chen for discussing the project findings with me.

My undergraduate tutors Professor Peter Nellist and Professor David Armstrong who have given me both academic and pastoral support. Thank you for believing in me over the years.

Finally, a huge thank you to my parents and to my friends for providing emotional support throughout this year.

Contents

List of Abbreviations	ix
1 Introduction	1
1.1 Project Overview	2
1.2 Project Aims	3
1.3 Project Objectives	3
2 Engineering Context	4
2.1 MoS ₂ in Batteries	5
2.2 MoS ₂ in Photovoltaics	6
2.3 Implications of Project Findings	8
3 Literature Review	9
3.1 Monolayer Molybdenum Disulphide	10
3.1.1 Mechanisms for Electron Irradiation Damage	11
3.1.2 Fundamental Electron Irradiation Defects Found in MoS ₂ . .	12
3.2 High Resolution Transmission Electron Microscopy (HRTEM) . . .	15
3.2.1 HRTEM Image Simulation	17
3.3 Processing HRTEM Datasets with Machine Learning	19
3.3.1 Machine Learning	19
3.3.2 Neural Networks (NNs)	19
3.3.3 Convolutional Neural Networks (CNNs)	19
3.3.4 Machine Learning in the Context of Electron Microscopy . .	21

4	Methods	23
4.1	Experimental Methods	25
4.2	Computational Methods	27
4.2.1	Generating a Defective Model	27
4.2.2	Generating a Synthetic Dataset	30
4.2.3	Training the Convolutional Neural Network	32
4.2.4	Applying the Convolutional Neural Network to Experimental Data	34
4.3	Post-prediction Data Analysis	37
4.3.1	Line Defect Tracking in Dataset A	37
4.3.2	Vacancy Tracking in Dataset B	41
5	Results	43
5.1	Line Defect Growth Rate	44
5.1.1	Sputtering Cross Section for Sulphur in MoS ₂	47
5.2	Observing Strain around a Defect	48
5.3	Effect of Dose and Defect Density on Rate of Vacancy Production .	52
5.3.1	Cumulative Dose vs Dose Rate Dependence	53
5.3.2	Effect of Cumulative Dose	55
5.3.3	Defect Density Dependence	56
5.4	Managing and Mitigating Errors	56
5.4.1	Accuracy of MULTEM Simulations	57
5.4.2	Accuracy of the Convolutional Neural Network	57
6	Discussion	60
6.1	Lengthening of Line Defects	61
6.2	Widening of Line Defects	62
6.3	Sputtering Cross Section for Sulphur in MoS ₂	63
6.4	Observing Strain	64

6.5	Inversion Domain Detection	65
6.6	Interaction of Line Defects with Pores	68
6.6.1	Digestion of Line Defect by Pore	68
6.6.2	Forming MoS Wires at Pore Edges	70
6.6.3	Molybdenum Clusters at Pore Edges	72
6.7	Effect of Dose and Dose Rate	73
6.8	Effect of Defect Density	73
6.9	Novelty of Method	76
6.10	Limitations	77
6.11	Summary	77
7	Future Work	78
8	Conclusion	80
9	Ethics and Sustainability	81
9.1	The Benefits of Using MoS ₂	82
9.2	Industrial Production of MoS ₂	82
9.3	Sustainability of MoS ₂ -based Solar Cells	83
9.4	Project Specific Considerations	84
10	Project Management	86
10.1	Initial Objectives and Subsequent Modifications	87
10.2	Resource Management	89
10.3	Assessing and Mitigating Project Risks	91
10.4	Conclusion	92
11	Health, Safety and Risk Assessment	102
Appendices		

A	Appendix	105
A.1	Creating Model $X_{\text{defective}}$	105
A.2	Applying the Convolutional Neural Network to Experimental Data .	106
B	Appendix	107
B.1	Calibrating HRTEM images	107
B.2	Calculating Dose Rate in Dataset A	108
B.3	Calculating the Number of Sulphur Atoms per \AA^2	109
B.4	Statistical Tests	110
B.4.1	Grubs Tests	110
B.4.2	χ^2 Test	111
	Bibliography	112

List of Abbreviations

AC-TEM	. . .	Aberration Corrected Transmission Electron Microscopy
ADF-STEM	.	Annular Dark Field Scanning Transmission Electron Microscopy
AI	Artificial Intelligence
BCC	Body-Centered Cubic
CNN	Convolutional Neural Network
COP21	21st Conference of the Parties (Paris Climate Conference)
CPU	Computer Processing Unit
CTF	Contrast Transfer Function
CVD	Chemical Vapour Deposition
DFT	Density Functional Theory
EELS	Electron Energy Loss Spectroscopy
EM	Electron Microscopy
ePSIC	Electron Physical Sciences Imaging Centre
EV	Electric Vehicle
FCC	Face-Centered Cubic
GPA	Geometric Phase Analysis
GPU	Graphics Processing Unit
GUI	Graphical User Interface
HRTEM	. . .	High Resolution Transmission Electron Microscopy

ID	Inversion Domain
LNG	Liquid Natural Gas
LUT	Look Up Table
MD	Molecular Dynamics
NN	Neural Network
PCE	Power Conversion Efficiency
ReLU	Rectified Linear Unit
SEM	Scanning Electron Microscopy
SNR	Signal to Noise Ratio
STEM	Scanning Transmission Electron Microscopy
SVL	Sulphur Vacancy Line
TMD	Transition Metal Dichalcogenide
VAT	Value Added Tax

1

Introduction

Contents

1.1	Project Overview	2
1.2	Project Aims	3
1.3	Project Objectives	3

1.1 Project Overview

The ongoing climate emergency is widely accepted as one of the largest threats to humanity. As a result, there is an increasing urgency for the rapid development of new technologies to facilitate the shift to renewable, clean energy. The desirable electronic properties of monolayer Molybdenum Disulphide (MoS_2) have stimulated interest in it as a functional material for a range of electronic applications, such as in batteries and photovoltaics. Defects are local areas of the material where the pristine crystal structure is disrupted. Their presence has a large effect on the electronic properties of MoS_2 . The nature of defect behaviour in MoS_2 is not well understood, hindering its potential for industrial use. This project aims to enhance understanding of defect behaviour in monolayer MoS_2 .

Electron Microscopy (EM) is a technique used to characterise MoS_2 at the atomic scale enabling the visualisation of defects. It is also used to stimulate defect generation via electron irradiation: a useful way to investigate defect dynamics which is often used as a proxy for extreme environments. The advances in high-speed pixelated detectors have enabled the capture of movies at record time resolutions [1, 2]. However, this generates vast quantities of data (up to 400 Gbs^{-1} [3]) which could not feasibly be analysed by hand. A degree of automation is therefore necessary. Machine learning is a promising tool for facilitating this analysis by compressing large volumes of data into quantifiable scientific insight.

In the literature, there are many purely theoretical investigations into the nature of defect dynamics in MoS_2 which involve Density Functional Theory (DFT) and Molecular Dynamics (MD). This project takes an alternative route and instead makes use of a combination of experimental and computational techniques: namely High Resolution Transmission Electron Microscopy (HRTEM) and Neural Networks (NNs) respectively. The use of a NN helps produce quantitative sequential analysis of time series data.

1.2 Project Aims

The most common defect found in monolayer MoS₂ is a sulphur vacancy. These individual vacancies can agglomerate to form line defects [4], which are the main focus of investigation in this project. Line defect growth was recorded using HRTEM and processed using a NN. Specific topics of interest were:

1. The dependence of line defect growth on the length and width of the specific defect.
2. The dependence of line defect growth on electron dose rate.
3. The effect of the defect density on further defect generation.

1.3 Project Objectives

In order to achieve the aims set out above, the following objectives were set:

1. Train and apply a NN to recognise defective MoS₂ lattices building on methods established by the previous Part II student.
2. Improve the quality of simulated training data by refining a model of defective MoS₂ and then retrain the NN.
3. Create a post-prediction method to extract quantitative information about line defect behaviour from the NN outputs.
4. Create a meaningful way to measure the accuracy and performance of the NN.

2

Engineering Context

Contents

2.1	MoS₂ in Batteries	5
2.2	MoS₂ in Photovoltaics	6
2.3	Implications of Project Findings	8

This chapter gives a broader context for the engineering applications and the need for the research carried out in this project.

197 countries around the globe have committed to limiting global warming to below 2°C in a landmark agreement at COP21 in 2015 [5], which requires wide-spread decarbonisation of energy production. New technologies are crucial to facilitate this goal. MoS₂ is a material of great interest for a range of electronic devices used in the energy industry. This section focusses on two specific engineering applications of MoS₂: batteries and photovoltaics.

2.1 MoS₂ in Batteries

Batteries are crucial to facilitate the transition to clean energy. Renewable energy sources such as wind and solar power are less reliable than coal and liquified natural gas (LNG). In order to maintain a stable grid based on renewables, energy storage technology is crucial. Energy produced in times of excess supply needs to be stored for later use in times of high demand [6]. Battery storage technology is a versatile and efficient way of storing and discharging this energy. Advances in battery technology have been further facilitated by the rise in demand for electric vehicles (EVs), which is driven by government policies and lowered costs. For example, the UK government will ban the sale of petrol or diesel cars from 2030 and EVs are exempt from VAT and road tax in Norway [7]. Longer battery life and faster charging times are crucial developments required of battery technology to keep up with these increasing demands.

Defect-free MoS₂ is a promising candidate for the electrode material in batteries for several reasons. The two-dimensional nature of MoS₂ enhances the electrochemical performance of the conversion reaction in lithium-ion batteries by increasing electrode-electrolyte contact area. In addition, MoS₂ can increase battery lifetimes.

Crack formation currently compromises the mechanical integrity of batteries which severely limits their time in operation [8]. Using MoS₂ increases mechanical stability because there is a smaller volume expansion across the charge/recharge cycle [9] and it is a soft material (with Mohs hardness between 1-2) [10]. MoS₂ also has a high theoretical energy density of 670 mAhg⁻¹: a value 1.8 times larger than graphite, which is a material commonly used in electrodes [11]. This gives the potential for lighter batteries.

2.2 MoS₂ in Photovoltaics

Solar power is projected to be the fastest growing energy source in the world, growing in use from 11% to 48% by 2050 in the U.S. alone [12]. It is the largest exploitable energy resource as shown in Figure 2.1. Even with a low power conversion efficiency (PCE), the potential for solar energy outstrips other sources. However, commercially used solar panels are rigid, heavy, non-transparent devices which restricts their applications. Any potential for solar cells which are lighter, more flexible, or more efficient would increase their feasibility for widespread use.

Defect-free MoS₂ has desirable intrinsic properties which make it a promising candidate to help improve these aspects of photovoltaics. Single layer MoS₂ has a low electron mobility [14] and behaves as an n-type semiconductor. It has a direct band gap of 1.9 eV [15] which gives it the potential for high efficiency electron-hole pair generation. A monolayer of MoS₂ can absorb as much sunlight as a 50 nm thick layer of silicon, with a 1 nm layer of MoS₂ absorbing 5-10% of incident sunlight [16]. This behaviour is superior to GaAs and Si (as shown in Figure 2.2) and would allow for thinner, lighter solar cells. Although the industrial manufacture of defect-free monolayer MoS₂ is a challenge, their integration into current Si devices for enhanced efficiency is promising. Tsai *et al.* [17] created a heterojunction solar cell with p-type silicon and monolayer MoS₂, which achieved a PCE of 5.23%: the highest achieved from existing solar cells based on monolayer transition-metal dichalcogenides. The

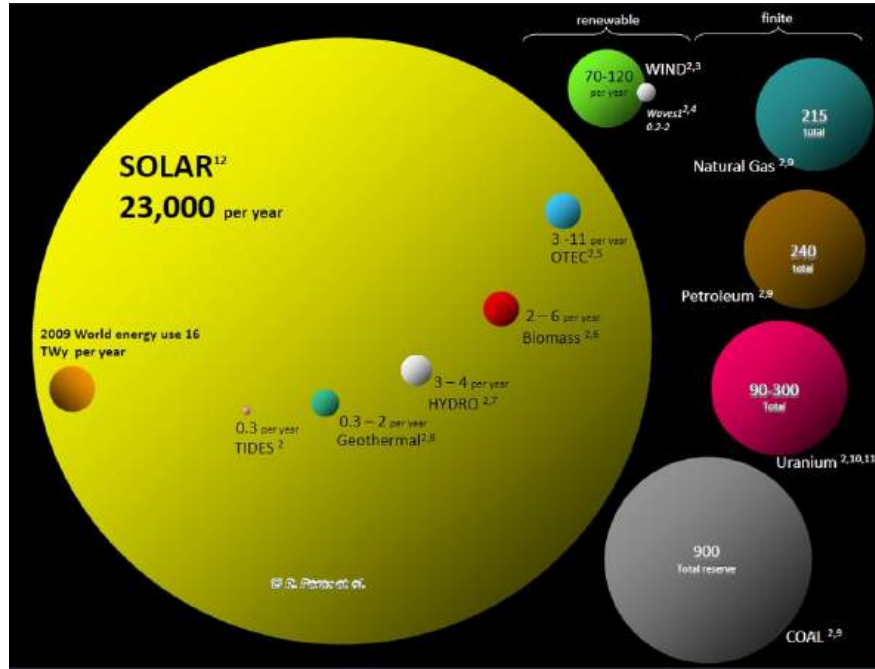


Figure 2.1: The sun has the largest potential as an energy reserve compared to other sources of energy. [13]

versatility of MoS₂ is further demonstrated by its use in pervoskite solar-cells, in which a PCE of 13.1% was achieved [18]. Furthermore, MoS₂ has excellent mechanical flexibility with a minimum bending radius of 0.74 mm [19], making it promising for use in flexible solar panels.

material	thickness	efficiency	weight (g/m ²)	power density (kW/L)
GaAs	1 μ m	\sim 29% ³⁸	5.3	290
Si	35 μ m	20.6% ³⁹	92.7	5.9
graphene/MoS ₂	0.9 nm	0.1–1.0%	3.9×10^{-3}	1000–10 000
WS ₂ /MoS ₂	1.2 nm	0.4–1.5%	7.9×10^{-3}	3000–12 000

Thickness and weight refer solely to the device active layer. Efficiency is the PCE under AM1.5G illumination.

Figure 2.2: The power density of MoS₂-based devices is up to 2000 times larger than silicon [16] under AM1.5G illumination: a standard used to ensure consistency of light intensity.

2.3 Implications of Project Findings

Defects have a significant effect on the electronic behaviour of MoS₂. For example, line defects are local channels of metallic material in the semiconducting 2H phase, whilst the metastable 1T phase is also metallic. This topic is further explored in the Literature Review (Section 3.1). Given the importance of defects on the electronic performance of MoS₂, advancing understanding of the mechanisms behind their behaviour is vital to increase the viability of defect-free industrial production of MoS₂. A well-developed understanding may also allow for manipulation of defects to perform band gap engineering in nano-electronic devices.

Apart from the engineering applications of MoS₂, this project leverages advances in machine learning capabilities to perform time and labour intensive data analysis. The implementation of this might encourage the wider adoption of artificial intelligence in scientific research.

3

Literature Review

Contents

3.1	Monolayer Molybdenum Disulphide	10
3.2	High Resolution Transmission Electron Microscopy (HRTEM)	15
3.3	Processing HRTEM Datasets with Machine Learning	19

This chapter provides a summary of the three topics which are relevant to this project; MoS₂, HRTEM, and machine learning.

3.1 Monolayer Molybdenum Disulphide

MoS₂ belongs to a class of materials called transition-metal dichalcogenides (TMDs), which have the common structural formula MeX₂ where M is a transition metal, and X is a chalcogen atom [20]. Monolayer MoS₂ is considered a nanomaterial and consists of two atomic layers of close-packed sulphur atoms separated by one close-packed molybdenum atomic layer [21]. MoS₂ has several phases. Its most stable form is the 2H phase, where sulphur atoms in the unit cell form a basic hexagonal lattice (as in Figure 3.1) [22].

Defects in MoS₂ affect its electronic properties [25]. The presence of sulphur vacancies introduces unpaired electrons into the lattice and creates a mid-gap energy level near the conductive band edge, causing the material to behave as an n-doped semiconductor [26]. As demonstrated by Tongay *et al.* [27], changes to defects in MoS₂ can lead to order of magnitude changes in the light absorption and electrocatalytic behaviour of the material. A study by Hong *et al.* [28] of antisites and vacancies showed that minimising point defects in the structure was crucial when using MoS₂ for electronic applications. Its photoluminescence quantum yield of 0.4% can be dramatically increased to over 95% by the removal of defects, which are responsible for sites of non-radiative recombination [29].

There are several mechanisms by which defects can be introduced into MoS₂, such as annealing [30], plasma treatment, ion irradiation, and electron irradiation. Similarly to graphene, electron irradiation allows for a high level of control over the type and number of defects formed [31, 32] and is the predominant damaging mechanism of MoS₂ when it is being imaged using electron microscopy (EM).

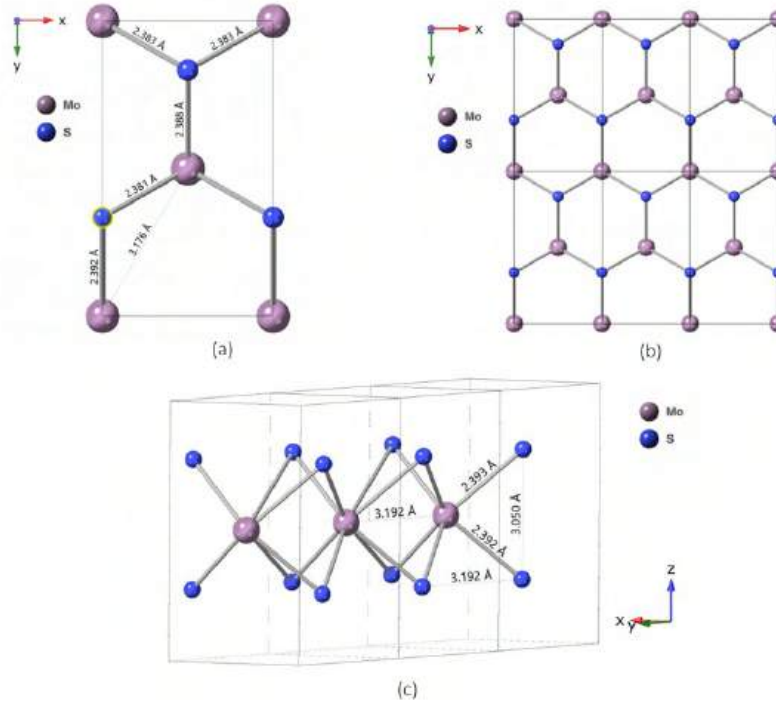


Figure 3.1: The atomic structure of 2H MoS₂ [23]. Diagram adapted from *Lear 2020* [24].

3.1.1 Mechanisms for Electron Irradiation Damage

The atomic structure of MoS₂ can be characterised using EM. During imaging, energetic electrons passing through the specimen can produce defects by displacing atoms from the sample. Beam damage is one of the main causes of the defects studied in MoS₂. It typically occurs via three mechanisms [33]:

1. Radiolysis: when inelastic electron scattering breaks the chemical bonds of the material.
2. Sputtering: when an atom is ejected from the specimen surface, creating point defects (shown in Figure 3.2).
3. Heating: an increase in local temperature due to inelastic scattering may result in defect creation [34].

There are several factors influencing the extent of damage caused by irradiation. Egerton *et al.* [35] found that damage should be proportional to accumulated

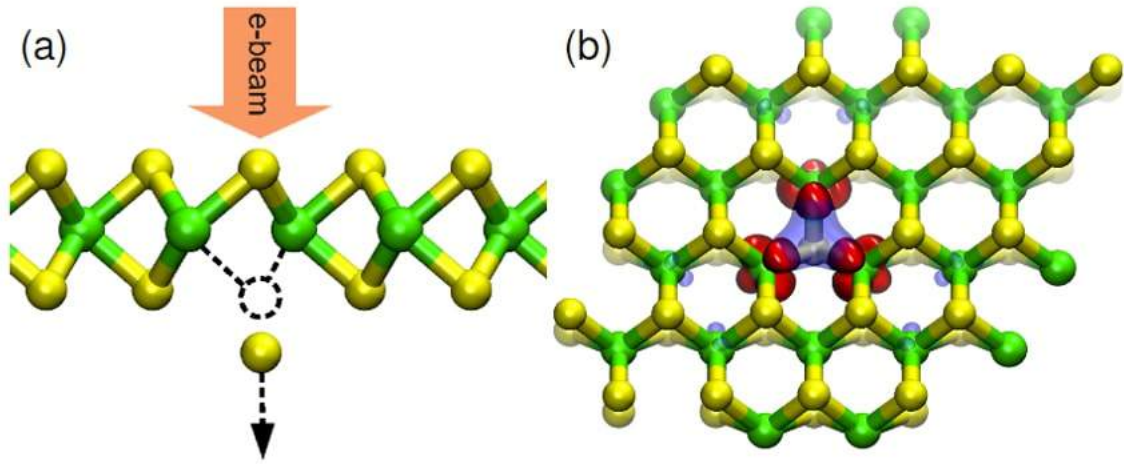


Figure 3.2: (a) Sputtering event leaving behind a vacancy. The bottom layer sulphur atom is always removed first. (b) Birds eye view of lattice: yellow atoms are sulphur, green atoms are molybdenum. Adapted from Komsa *et al.* [20].

radiation dose. In addition, Robertson *et al.* [32] found ways to control defect creation by making use of a threshold electron dose rate.

3.1.2 Fundamental Electron Irradiation Defects Found in MoS₂

Below are a list of the main irradiation defects in MoS₂ that have been observed in previous studies.

1. **Sulphur vacancies** are intrinsic defects [36] and can be seen in Figure 3.3. In an ideal MoS₂ layer, each sulphur atom has two valence electrons that bind to two molybdenum electrons [37]. Double sulphur vacancies are where the top and bottom sulphur atoms in the same atomic column are removed: the bottom atom is always removed first in a sputtering event [20].
2. **Line Defects:** Individual sulphur vacancies are likely to directionally agglomerate via diffusion to form extended line defects (shown in Figure 3.4) [4]. Chen *et al.* [38] found that 60 nm long sulphur vacancy line defects (SVLs) initiated pore formation at high vacancy densities. The strain field around the

line defect (shown in Figure 3.5) acts as a sink for vacancies, which encourages line defect lengthening. Prolonged beam exposure results in the widening of line defects [4]. These multi-line defects become increasingly metallic as their width increases (as in Figure 3.6).

3. **Inversion Domains** are a type of intrinsic defect and are where the layer changes its direction through a line defect [25]. Line defects grow to eventually form these regions [39]. These boundaries act as metallic channels inside the monolayer, which affects exciton behaviour [21].

Not much experimental data of typical defect concentrations exists. This is because defects in low-dimensional systems are so unstable that they are hard to measure [40]. Long exposure times in EM are required for data with low noise, which often fails to capture rapid changes in defect movement.

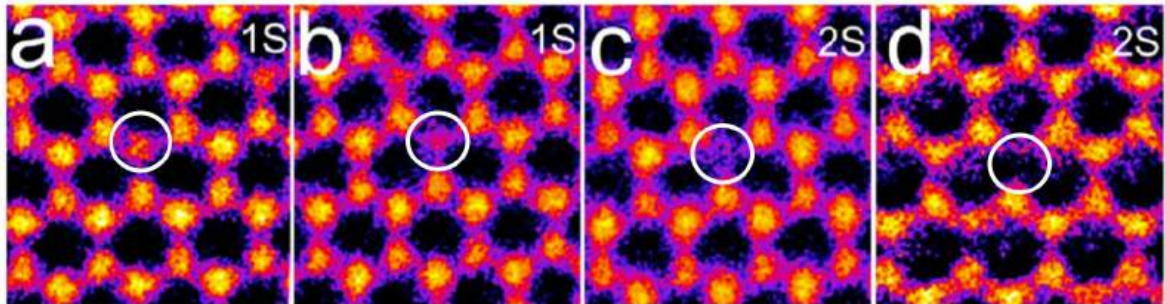


Figure 3.3: AC-TEM images of single (a)-(b) and double (c)-(d) sulphur vacancies. Adapted from Wang *et al.* [41].

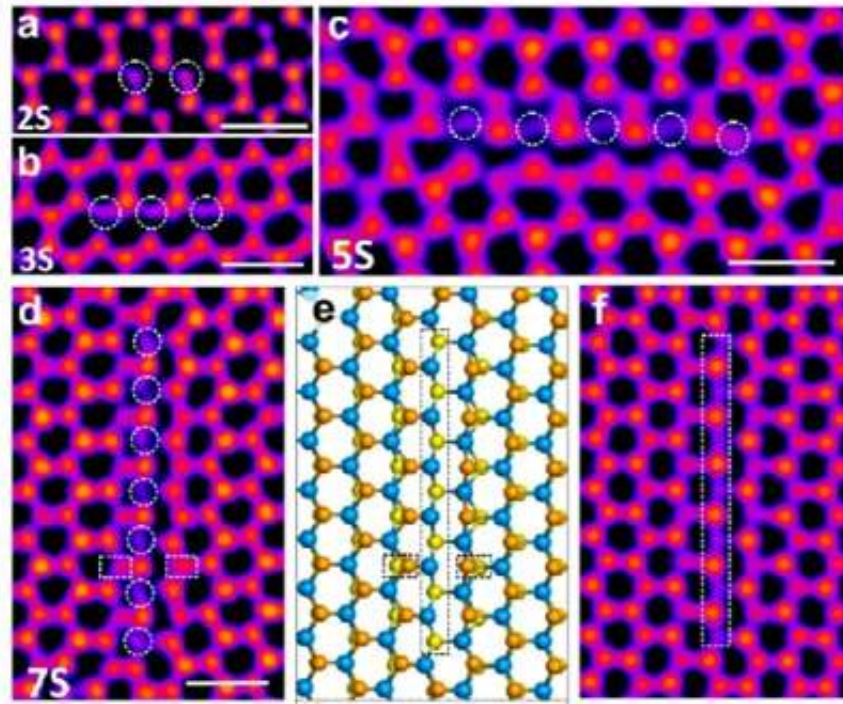


Figure 3.4: AC-TEM images taken by Wang *et al.* demonstrating how single sulphur vacancies may agglomerate to form line defects. (a), (b), (c) show SVLs of 2, 3, and 5 sulphur vacancies in length. (d) is the experimental image on which (e), an atomic model, is based. (f) is a simulated image based on the atomic model in (e) [41].

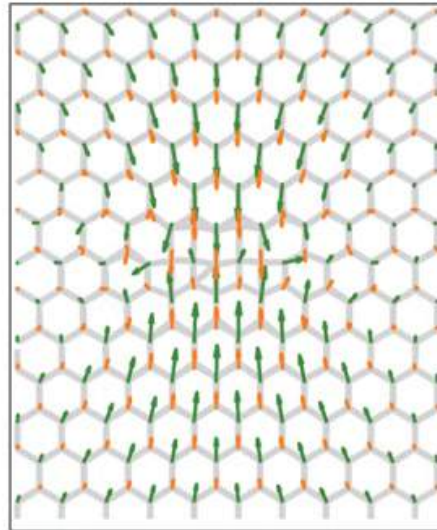


Figure 3.5: Strain around a line defect is anisotropic. SV and DV represent single and double vacancies respectively [4].

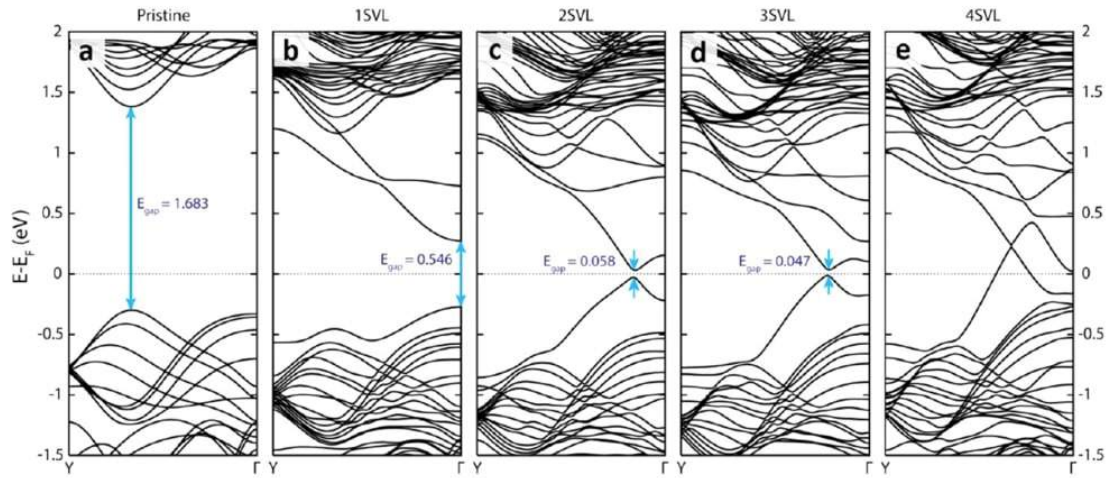


Figure 3.6: DFT calculations showing a decreasing band gap as the width of the line defect increases. Band diagrams from Wang *et al.* [41].

3.2 High Resolution Transmission Electron Microscopy (HRTEM)

HRTEM is a tool used to characterise atomic-scale defects accurately [42] and has been developed from the initial transmission electron microscope (TEM) developed by Ruska and Knoll in 1932 [43]. In this technique, highly concentrated magnetic fields are used as lenses to control the trajectory of electrons which are fired at the sample. Electron energies range from 30 keV to 1 MeV. The sample must be thin (tens of nm) in order to prevent the effects of multiple electron scattering becoming obstructive to the resolution of fine atomic detail [42].

Image Formation

The TEM forms an image by firing electrons at a sample (shown in Figure 3.7). This incoming electron beam interacts with the atoms in the sample by elastic and inelastic scattering [42]. Images in HRTEM are formed via phase contrast [45] and use information from both transmitted and elastically scattered waves which interfere. A diffraction pattern is formed in the back focal plane of the objective

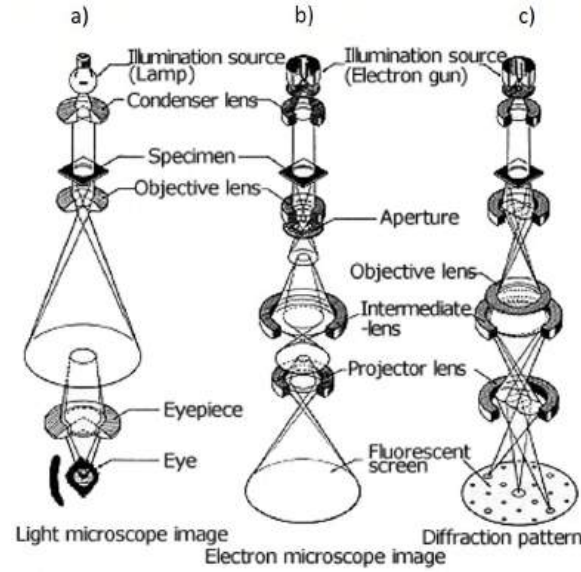


Figure 3.7: Schematic showing the similarity of a TEM to an optical microscope: TEM imaging mode is shown in diagram (b). Adapted from JEOL 200fx handbook [44].

lens, and an image is formed in the image plane [46]. At the image plane, the exit-surface wavefunction may be measured. This describes the information carried by the transmitted electron beam [42].

In the case of a thin specimen, the weak phase object approximation can be applied. In this approximation, absorption effects and Fresnel diffraction within the specimen are neglected [46] and it is assumed that the amplitude of the transmitted wave function is linearly related to its projected potential [33]. The effect of the objective lens on image formation is described by the phase contrast transfer function (CTF) [42].

The CTF is key to interpreting HRTEM images and describes the unique relation between the input and output signals [33], neglecting the effects of noise. The CTF can be deduced via empirical methods by observing the specimen and image. It is also used in HRTEM image simulation.

Limits to Resolution

For any optical system the wavelength of the radiation used is the ultimate resolution limit as expressed by Abbe's equation [46]:

$$r_d = \frac{k\lambda}{n(\sin \alpha)}, \quad (3.1)$$

where $0.6 < k < 0.8$, dependent on the coherence of the illumination, λ is the wavelength, n is the refractive index, α is the aperture angle of the objective lens, and r_d is the resolution. In 1936, Scherzer demonstrated that electron lenses always have chromatic and spherical aberrations which limit the resolution [47]. Other types of aberrations include defocus, coma, and astigmatism all of which can be introduced as terms in the CTF. For example, the phase CTF function due to defocus and spherical aberration is given by:

$$\sin W(\mathbf{k}) = \sin \left(\pi C_1 |\mathbf{k}|^2 + \frac{\pi}{2} C_3 \lambda^3 |\mathbf{k}|^4 \right), \quad (3.2)$$

where W is the wave aberration function, \mathbf{k} is the wavevector, C_1 and C_3 are aberration coefficients, and λ is the wavelength [46].

3.2.1 HRTEM Image Simulation

Despite being able to achieve up to 0.5 Å resolution [48], image interpretation in HRTEM is a challenge. This is because images are formed via phase contrast which makes them very sensitive to changes in parameters such as defocus. To tackle this difficulty, a simulated image is formed by assuming a structure and using numerical computations derived from first principles [22], such as the multislice method, which is discussed below. The simulated image is compared with the experimental image, and is modified until the simulated trial images and experimental images match closely [49].

MULTEM: a multislice method for HRTEM image simulation

In 1977, Ishizuka and Ueyda [50] introduced a numerical approach to the multislice method which was originally proposed by Moodie and Cowley [51, 52]. This method models the electron-specimen interaction by dividing the specimen into many thin slices (as shown in Figure 3.8) which obey the weak phase object approximation. The exit-surface wave function is recreated to form the simulated image. Advances in computing allowed Lobato and Van Dyck to implement the method in a parallel computing system in 2015 [53]. Their programme, called MULTEM, allows for use of the CTF to include the microscope's effects, such as that of lens aberrations and defocus [54].

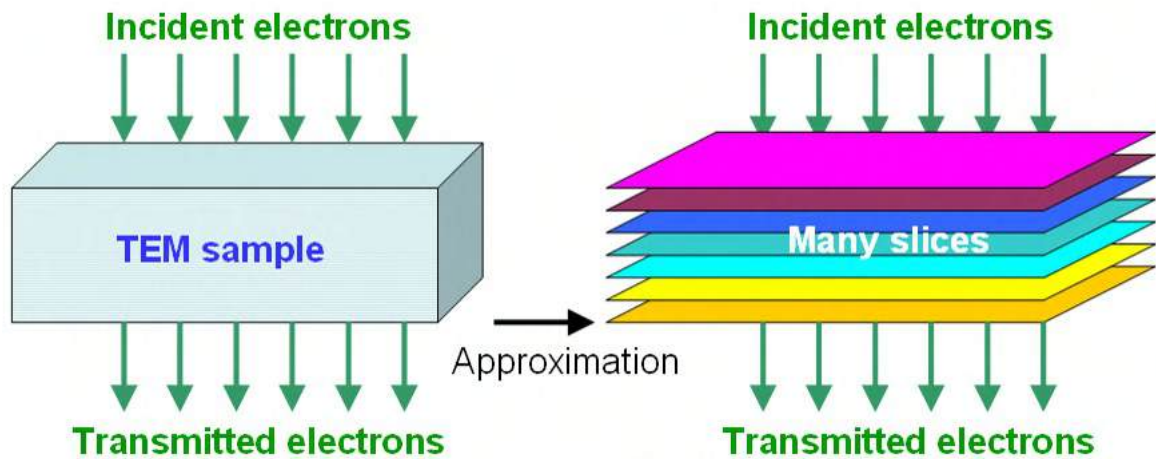


Figure 3.8: Diagram illustrating the multislice approximation from [55].

3.3 Processing HRTEM Datasets with Machine Learning

The increasing amount of data obtainable via EM demands a degree of automation during analysis for which machine learning is an ideal method.

3.3.1 Machine Learning

Machine learning is a powerful technique because it avoids any hard-coding of rules and is able to predict trends and patterns from raw data. There are two main categories of machine learning algorithms: supervised and unsupervised learning, depending on what type of experience is allowed during the learning process [56]. In supervised learning, some input-output pairing is provided to build and refine the model [57].

3.3.2 Neural Networks (NNs)

Neural networks are a technique used in deep learning which is a type of machine learning. Neural networks imitate the human brain [58]. Layers of neurons are connected [57] and each neuron collects the weighted sum of incoming signals before using an activation function to calculate the strength of the signal it will pass on [58]. The most commonly used activation function is the leaky ReLU (rectified linear unit).

3.3.3 Convolutional Neural Networks (CNNs)

A convolutional neural network (CNN) is a type of neural network specifically designed to infer predictions from data with ‘a grid-like topology’ [56], such as images. Convolution is an operation which can detect features of an image. It is used because it is an integral transformation which does not change the spatial association between pixels [59].

In CNNs, neurons are organised into three dimensions [60]. There are two major stages of the network:

- **Feature Extraction:** a series of convolutions and pooling operations take place in order to detect the features of the image.
- **Classification:** in these layers, a probability is assigned to the object on the image [61].

Layers of a CNN

Layers are an important aspect of CNNs. Simonyan *et al.* [62] demonstrated the importance of depth, defined by the number of layers applied, in a network model to achieve a greater classification accuracy. Krizhevsky *et al.* [63] observed that the removal of one layer significantly degraded the performance of their CNN.

Three main types of layers make up the structure of a convolutional network; convolutional layers, pooling layers, and a fully-connected layer. **Convolutional layers** compute the output of the neurons which are connected to local regions in the input volume [60]. An activation function is applied in each convolutional layer [64]. **Pooling layers** reduce both the image dimensions and noise [60, 59, 61]. The **fully-connected layer** computes the scores. A CNN applies these layers to the original image repeatedly until each pixel of the image is labelled with a value for classification [60].

The universal approximation theorem proposed by Hornik and Stinchcombe states that it is possible to create a network able to achieve any desired accuracy if it is large enough [66]. However, there is an inevitable trade-off between accuracy and resources [56].

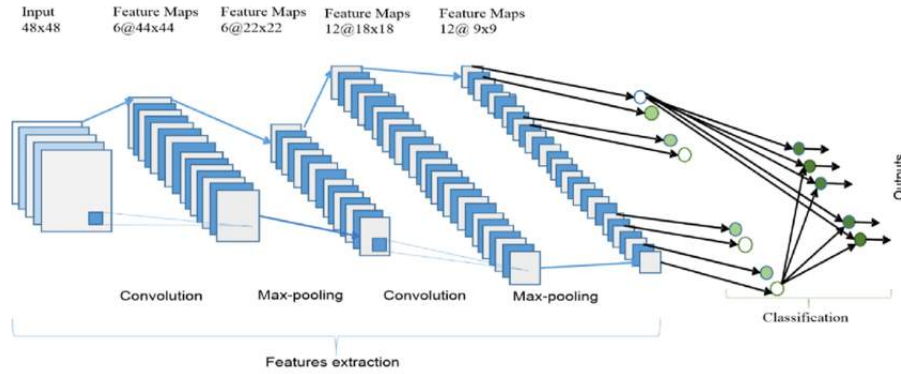


Figure 3.9: The overall architecture of a Convolutional Neural Network [65].

3.3.4 Machine Learning in the Context of Electron Microscopy

Analysis of EM data normally relies on inspection by experts [67]. In the field of EM there have been several attempts made at training CNNs for image analysis. The U-net is a popular CNN architecture which was made by Ronneberger in 2015 for the purpose of biomedical imaging [68]. This type of CNN has been a popular choice for previous studies in EM.

In 2018, Schiotz and Madsen [67] used a CNN to ‘identify chemical species and the height of atomic columns’ in scanning transmission electron microscopy (STEM) images. The CNN classified each image pixel as either a background atom, or an atomic column. Another CNN built by Modarres *et al.* [69] was shown to classify nanowires and fibres in scanning electron microscopy (SEM) images with an accuracy rate of 80%. In 2017, Ziatdinov *et al.* [70] used a CNN to understand how the chemical structure of a defect changed at each stage of a reaction with STEM data.

CNNs have only been used to process HRTEM images a handful of times. Saito *et al.* [71] built a CNN that distinguished between monolayer and bilayer flakes of MoS₂ with 70-80% accuracy. In 2021 Groschner *et al.* [72] used HRTEM images to

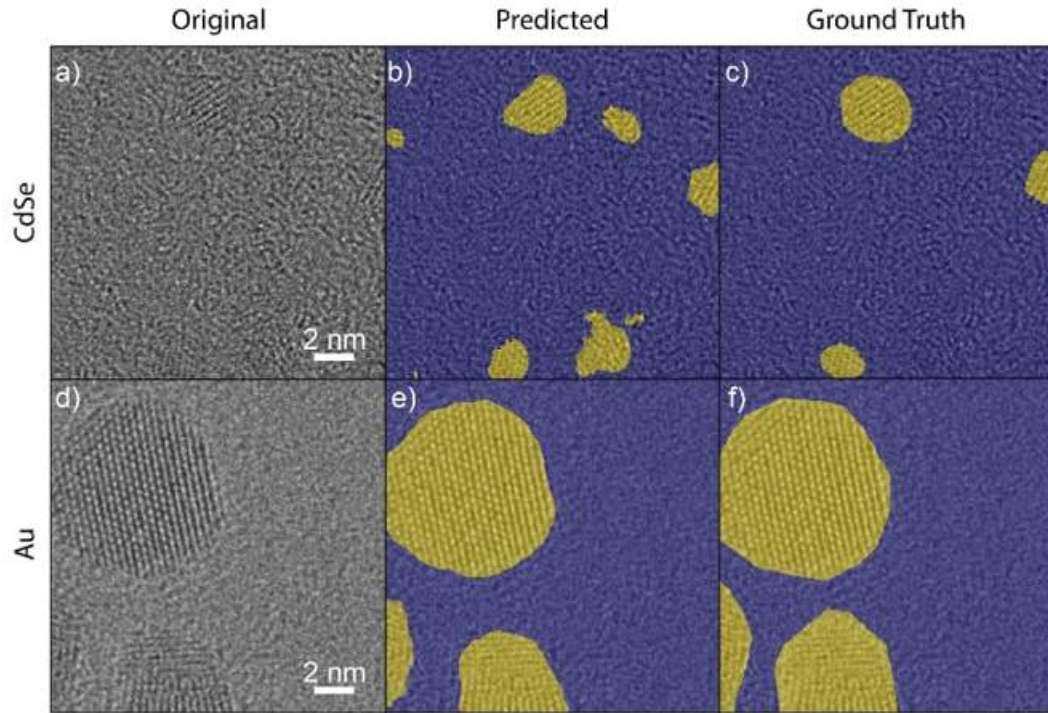


Figure 3.10: Performance of a segmentation network built by Groschner *et al.* to identify nanoparticles in HRTEM images which demonstrates a successful application of this network architecture in HRTEM. Notably, the hand labelled micrographs have been assumed to be the ground truths. Not all HRTEM images can be so confidently labelled. [72].

train a U-Net to spot nano-particles, which significantly out-performed traditional image segmentation techniques (Figure 3.10), and Zhu *et al.* used a CNN to automate lattice spacing measurements [73]. Only one attempt has been made to segment an image by individual atoms; Schiotz *et al.* [74] trained a CNN to identify atoms within nanoparticles in HRTEM images. Synthetic data was used to train this CNN rather than hand-labelled experimental data. However, barely any studies highlighted how HRTEM image classification outputs from the CNNs were further used to give any quantitative insights. This is a noticeable gap.

4

Methods

Contents

4.1	Experimental Methods	25
4.2	Computational Methods	27
4.3	Post-prediction Data Analysis	37

A set of largely untouched HRTEM data had been acquired before this project in March 2020 (referred to as **Dataset A**). In April 2021, further data acquisition (referred to as **Dataset B**) took place (data acquisition is described in Section 4.1). Methods developed to analyse Datasets A and B are described in Section 4.2 and 4.3.

Figure 4.1 shows a summary of the methodology described in this chapter.

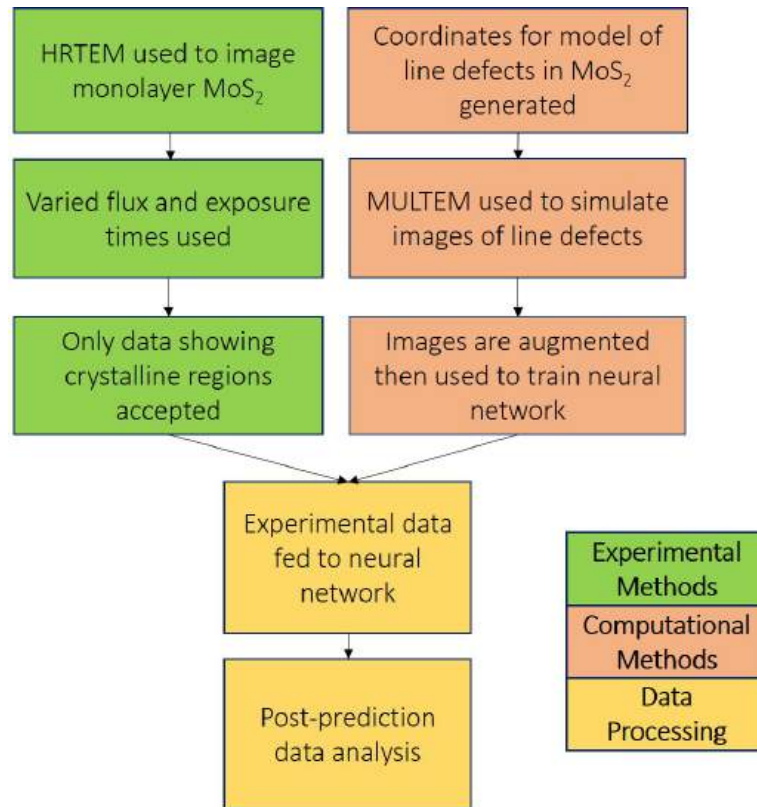
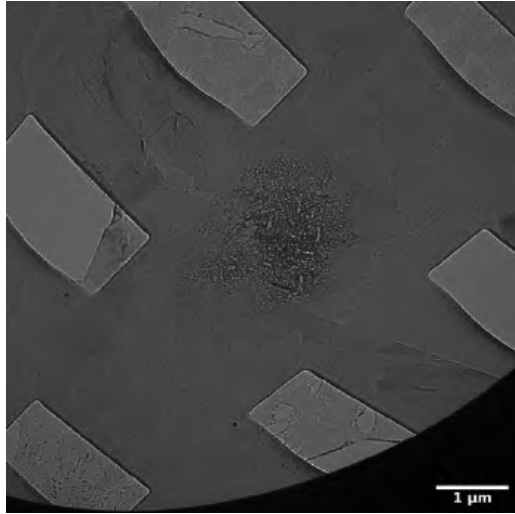


Figure 4.1: Diagram illustrating the overall workflow of the project described in this chapter.

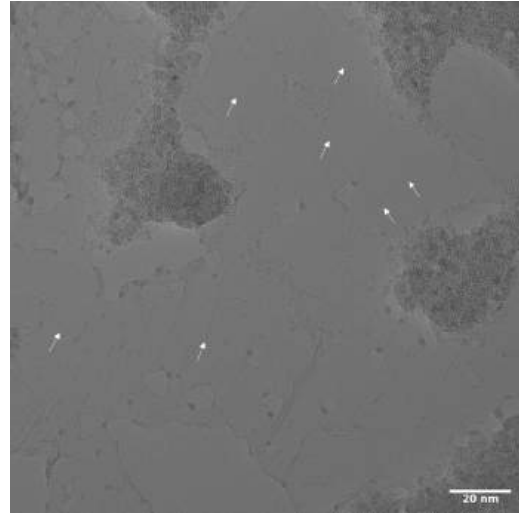
4.1 Experimental Methods

Dr. Chen Huang carried out the experimental methods described in this section. Collaboration on data acquisition was conducted remotely via Microsoft Teams.

The MoS_2 sample used had been synthesised via chemical vapour deposition (CVD) and mounted on a Si_3N_4 grid. In order to remove contamination from the sample's surface, it was mounted on a DENS heating chip and heated to 500°C in the imaging chamber. All data was collected using a JEM-ARM300F GRAND ARM Atomic Resolution Electron Microscope operating at 80 kV. A Gatan 4k x 4k detector was used to record the data. Acquisition times ranged between 0.1 s to 0.2 s. A large field of view was used to search the sample for potential monolayer regions.



(a) Rectangular holes in the Si_3N_4 grid are the location of MoS_2 areas of interest.



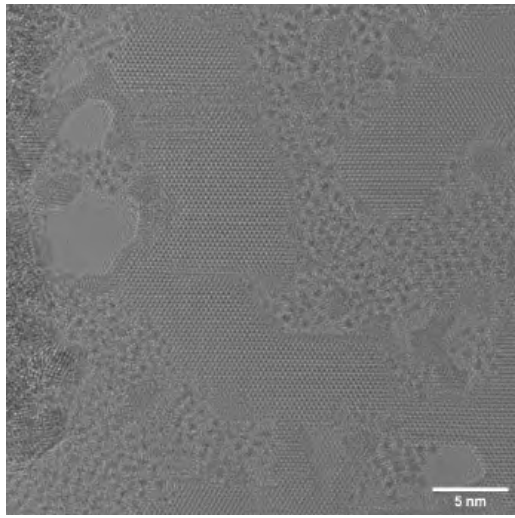
(b) Line defects are visible to the naked eye at this magnification and are labelled with white arrows.

Figure 4.2: A low magnification was used to spot potential monolayer areas on the sample.

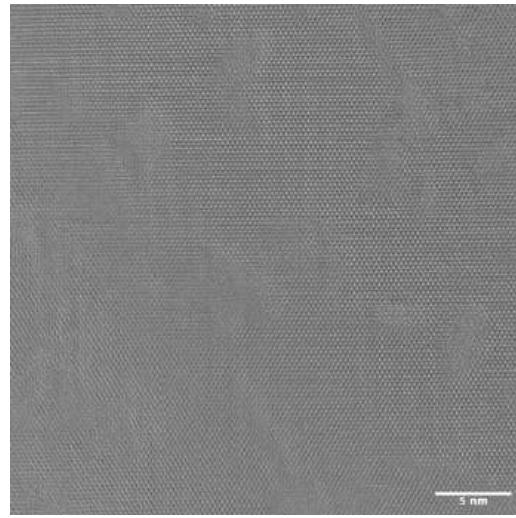
Both Datasets A and B were acquired using similar experimental methods. However, in order to introduce an investigation into the effects of dose and dose-rate on line defect growth in Dataset B, the flux for this dataset was varied between the range of $8539\text{--}56705\text{ electrons } \text{\AA}^{-2} \text{ s}^{-1}$. In total, 30000 frames were collected: over 2

Tb of data.

Due to the beam sensitivity of the material, limited time was spent on confirming that the most desirable areas were being imaged, so around 35% of collected data (some examples are shown in Figure 4.3) were discarded after acquisition.



(a) Unusable data: bilayer and surrounded by non-crystalline areas.



(b) Another bilayer region: identifiable due to the contour present in the contrast.

Figure 4.3: Bilayer regions were difficult to distinguish from monolayer regions until closer inspection. The presence of contouring and contrast indicates the presence of a bilayer region here.

4.2 Computational Methods

This section describes the image simulation and machine learning techniques developed to process experimental data collected in Section 4.1. An overview of this is shown in Figure 4.4.

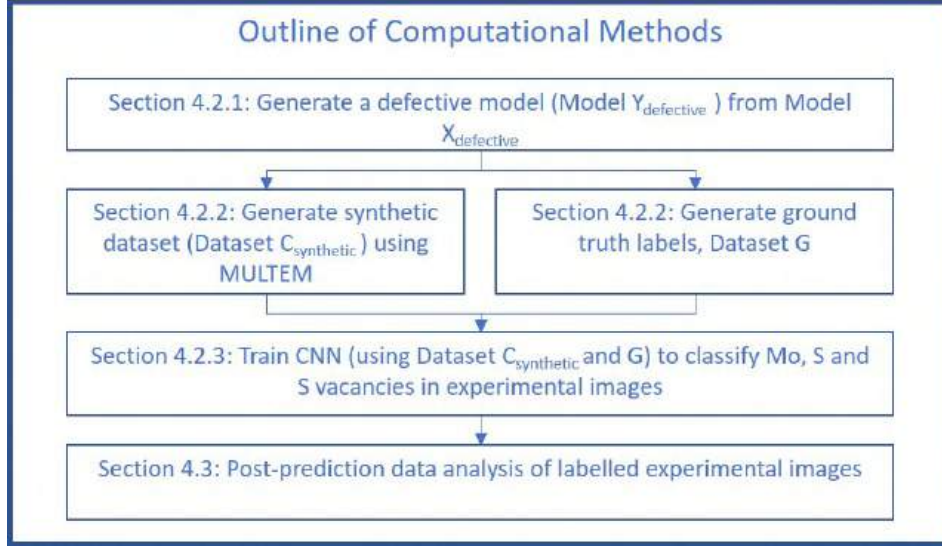


Figure 4.4: Overview of Computational Methods. Details of each step are shown in Figures 4.5, 4.7 and 4.8, 4.10, 4.15 respectively. Labelling of models and datasets are explained in each section.

4.2.1 Generating a Defective Model

A model of defective MoS_2 was used to form an array of atomic coordinates. These coordinates were then used to simulate electron micrographs for training of a CNN.

An initial model of MoS_2 (referred to as **Model $X_{\text{defective}}$**) from the previous Part II student [24] was improved to create a new model (referred to as **Model $Y_{\text{defective}}$**). Details of how Model $X_{\text{defective}}$ was created can be found in Appendix A. There were several types of defects in Model $X_{\text{defective}}$: single-width line defects some of which had kinks, and single sulphur vacancies.

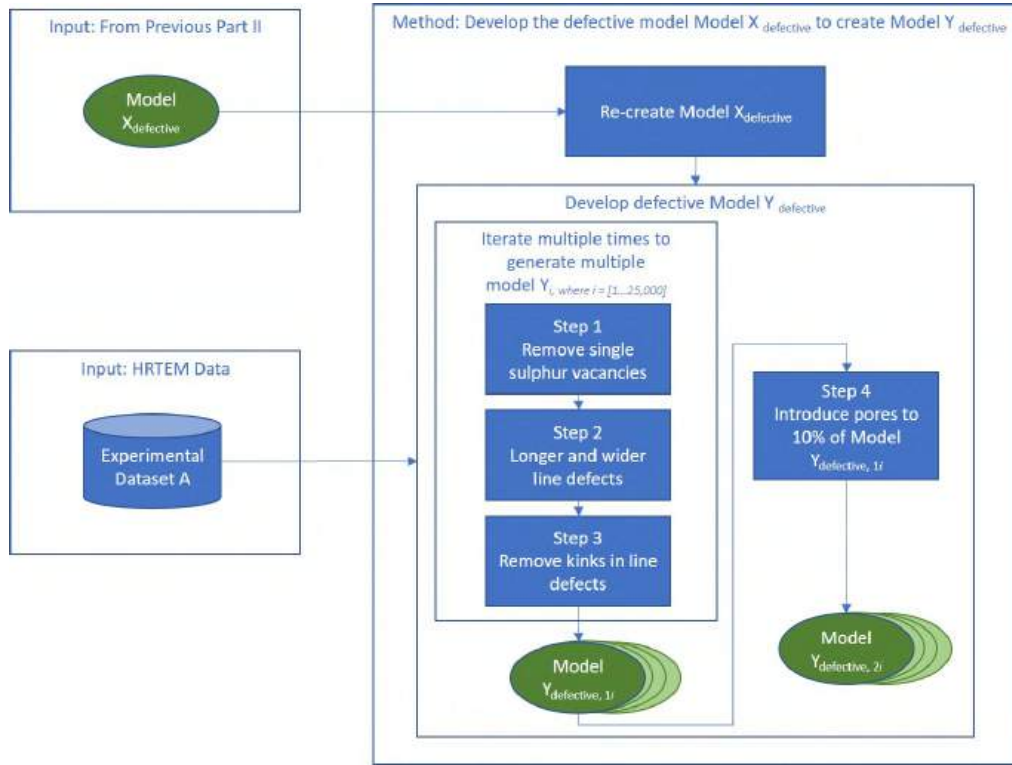


Figure 4.5: Firstly, Model $X_{\text{defective}}$ was improved to make Models $Y_{\text{defective},1}$ and 2 which model line defects of multiple line width and include pores.

This project implemented changes to Model $X_{\text{defective}}$ which benefited from the hindsight of the already collected Dataset A, which was used to make the overall model more realistic. Several changes (illustrated in Figure 4.5) were made to create Model $Y_{\text{defective},1}$ and Model $Y_{\text{defective},2}$:

1. No single vacancies were generated to minimise false positive predictions which produced noise making line defects hard to distinguish.
2. The range of possible widths of SVLs was increased to allow n-SVLs up to 5 atoms wide. In addition the range of possible line defect lengths was increased to 60 atoms.
3. Kinks in line defects were rare in most desirable experimental data. Therefore, they were removed.

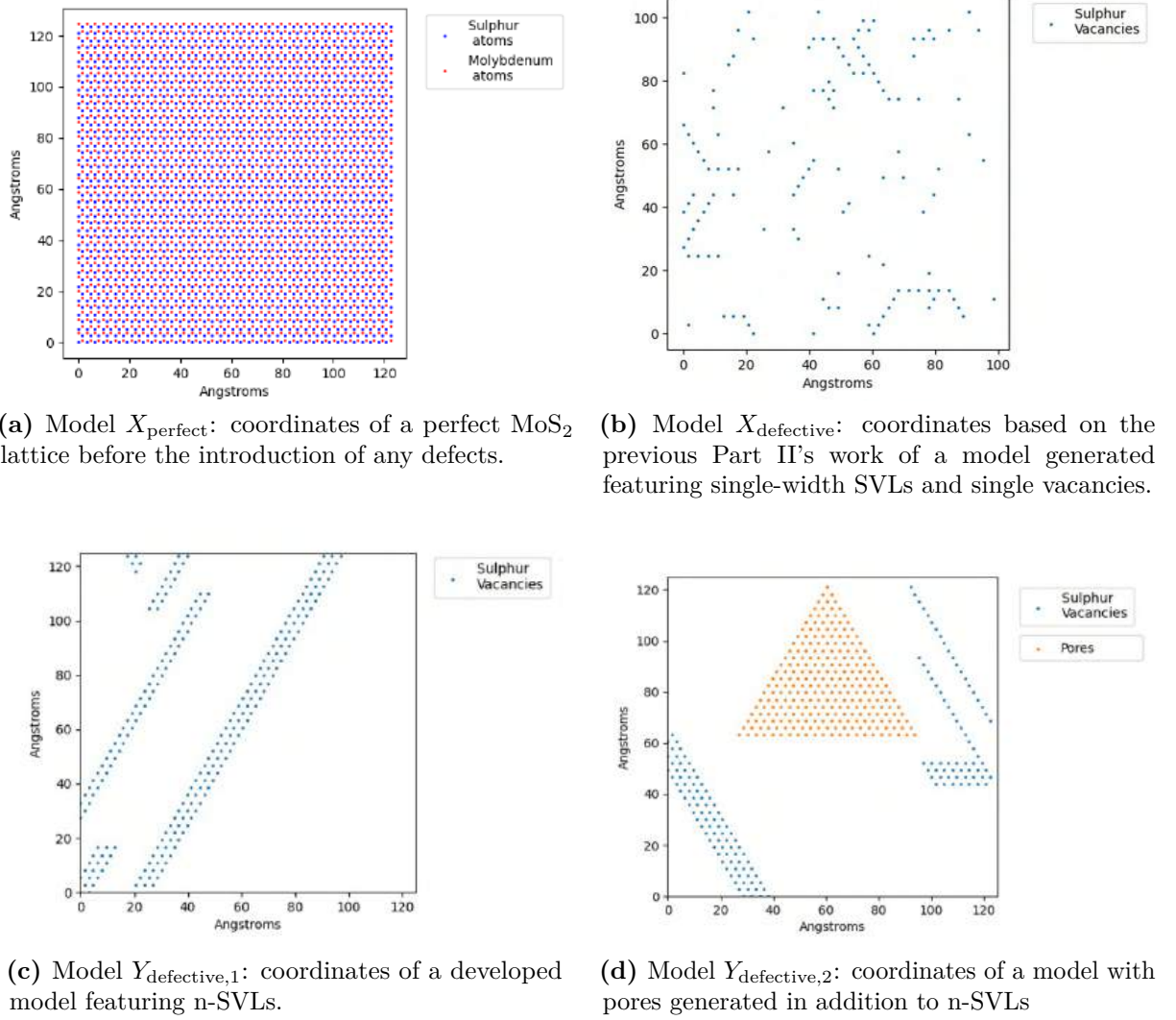


Figure 4.6: An illustration of the different models with increasing complexity developed in Figure 4.5.

4. Pores were added to 10% of Model $Y_{\text{defective},1}$, giving Model $Y_{\text{defective},2}$. Pore edges were between 15-40 atoms in length. Pore edges were parallel to the closest line defect.

The development of the models is visualised in Figure 4.6. Model generation was iterated to produce 25000 unique lattices (using random number generators) of which 90% were Model $Y_{\text{defective},1}$ and 10% were Model $Y_{\text{defective},2}$.

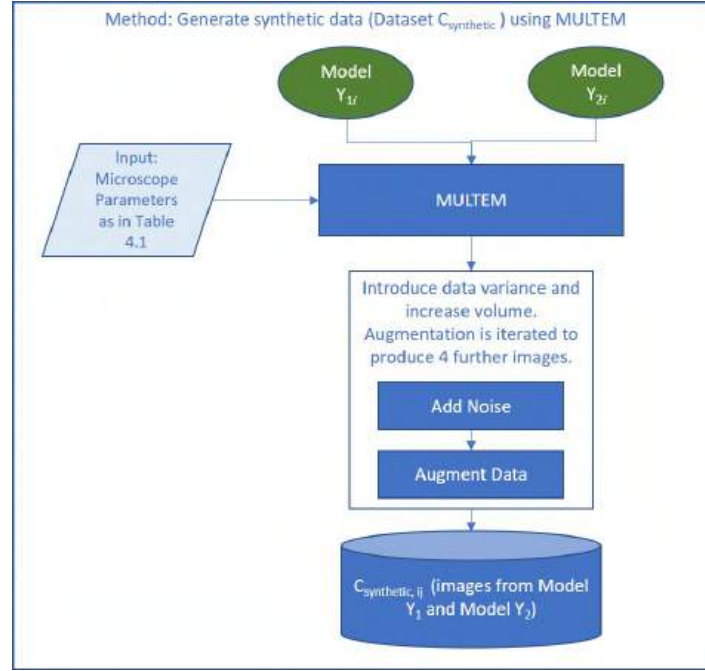


Figure 4.7: In this step, models (their creation is illustrated in Figure 4.5) are used to generate simulated images which make up Dataset $C_{\text{synthetic}}$.

4.2.2 Generating a Synthetic Dataset

Each of the 25000 generated models were fed into MULTEM to create a corresponding simulated electron micrograph. These made up a synthetic dataset (referred to as **Dataset** $C_{\text{synthetic}}$). An overview of this process is shown in Figure 4.7.

In order to maximise the diversity of simulated training data, for each generated simulation a random number generator was used to select microscope parameters within the ranges set out in Table 4.1. These reflect realistic experimental conditions. All other imaging parameters were set at the default MULTEM values.

Gaussian noise was applied to each simulated image, and a beam profile was added. This was done using functions previously written by Dr. Chen Huang. Each original image was augmented by random rotation and cropping to produce four further training images in order to increase data variance and volume. Each generated simulated image corresponded to a separate image with ground truth

Parameter	Range
Defocus	$[-120, -30]$ Å
Two-fold Astigmatism norm	$[0, 800]$ Å
Two-fold Astigmatism angle	$[0, \pi]$ rad
Three-fold Astigmatism norm	$[0, 100000]$ Å
Three-fold Astigmatism angle	$[0, 120]$ rad
Acceleration Voltage	$[65, 90]$ keV

Table 4.1: The range of possible simulation parameters.

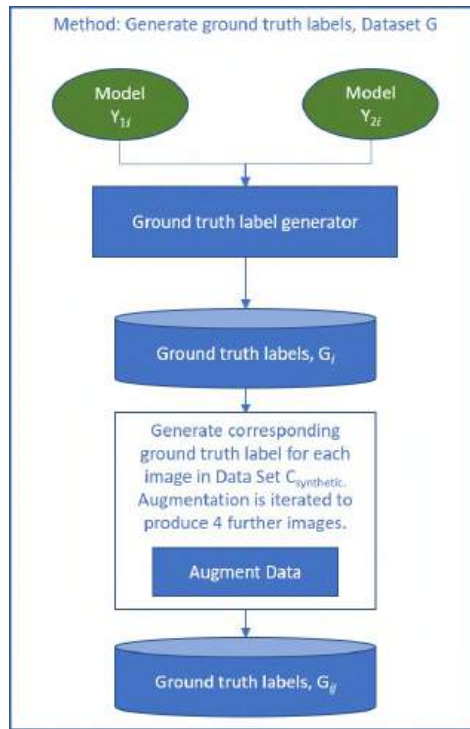


Figure 4.8: For each simulated image which is augmented, corresponding ground truth labels are also identically augmented. This gives a training data set made up of pairs of images ($C_{\text{synthetic}, ij}$ and G_{ij}).

labels which was also identically augmented (Figure 4.8). Three colours were used to label atoms: blue for molybdenum, white for sulphur, and red for sulphur vacancies. An example of training data can be seen in Figure 4.9.

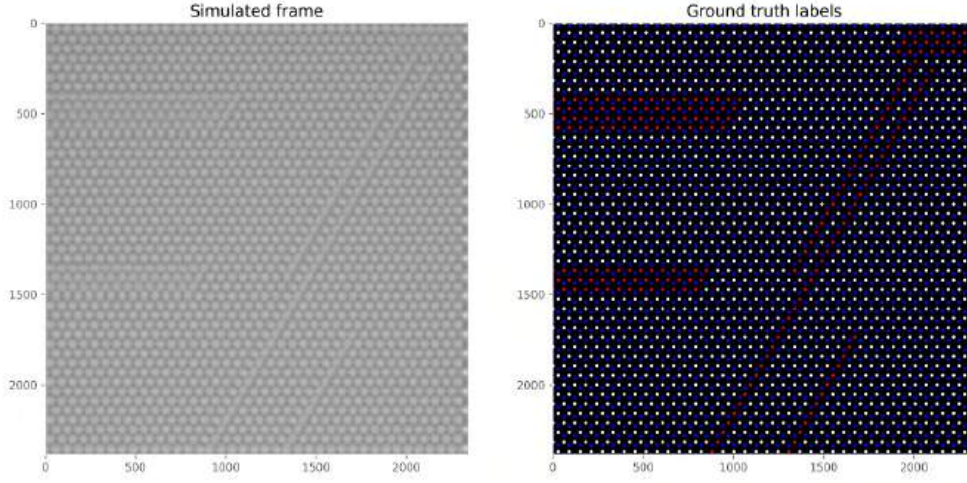


Figure 4.9: An example of training data from Model $Y_{\text{defective},1}$. Left are simulated images, right are their corresponding labels. These were fed to the CNN during training.

4.2.3 Training the Convolutional Neural Network

The CNN was built using off-the-shelf components from TensorFlow (an open source machine learning framework [75]) and based on the CNN built by Lear in 2020 [24] which is labelled U-Net Architecture X (as in Figure 4.10). In this CNN, there are four pooling layers and four de-convolution layers, each of which are sandwiched by convolution layers with a ReLU activation function. Small changes to U-Net Architecture X were made to experiment with the CNN performance, however U-Net Architecture X was not ultimately modified. Figure 4.10 illustrates how the CNN was trained and applied to experimental data. Figure 4.11 shows the CNN’s successful predictions on simulated data which indicate that it was fit for use on experimental data.

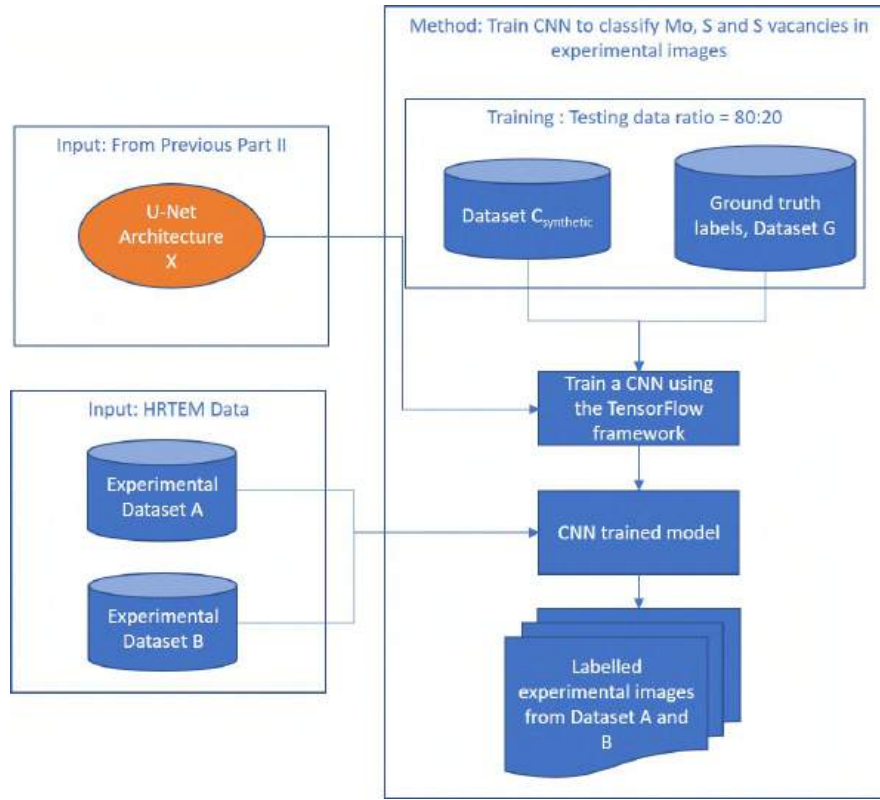


Figure 4.10: An illustration of the process described in Section 4.2.3 and 4.2.4. A CNN is trained using the Tensorflow framework.

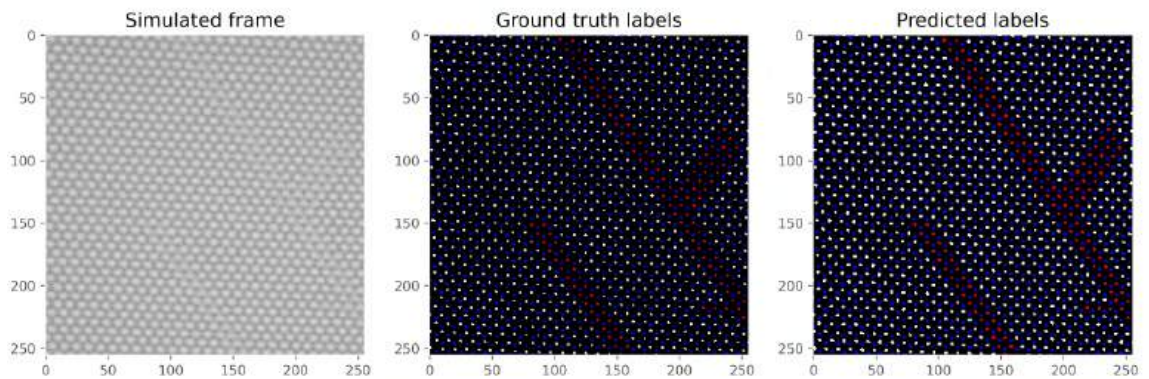


Figure 4.11: The CNN predictions compared to simulated data shows a high prediction accuracy with simulated images.

4.2.4 Applying the Convolutional Neural Network to Experimental Data

The CNN was applied to each experimental micrograph (as in Figure 4.10) which were 4096 pixels x 4096 pixels. Conditions for progression of CNN outputs, which were manually sorted, to further analysis were:

- Line defects must be clearly visible and not swamped by other noise in the prediction from amorphous regions. This rules out $\sim 75\%$ of the usable data.
- Line defects must grow within the field of view of the frame. This ruled out $\sim 50\%$ of the remaining usable data.

Despite training for 56 hours, there were still plenty of images that the CNN failed to recognise. For example, the beam profile across the image shown in Figure 4.12 causes failures of the CNN in the corners, whereas a much more desirable image is shown in Figure 4.13 which has both a smaller range of grayscale (i.e. a lower beam profile) and a higher grayscale value (i.e. higher signal to noise ratio (SNR)). A comparison of the beam profiles in these two images is shown in Figure 4.14.

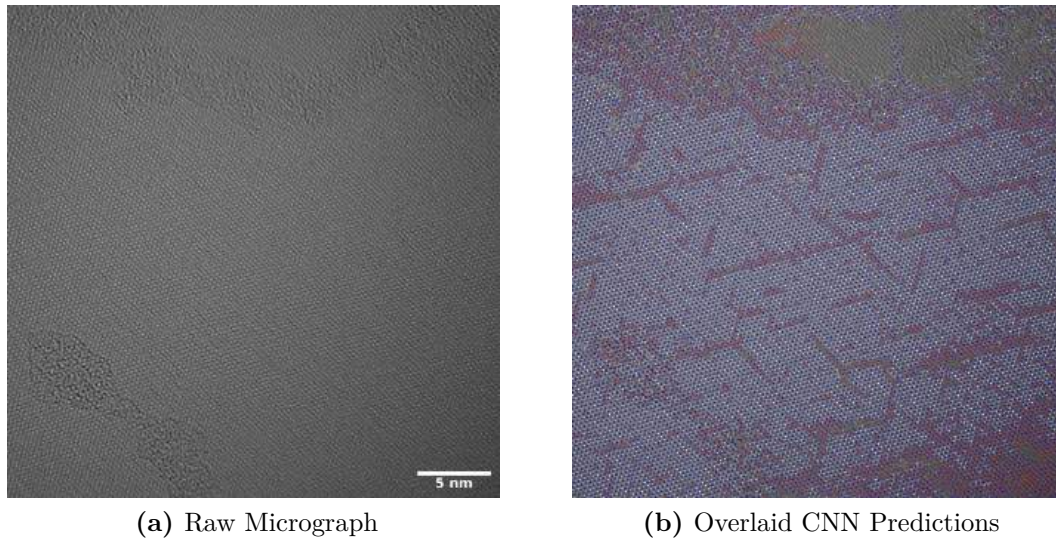


Figure 4.12: Undesirable data: a strong beam profile causes prediction problems in the lower right hand corner, the amorphous regions also confuse the CNN at the top, and the presence of a high density of short line defects means any extensive individual line defect growth unlikely to occur.

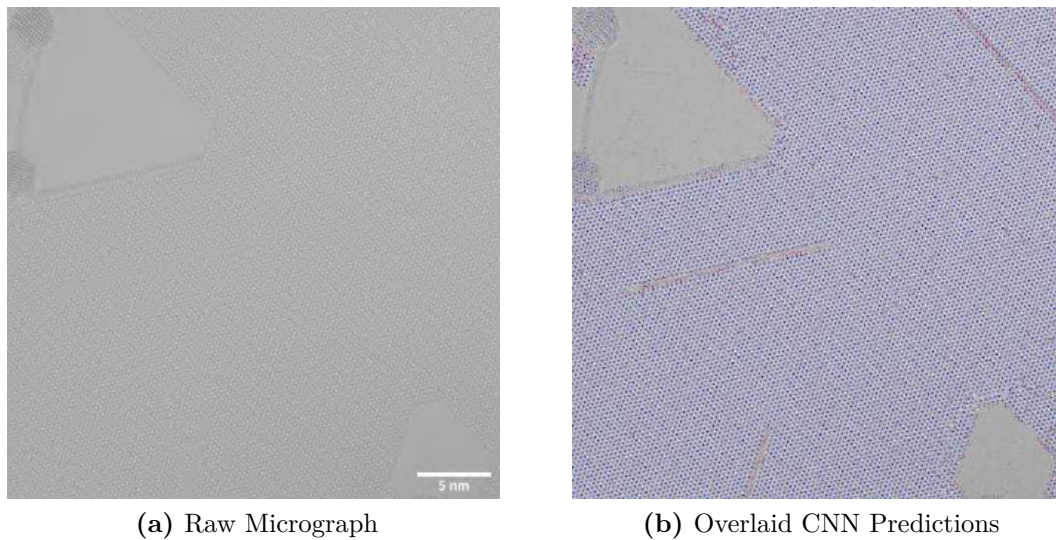
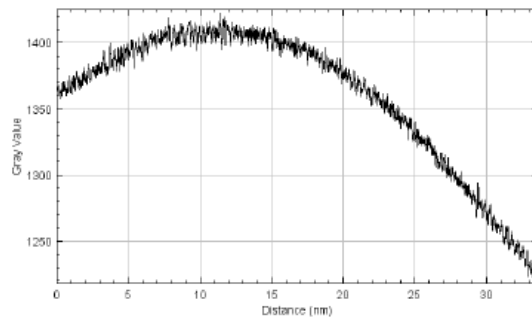
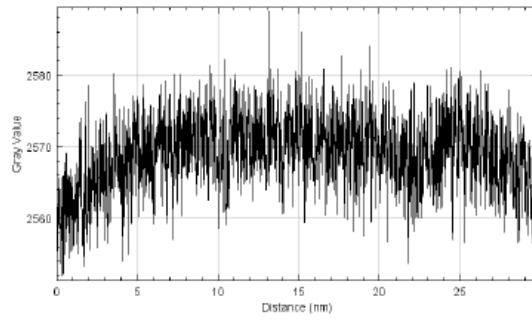


Figure 4.13: Desirable data: minimal beam profile and a largely undamaged sample allows for the successful detection and growth of long line defects.



(a) Undesirable: beam profile of Figure 4.12.



(b) Desirable: beam profile of Figure 4.13.

Figure 4.14: A strong beam profile as shown in (a) causes failure of the CNN in the regions where the profile is darkest whereas (b) shows a much smaller grayscale range due to a minimal beam profile.

4.3 Post-prediction Data Analysis

Interpreting the predictions (i.e. the output of the CNN) was a complex task due to the varying quality of data and novelty of the methods: creativity was required. Dataset A showed clear line defect growth, whilst Dataset B data had larger damaged areas. As a result, Dataset A was used to track line defect growth whilst Dataset B was used to track vacancy generation more generally as shown in Figure 4.15.

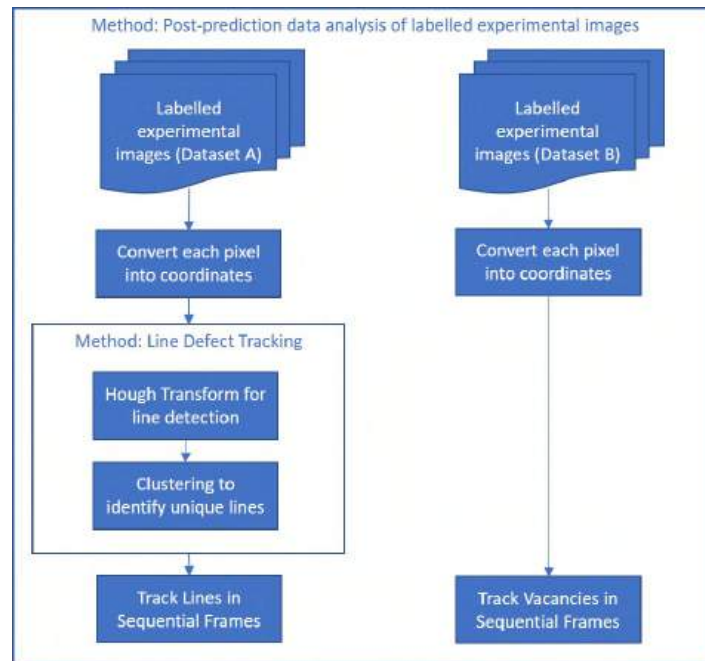
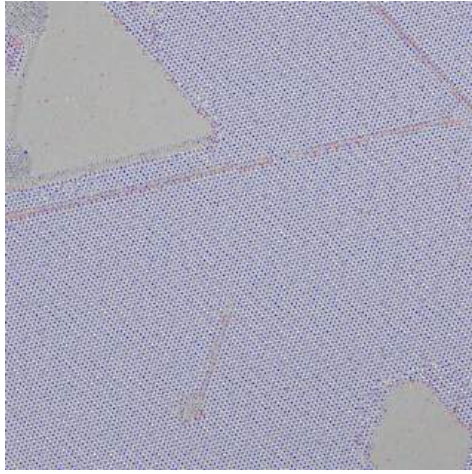


Figure 4.15: An overview of how the CNN outputs were processed in order to extract quantitative insight from the data.

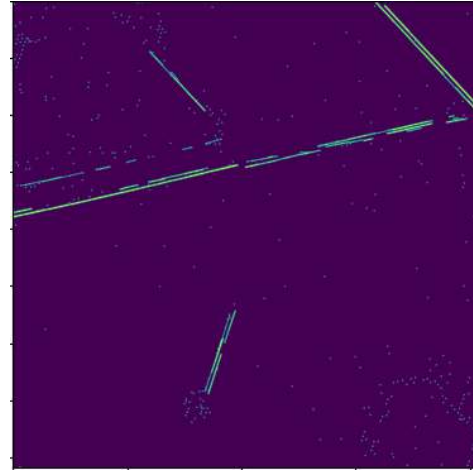
4.3.1 Line Defect Tracking in Dataset A

Several approaches were attempted to extract quantitative data from the CNN output. Software was written with the aim of delivering sequential analysis of the frames to extract the rate of defect generation, the lengthening rate of line defects, and the widening rate of line defects.

There are several stages to the final developed method as described below. This methodology is demonstrated using an example image shown in Figure 4.16 (a).



(a) The full overlay of predictions on the original micrograph.



(b) Hough Transform is applied to highlight lines in the image although each detected line does not correspond to a distinct line defect: 167 different lines are detected here.

Figure 4.16: (b) is extracted from (a) by applying a Hough Transform to isolate line defects.

Hough Transform

The original prediction was run through a Hough Transform: an image segmentation technique used to detect edges in images [76, 77] which has previously been used in electron micrographs [78, 79], although not on the atomic scale. This was implemented using the *HoughTransform* library in Python. The transform has three parameters which control its sensitivity to line detection: *Threshold*, *minLineLength*, *maxLineGap* which were set to 30, 30 and 90 pixels respectively. An extremely high sensitivity in the transform led to the introduction of falsely detected line defects which added noise. Therefore a while loop was implemented to ensure that the values of these parameters were increased or decreased so that no fewer than 20 and no more than 200 lines were detected in each image.

The output of the Hough Transform gives the start and end coordinates of each line detected in the image. Whilst the number of unique straight lines in the prediction may appear obvious to the human eye, many short overlapping lines were detected by the transform in Figure 4.16 (b) which made it difficult to distinguish

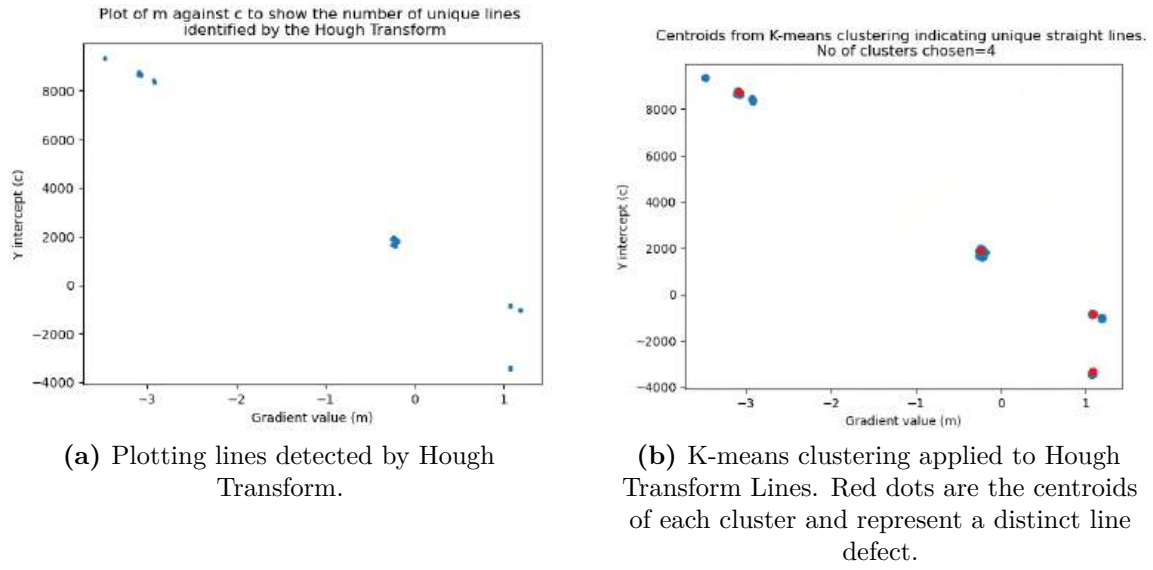


Figure 4.17: Clusters of points represent overlapping lines. Clustering was used to find the centroid of each cluster, therefore isolating the equations of individual line defects.

between different line defects. From the coordinates of each detected line, the straight line equation ($y = mx + c$) was calculated. The values of the gradient (m) and y-intercept (c) were plotted as shown in Figure 4.17 (a).

Clustering

K-means clustering was used to group the overlapping lines allowing for the detection of unique line defects. The algorithm requires a pre-set number of clusters. This was set at the beginning of each sequence of frames. The coordinates of the centroid of each cluster represent the equation of a unique line and are shown in red in Figure 4.17 (b). These lines were then plotted and overlaid onto the original prediction as shown in Figure 4.18 (a).

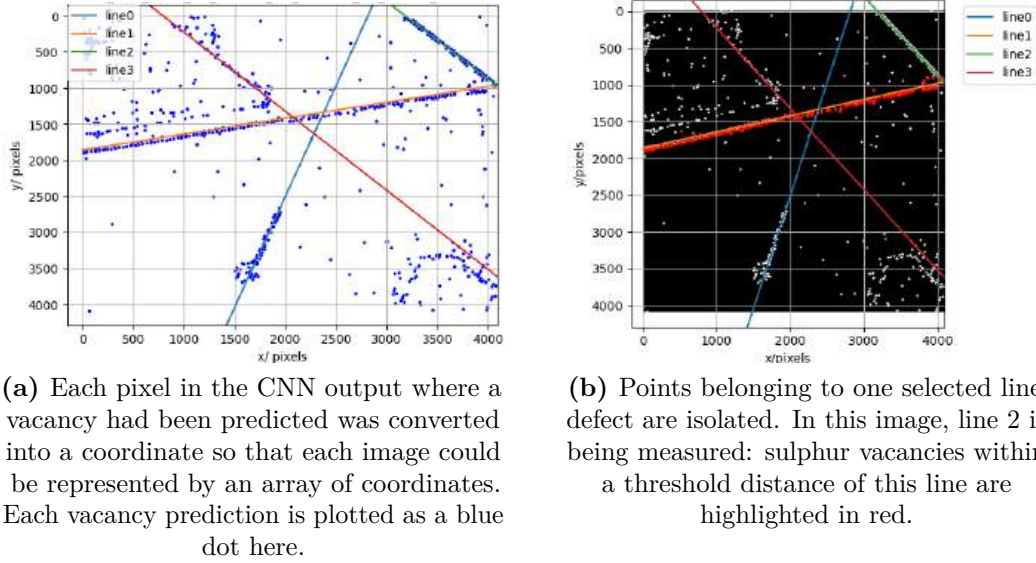


Figure 4.18: Measuring a line defect's length by making use of both the Hough Transform and CNN outputs.

All the detected vacancies (displayed as blue dots in Figure 4.18 (a)) which fell within a threshold distance of a desired line defect were isolated. They are highlighted in red in Figure 4.18 (b). Two metrics were used to analyse the identified line defect: the total length of the line defect, and the total number of vacancies in the line. The total length of the line defect was obtained by taking the distance between the extreme points in the isolated array with maximum and minimum x coordinates.

Tracking Lines in Sequential Frames

The steps outlined above were applied to each frame and the lengths of line defects were tracked across sequential frames. In order to track line defects from the very beginning of their growth (when the lines form they are not well defined and unlikely to be detected by the Hough Transform), each sequence of frames was run in reverse order. This allowed the Hough Transform to pick up all the main lines of interest when at their longest and most well-defined, and 'follow' them all the way to the earliest frames of their growth. The data was re-reversed before it was analysed.

4.3.2 Vacancy Tracking in Dataset B

Dataset B was not comparable to Dataset A. Long line defects were no longer characteristic in the remaining small undamaged monolayer regions (with estimated area size of around 700 nm^2) which were now surrounded by amorphous material. Therefore instead of tracking line defects, the change in total number of vacancies was measured. The boundary amorphous regions were removed from the images as these would add false positive predictions from the CNN. The coordinates of points bounding the amorphous regions were identified using imageJ (an image editing software) (as shown in Figure 4.19 and 4.20).

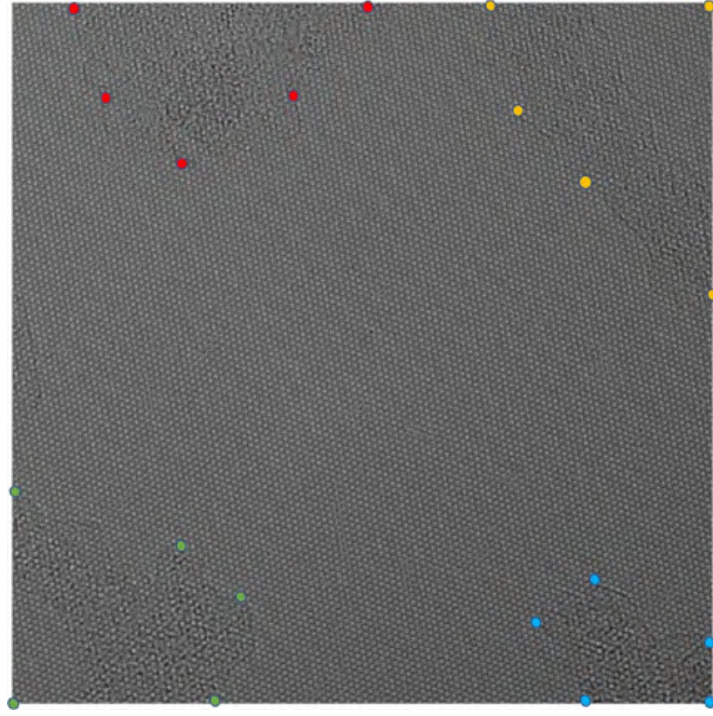
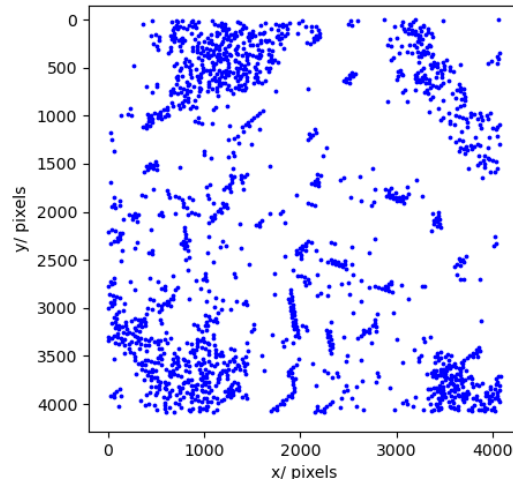
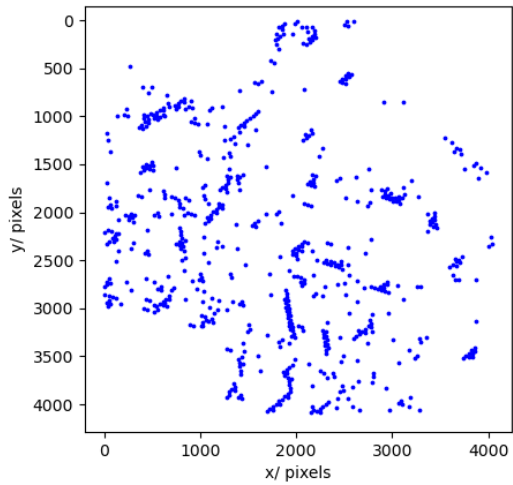


Figure 4.19: Bounding amorphous regions to leave out of analysis.



(a) Detected vacancy map with amorphous regions included (which give false positive sulphur vacancy labels).



(b) Map after amorphous regions excluded.

Figure 4.20: Removing amorphous regions highlighted in Figure 4.19 in order to avoid unwanted false positive predictions from the CNN which would invalidate analysis.

The accuracies of the CNN and line defect tracking algorithms are analysed in the results (Section 5.4.2).

5

Results

Contents

5.1	Line Defect Growth Rate	44
5.2	Observing Strain around a Defect	48
5.3	Effect of Dose and Defect Density on Rate of Vacancy Production	52
5.4	Managing and Mitigating Errors	56

In this chapter, results and analysis of Dataset A are presented in Section 5.1-5.2, whilst results from Dataset B are presented in Section 5.3.

5.1 Line Defect Growth Rate

Results showing lengthening of individual line defects in Dataset A are displayed in Table 5.1. The growth of two of these lines, which are representative of the rest of the data, are plotted in Figure 5.1. For each line defect measured, a line of best fit was drawn using the least squares fitting method to ascertain whether a linear fit was appropriate.

The R^2 values shown in Table 5.1 illustrate a good fit to linear growth of line defects. The line defect tracking method developed in Section 4.3.1 was manually supervised to ensure that any errors or misleading results from the method were spotted. The anomalous behaviour of Line 7 was confirmed by a two-sided statistical Grubs test at a confidence level of 5% (Appendix B.4.1). This is discussed in Section 6.1.

The overall equation for line-length was found to be:

$$L = 6.5 (\pm 0.2) x + 4.5 (\pm 0.7), \quad (5.1)$$

Line Number	Lengthening Rate (nm/s)	R ²
Line 1	6.61	0.94
Line 2	6.82	0.90
Line 3	6.53	0.83
Line 4	6.71	0.87
Line 5	6.55	0.78
Line 6	5.62	0.90
Line 7*	2.72	0.93

Table 5.1: The rate of line lengthening measured for different line defects observed. Anomalous results have been highlighted (*) in red and are discussed in this section.

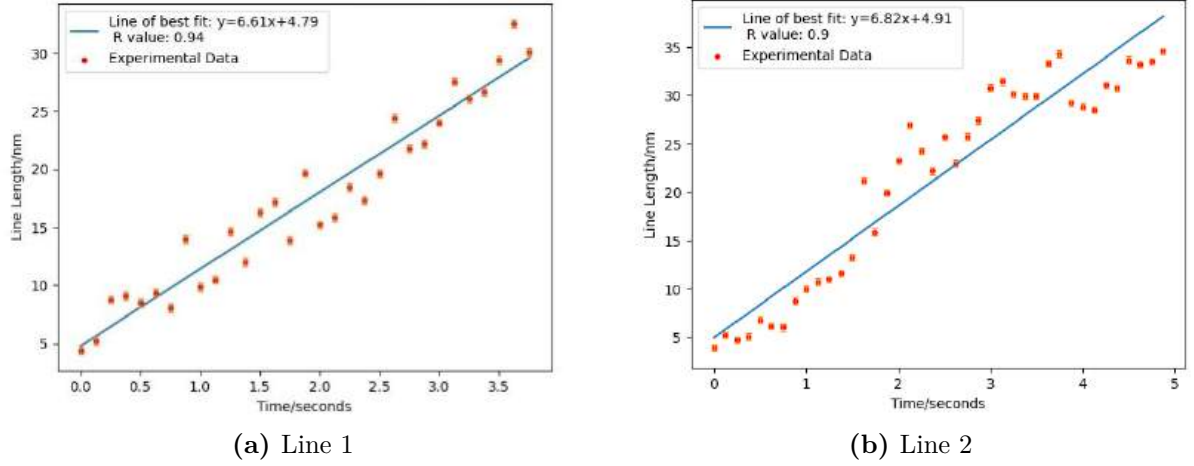


Figure 5.1: Graphs (a) and (b), which are Lines 1 and 2 in Table 5.1, are two typical examples of line defect growth. Error bars are plotted in orange.

where L is line length (nm), and x is time (s). Equation 5.1 shows that line defects lengthen at a rate of $6.5 (\pm 0.2) \text{ nm s}^{-1}$, which equates to $20 (\pm 1)$ atoms, with an initial length of $4.5 (\pm 0.7) \text{ nm}$.

The mean value (\bar{m}), standard deviation (σ), and standard error (ϵ), of the line gradient, were calculated using [80]:

$$\bar{m} = \frac{1}{n} \sum_{i=1}^n m_i, \quad (5.2)$$

$$\sigma = \sqrt{\frac{1}{n-1} \sum_{i=1}^n (m_i - \bar{m})^2}, \quad (5.3)$$

$$\epsilon = \frac{\sigma}{\sqrt{n}}. \quad (5.4)$$

Error in c , the line-intercept, was calculated the same way.

The error bars in Figure 5.1 and 5.3 take account of both micrograph calibration error and the CNN's accuracy. The latter is defined by the difference between CNN and human measurement. This error was found to be $\pm 2.9 \text{ \AA}$ (calculated in Section 5.4.2). This error is compounded with the micrograph calibration

error of 1.6\AA (Appendix B.1). Errors in line length are compounded according to the following equation [80]:

$$\frac{\Delta \text{line length}}{\text{line length}} = \sqrt{\left(\frac{\Delta c}{c}\right)^2 + \left(\frac{\Delta n}{n}\right)^2}, \quad (5.5)$$

where $\frac{\Delta c}{c}$ is calibration error, and $\frac{\Delta n}{n}$ is the CNN error. This gives a total line length error of $\pm 3.3\text{\AA}$.

One observation made was a line defect (shown in Figure 5.2) which appeared to be shortening as it moved out of the field of view at a rate of $8.6 (\pm 0.3) \text{ nm s}^{-1}$. A statistical two-sided Grubs test at a 5% confidence level (Appendix B.4.1) found that the rate of line defect movement in Figure 5.3 was significantly higher than other line defects growth shown in Table 5.1. This behaviour is discussed in Section 6.6.1.

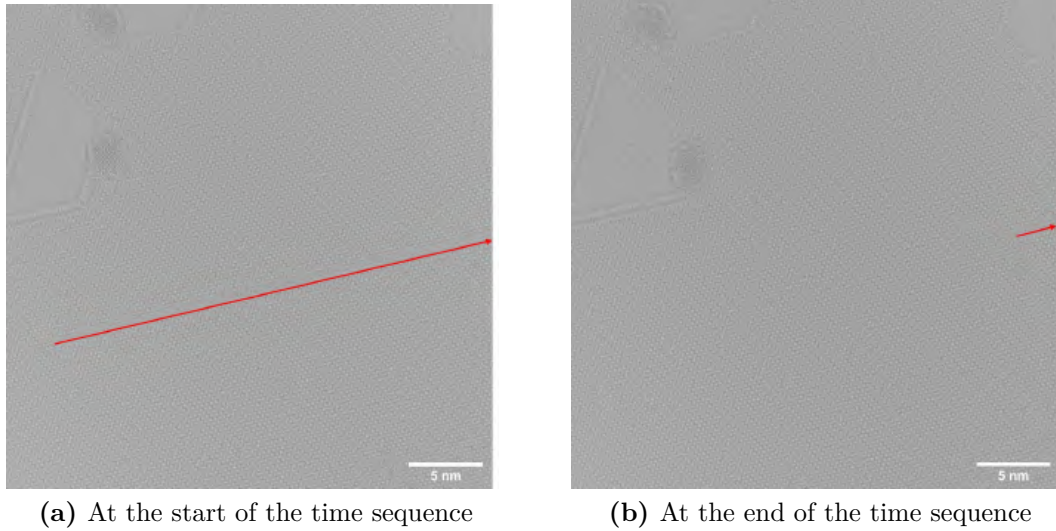


Figure 5.2: The line defect perceived to be shortening is highlighted in red.

Both the lengthening and widening rates were recorded. However, the uncertainty when measuring the defect width was much higher than when measuring defect length, given that width is a fraction of the latter (line defect widths are typically between 1-5 atoms, whereas the lengths are between 20-140 atoms). This larger error prohibited any quantitative conclusions from this project about the nature of widening. Widening rates are instead discussed in Section 6.2.

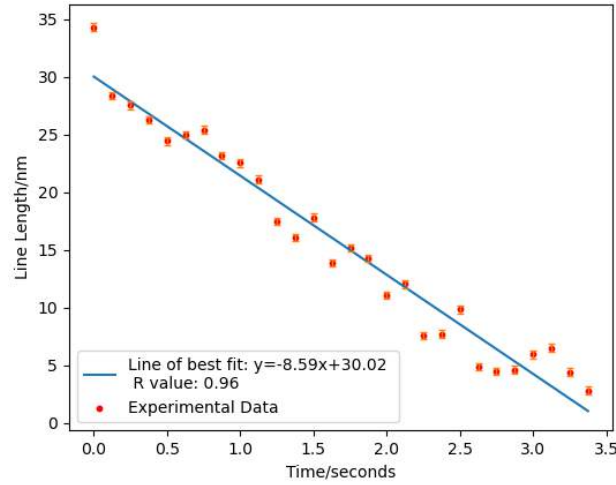


Figure 5.3: The shortening rate of the line defect.

5.1.1 Sputtering Cross Section for Sulphur in MoS₂

An experimental value for sputtering cross section of sulphur in MoS₂ was calculated from Equation 5.1. It was assumed that all the vacancies generated migrate to the line defect because of the low extent of damage elsewhere and that the area from which the vacancies appear is equivalent to the field of view. Equation 5.6 can be used to link sputtering cross section and the number of sulphur vacancies generated:

$$n = N \cdot \sigma \cdot F, \quad (5.6)$$

where n is the number of sputtered sulphur atoms per \AA^2 per second, N is the number of sulphur atoms per \AA^2 (this value is calculated to be 0.3 in Appendix B.3), σ is the sputtering cross section for sulphur atoms in MoS₂, and F is the flux (i.e. dose rate). For Dataset A, flux is 30715 electrons \AA^{-2} (Appendix B.2).

From Equation 5.1, $20 (\pm 1)$ atoms are sputtered from an area assumed to be the same as the field of view ($32 \text{ nm} \times 32 \text{ nm}$) each second. Therefore,

$$\begin{aligned} n &= \frac{20 \text{ atoms s}^{-1}}{(320 \text{ \AA})^2} \\ &= 1.9 (\pm 0.1) \cdot 10^{-4} \text{ s}^{-1} \text{\AA}^{-2} \end{aligned}$$

The experimental value of sputtering cross section of sulphur is therefore:

$$\begin{aligned}\sigma &= \frac{n}{N \cdot Flux} \\ &= \frac{1.9 \cdot 10^{-4}}{0.3 \cdot 30715} \\ &= 2.1 (\pm 0.1) \cdot 10^{-8} \text{\AA}^2.\end{aligned}$$

Using the conversion between units $1 \text{ barn} = 10^{-8} \text{\AA}^2$, the experimental value of σ is $2.1 (\pm 0.1) \text{ barn}$. The theoretical value of σ for sulphur in monolayer MoS_2 at 80 keV is calculated using the McKinley-Feshbach equation and is 0.8 barn [81]. The experimentally calculated value is 2.6 times larger than the theoretical value, which is in reasonable agreement considering the difference between theoretical and experimental conditions. The difference between these values is further discussed in Section 6.3.

5.2 Observing Strain around a Defect

The level of confidence in the CNN's predictions were further tested by investigating whether atomic mappings would reveal expected strain in the surrounding lattice. Due to time constraints, only one experimental image was selected in which a line defect 11 atoms long and 4 atoms wide was observed. This selected region was rotated, cropped and then overlaid on top of a pristine lattice for comparison. Point (0,0) in Figure 5.5 was assumed to be strain free and used as the reference point. Atomic displacement from bulk lattice sites were calculated and plotted in Figure 5.6.

The error in the alignment of pristine and experimental lattices is $\pm 0.6 \text{ pm}$ (Appendix B.1). Maximum recorded displacements are over an order of magnitude larger than this error (with 70 pm being the largest recorded displacement as in Table 5.2) and are therefore meaningful results.

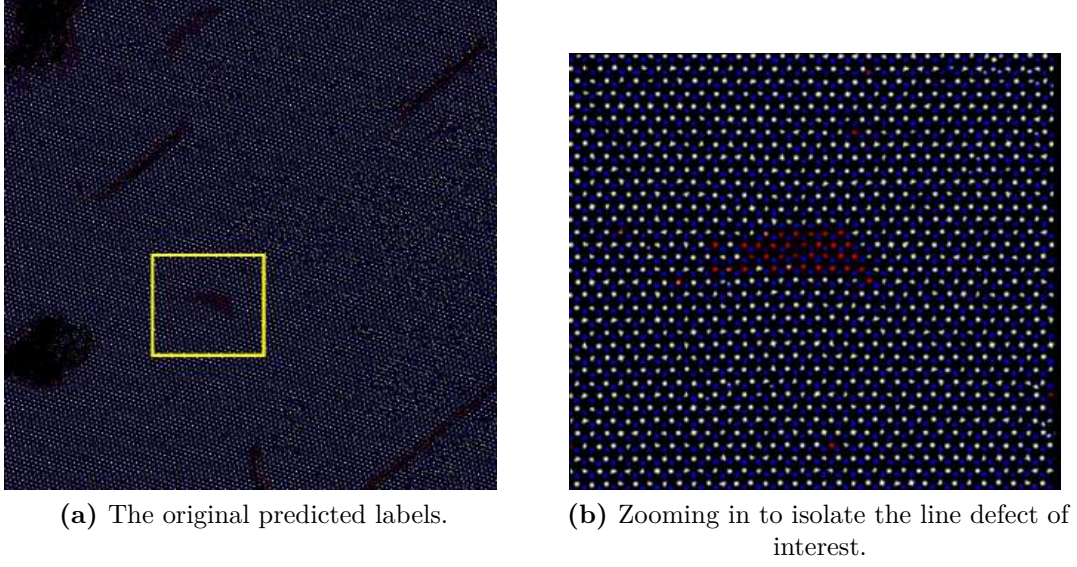


Figure 5.4: The chosen line defect to visualise any detected strain.

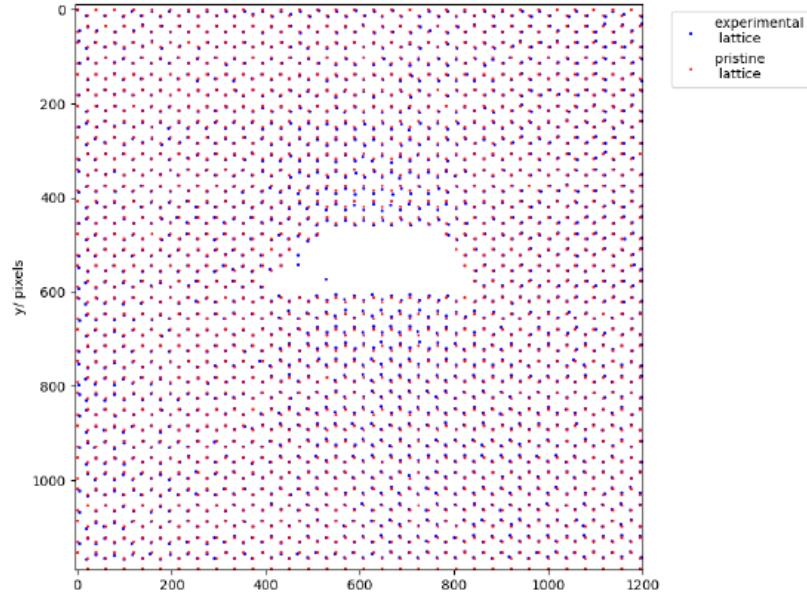


Figure 5.5: Experimental lattice overlaid on a pristine lattice (line defect excluded). Point (0,0) is the reference point. Displacement detected by the CNN is largest closest to the defect, as expected.

The corresponding strain tensor was calculated with help from Xiaonan Luo using a method previously used to measure strain in nano-particles [82]. The strain tensor takes the form:

$$\begin{pmatrix} \varepsilon_{xx} & \varepsilon_{xy} \\ \varepsilon_{yx} & \varepsilon_{yy} \end{pmatrix}. \quad (5.7)$$

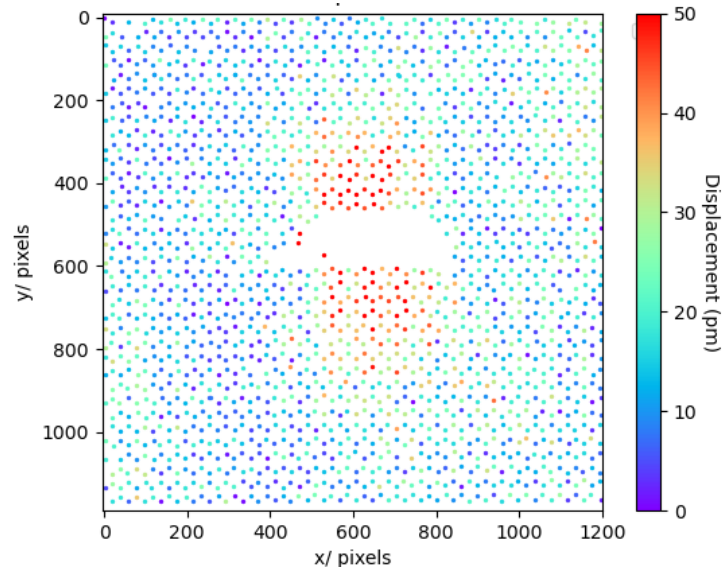


Figure 5.6: Colour map showing magnitude of displacement. The largest displacements are closest to the defect as would be expected.

	Max Value	Min Value
Displacement (pm)	70	0
ε_{xx}	0.40	-0.30
ε_{yy}	0.22	-0.39
ε_{xy}	0.47	-0.29

Table 5.2: Table showing the range of values for displacement and the calculated strain tensors. The error for all the values is ± 0.6 pm.

Each component of the tensor is plotted in Figure 5.7. The range of values of each calculated component are shown in Table 5.2.

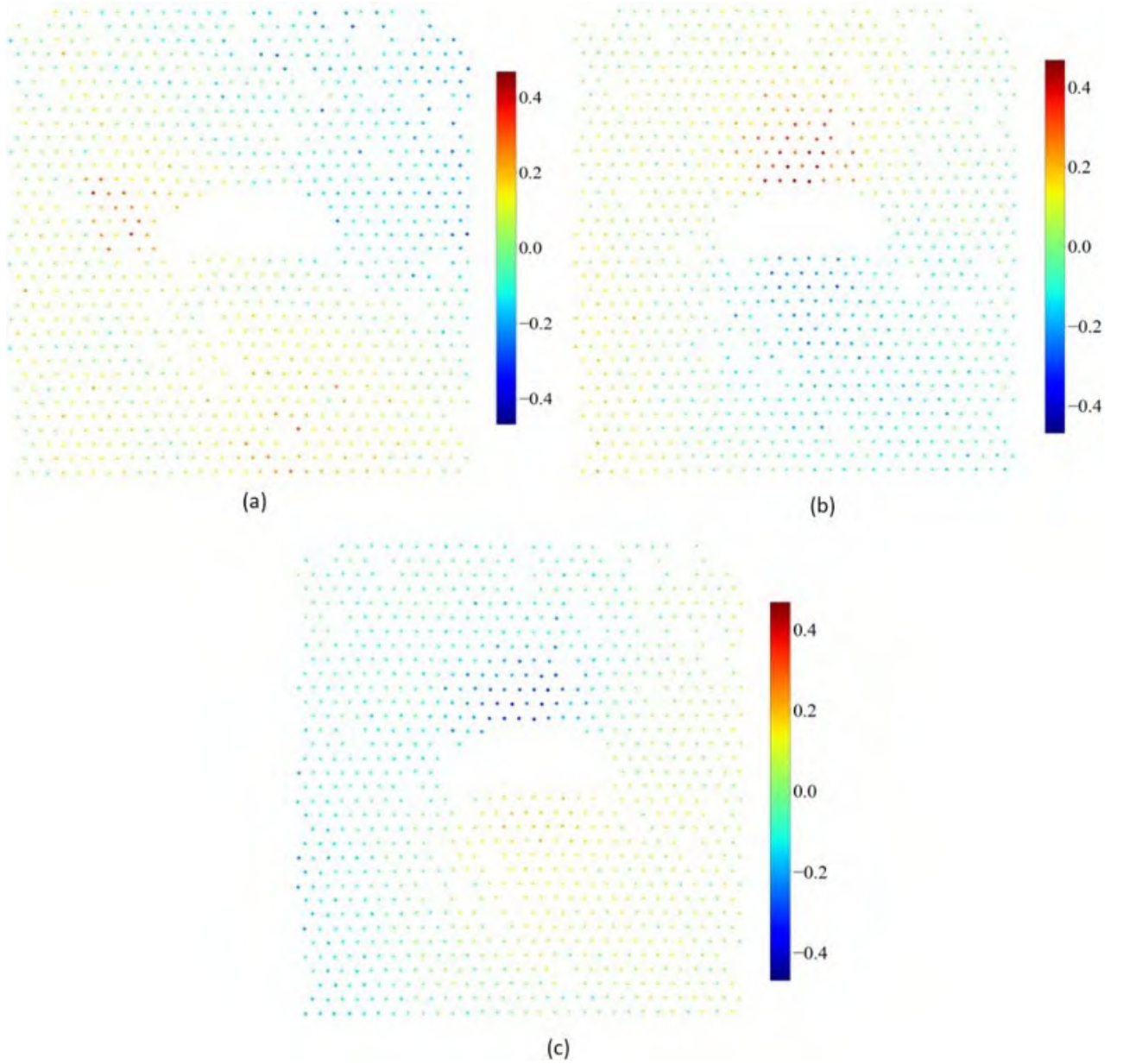


Figure 5.7: Components of the strain tensor: (a) ε_{xx} , (b) ε_{yy} , (c) $\varepsilon_{xy} = \varepsilon_{yx}$ calculated from Figure 5.6 using methods from Ellaby *et al.* [82] with help from Xiaonan Luo.

5.3 Effect of Dose and Defect Density on Rate of Vacancy Production

Dataset B was used to investigate the effect of dose and dose rate on line defect growth. Data were obtained at five dose rates as shown in Table 5.3. Dose rate error comes from the precision of current measured; the microscope's detectors are highly accurate so these errors are insignificant.

Dose Rate (electrons $\text{\AA}^{-2} \text{s}^{-1}$)	Number of available datasets
56705	4
29032	3
20450	2
10630	3
8539	1

Table 5.3: The different dose rates of data collected in Dataset B.

The results showed variable starting defect densities in different regions of the sample. This variety warranted additional investigation into the effect of defect density on vacancy generation. Figure 5.8 shows the need to segment Dataset B for an investigation of dose effect independent of the defect density. Table 5.4 shows how the data was segmented; an example of a segmented data set for Interval 2 is shown in Figure 5.9. Error bars are not plotted in Figures 5.8 and 5.9 because they are set by the CNN's performance. It is very hard to directly measure CNN error in counting numbers of vacancies to any meaningful precision.

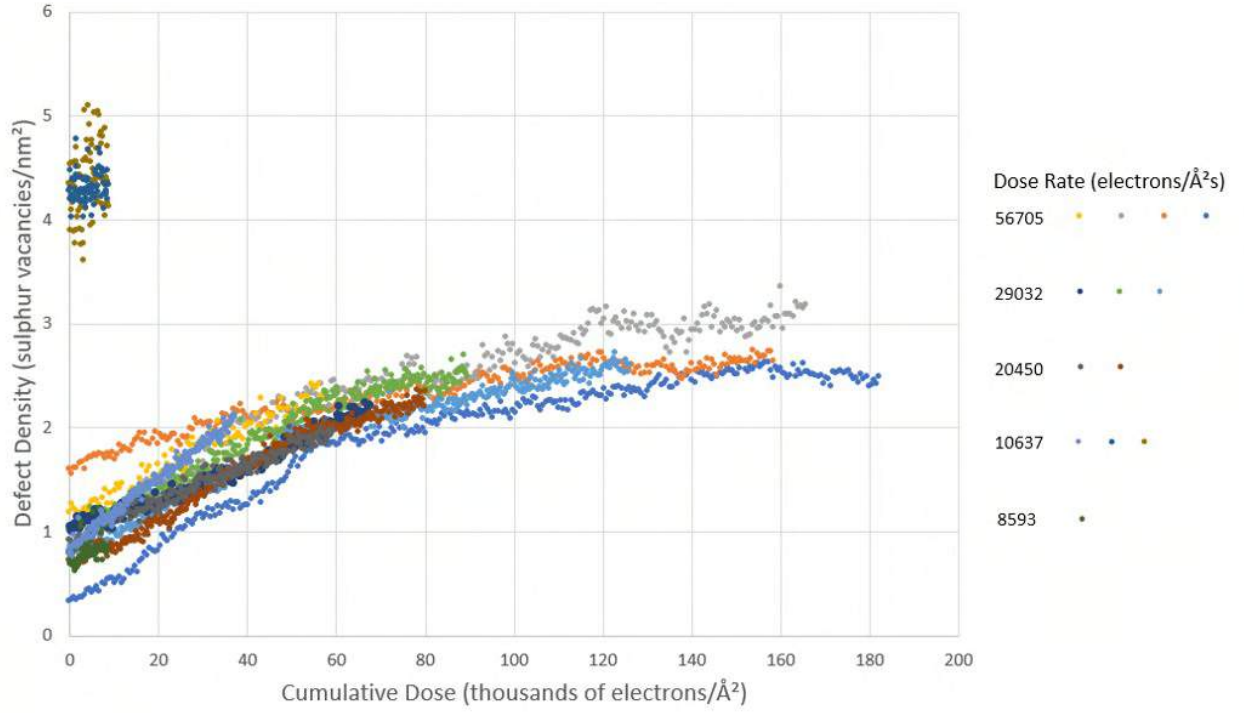


Figure 5.8: Dataset B is made up of sub-datasets with varying degrees of damage as can be seen by the varying y-intercepts. The inconsistent gradients suggest that the defect density has an effect on the damage. For these reasons, Dataset B was segmented for further analysis.

Name of Interval	Defect Density (vacancies nm ⁻²)	Dose Rates available for this interval (electrons Å ⁻² s ⁻¹)
Interval 1	0.7-1.6	56705, 29032, 20450, 10630, 8539
Interval 2	1.6-2.5	56705, 29032, 20450, 8539
Interval 3	2.5-3.4	56705, 29032, 8539
Interval 4	3.4+	10630

Table 5.4: The intervals of defect density chosen for segmented analysis. The use of multiple datasets under the same conditions allowed for standard errors to be calculated using Equation 5.4.

5.3.1 Cumulative Dose vs Dose Rate Dependence

Firstly, analysis aimed to distinguish between the effect of accumulated dose and dose rate. The total number of electrons arriving at the sample was compared to the number of defects created. As shown in Figure 5.9, for each of the chosen intervals of defect density, the change in defect density caused by the same accumulated dose

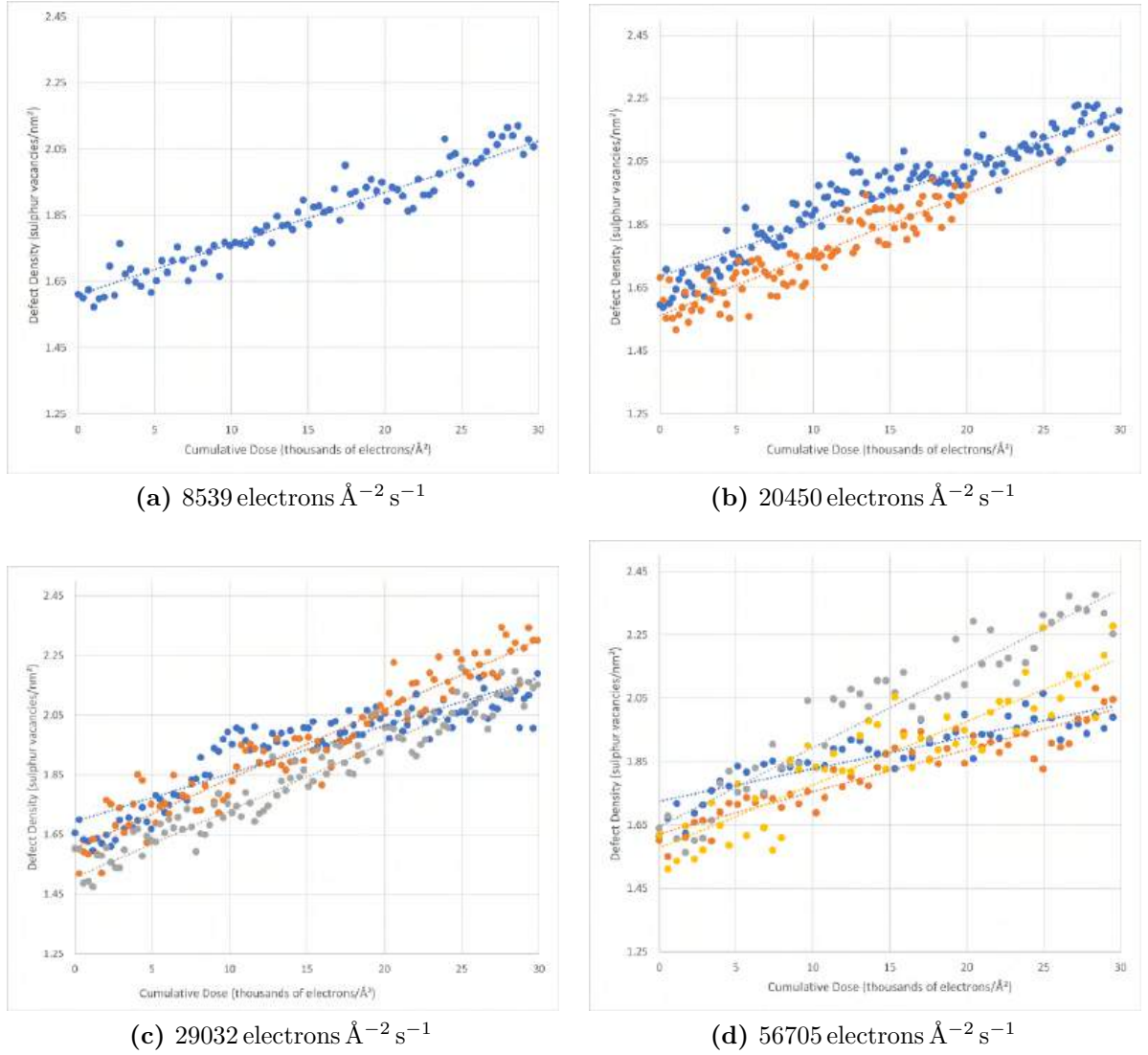


Figure 5.9: Illustration of how data from Figure 5.8 is segmented for a fair dose rate comparison. The defect density interval (Interval 2) is 1.6 – 2.5 vacancies/nm² and all data from four different dose rates are shown. The gradients of these lines of best fit are compared across dose rates in Figure 5.10.

was compared across all dose rates. At the highest defect density interval, data was only taken for one dose rate so no comparison was possible here.

Figure 5.10 shows no strong correlation between the number of defects generated per amount of arriving electrons and the rate at which these electrons arrive. Standard errors in Figure 5.10 were calculated using Equation 5.4 [80].

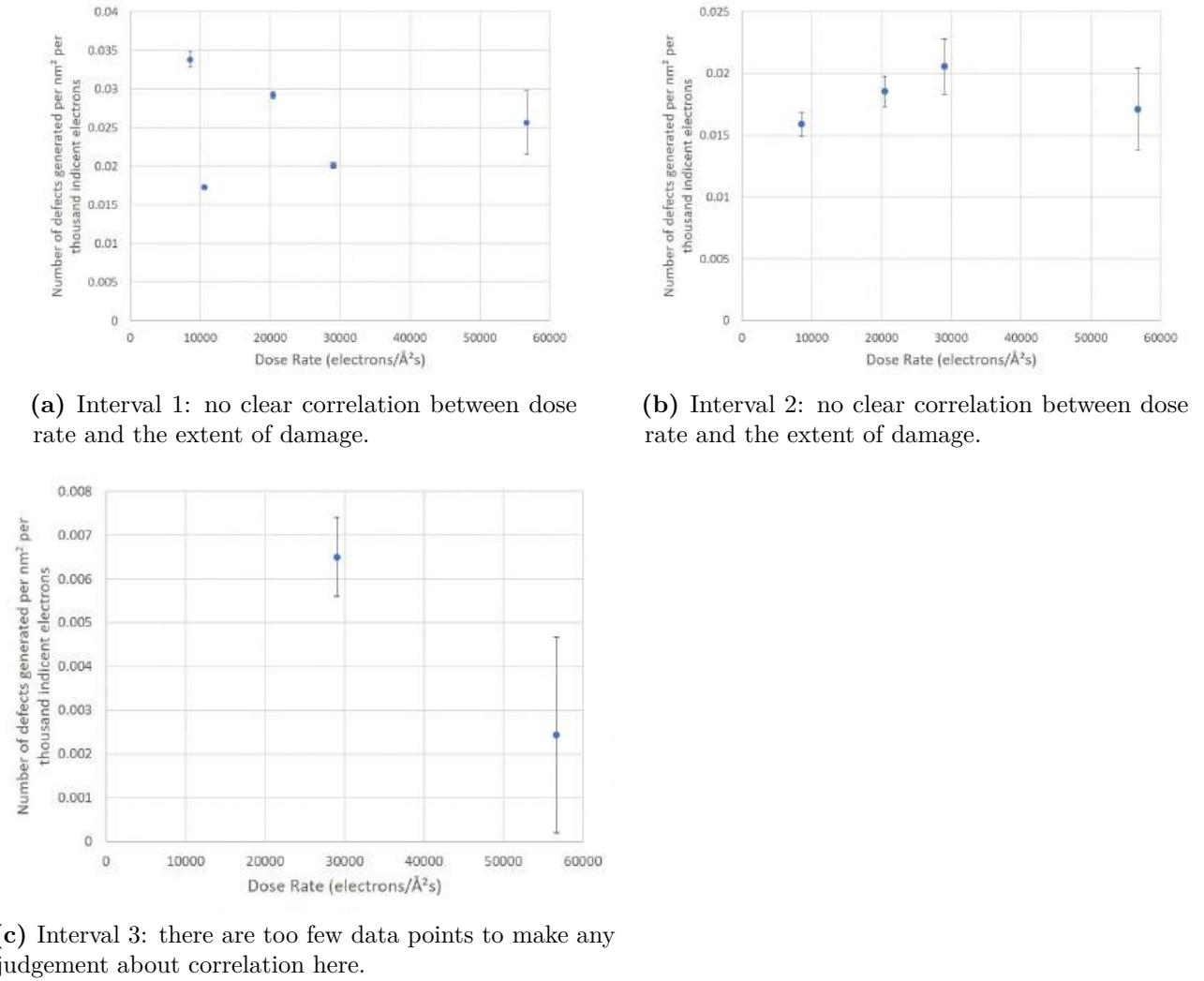


Figure 5.10: Given the same cumulative dose, there is no obvious correlation in interval 1 or 2 between the dose rate and overall damage.

5.3.2 Effect of Cumulative Dose

As shown in Figure 5.9, accumulated dose and the rate of defect generation are positively correlated to defect generation rate as expected: although this was not found to be directly proportional (as analysed in Section 5.3.3). Whilst comparison of dose rate and the rate of defect generation also show a positive correlation, Section 5.3.1 has shown that the underlying reason for this behaviour is due to the effect of cumulative dose.

5.3.3 Defect Density Dependence

In Figure 5.8, it can be seen that the lattices with a starting defect density of around 4 sulphur vacancies nm^{-2} , which were taken at a dose rate of $10637 \text{ electrons } \text{\AA}^2\text{s}^{-1}$, did not display any increase in vacancy generation. However, another sub-dataset of Dataset B taken at the same dose rate but with a lower starting defect density of $0.8 \text{ sulphur vacancies } \text{nm}^{-2}$, did display an increase in vacancy generation. This suggests that stagnation in vacancy generation is linked to the increased defect density, rather than a low dose rate.

To further support this, Figure 5.11 shows a decrease in the rate of vacancy generation as defect density increases. This quantifies the change of slope seen in Figure 5.8. Standard errors in Figure 5.11 were calculated using Equation 5.4.

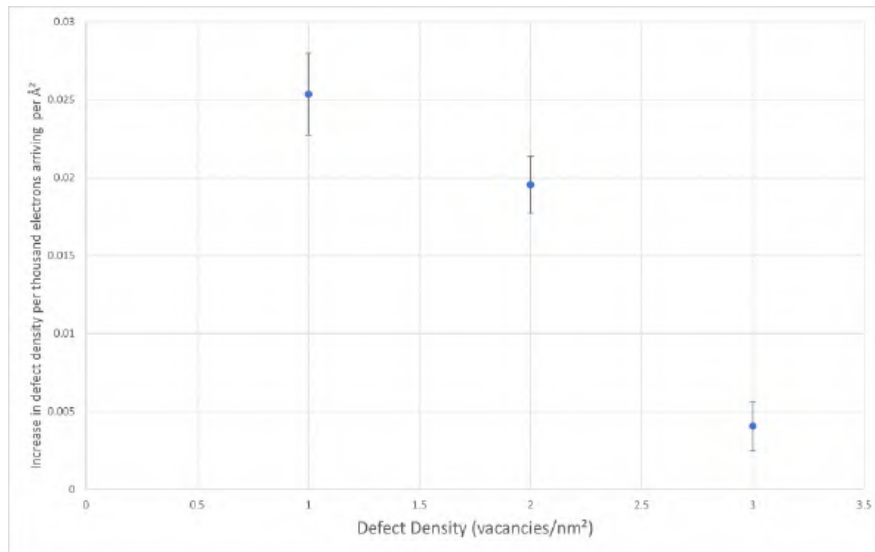


Figure 5.11: The rate of damage decreases as defect density increases, implying an effect of defect density in addition to dose effects.

5.4 Managing and Mitigating Errors

Aside from errors in the post-prediction analysis which are directly presented with the results, there are also other sources of error introduced in the methods used.

The section below discusses how these errors were quantified and mitigated.

5.4.1 Accuracy of MULTEM Simulations

To simulate any defects, they are introduced in an effective supercell to MULTEM and images are calculated using the periodic continuation method [33]. This method creates overlap artifacts: unwanted signal from scattering of atoms on the opposite side of the supercell due to artificial periodicity. To eliminate this, each defective model (i.e. each supercell) was padded with a vacuum a third its size.

5.4.2 Accuracy of the Convolutional Neural Network

Whilst training the CNN, training loss and accuracies were reported based on cross-validation. Despite being used widely in the computer science world, reported accuracy does not reflect experimental accuracy because of an inevitable difference between experimental and simulated images. Therefore, metrics were manually created to evaluate the CNN. Two methods were used to evaluate the CNN.

a) CNN's performance on simulated data

The CNN was shown freshly simulated data and its output predictions were compared to the ground truth labels. The predicted number of vacancies was compared to the actual number of vacancies using a nearest neighbour's search to give the percentage of correctly predicted sulphur atoms.

This gave an average accuracy of 82.3%. It was observed that the CNN often failed to predict the presence of all sulphur vacancies within a line defect but was good at spotting the ends of the defect. Therefore, the more accurate metric to measure the line defects is line length, rather than the number of vacancies in the defect, as the latter is more susceptible to the CNN's tendency to under-predict.

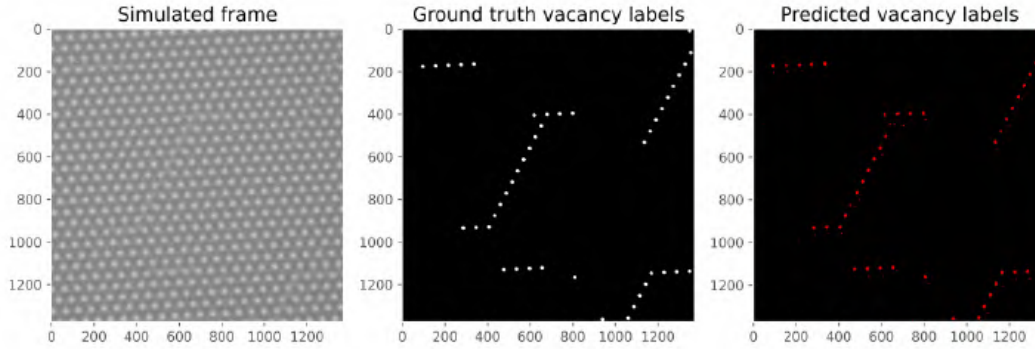
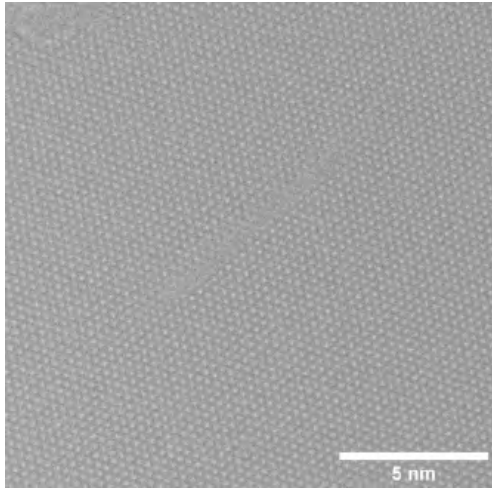


Figure 5.12: Successful CNN performance on testing data alike the training data.

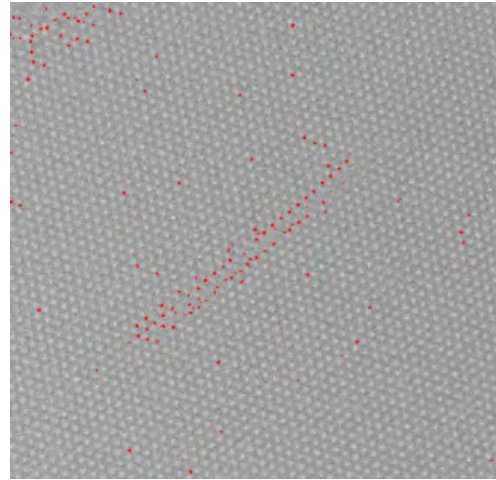
b) CNN's success compared to human vacancy labelling

Given the lack of ground truth in experimental images, human labelling was used for comparison against the CNN's predictions in Dataset A. The human measurements were generated by randomly selecting 30 experimental images to be labelled from the pool of images which had been used to give the results shown in Figure 5.1. Before hand-labelling, the image contrast was inverted to provide white atom contrast, and a false-colour LUT (Look Up Table) was applied to make atoms clearer for the human eye. The total line defect length was measured and compared to the CNN's predicted line-length. Figure 5.13 illustrates this process.

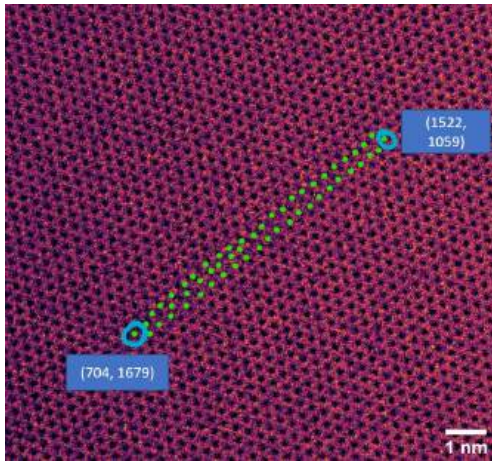
Across the 30 images, the difference in measured length had a mean of ± 0.29 nm (2.62%). The error is not systematic because there was no consistently larger measurement between the human and CNN performances. Considering that this error is 9% of the S-S bond length and that line defects could be up to 140 atoms long, the performance from the CNN in Dataset A matches very well to a trained human. A χ^2 test showed that there was no statistically significant difference found between CNN and human performance (Appendix B.4.2). However, the trained human had seen the CNN predictions before labelling so some bias is inevitable.



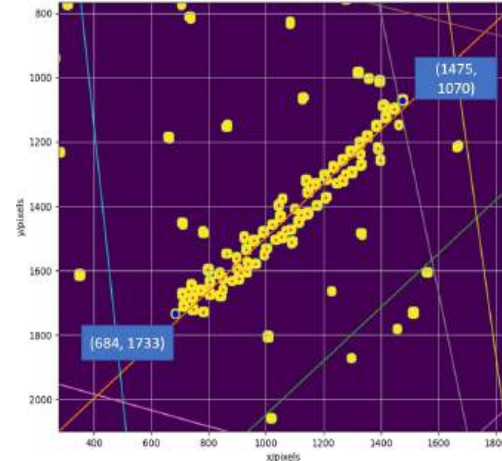
(a) Raw Image



(b) CNN-labelled Image



(c) Manual Labelling Measurement from Raw Image



(d) Hough Transform Measurement from CNN-labelled Image

Figure 5.13: CNN vs Human Labelling: the lengths of line are calculated using the two extreme points measured (measured coordinates shown). The CNN takes 0.5s to predict on an entire image. Human labelling took 10 minutes per image.

6

Discussion

Contents

6.1	Lengthening of Line Defects	61
6.2	Widening of Line Defects	62
6.3	Sputtering Cross Section for Sulphur in MoS ₂	63
6.4	Observing Strain	64
6.5	Inversion Domain Detection	65
6.6	Interaction of Line Defects with Pores	68
6.7	Effect of Dose and Dose Rate	73
6.8	Effect of Defect Density	73
6.9	Novelty of Method	76
6.10	Limitations	77
6.11	Summary	77

Results from both Datasets A and B are discussed in this chapter. Points of discussion derived from Dataset A are addressed in Sections 6.1 - 6.6 whilst Dataset B is discussed in Sections 6.7 - 6.8.

6.1 Lengthening of Line Defects

Equation 5.1 indicates that the rate of line defect growth is well described by a linear fit for defects between 5 nm – 60 nm. Line 7 in Table 5.1 lengthened at a statistically significant lower rate. This line defect was in close proximity to a pore and another non-parallel line defect. An explanation for slower lengthening could be the interference of strain fields of the other nearby line defect. Nearby vacancies are attracted to both line defects, and so each line defect grows at a slower rate because they are in competition to attract vacancies (as shown in Figure 6.1). The other end of line 7 is close to a pore, so interaction with these strain fields would further slow lengthening. For this reason, it appears that significant line defect interactions slow the rate of line defect growth, although the relationship remains linear.

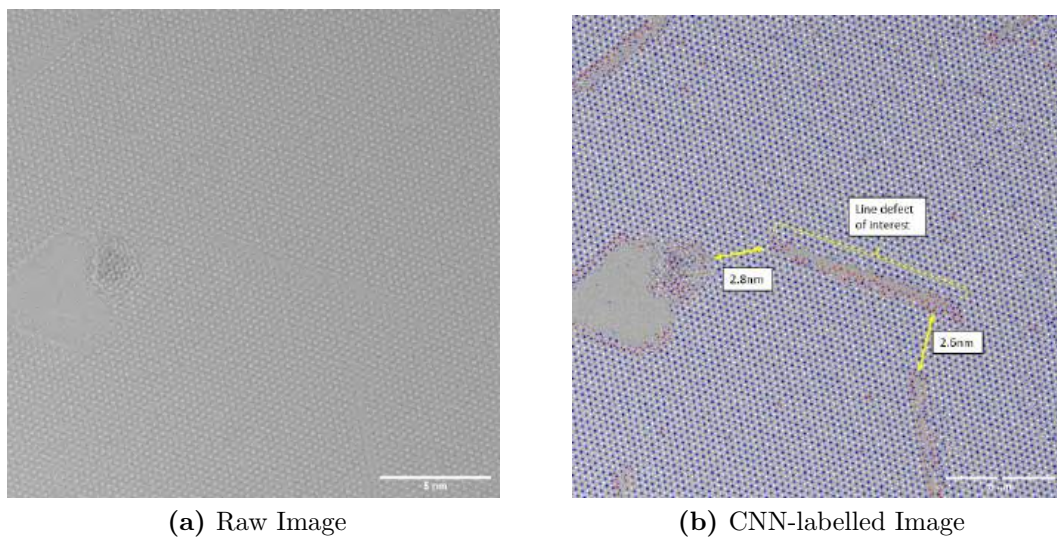


Figure 6.1: The unusually slow rate of this line defect growth (Line 7 in Table 5.1), whilst still linear, is attributed to the proximity of a pore and line defect.

Due to the limited field of view, it was not possible to witness further growth of any line defect greater than 60 nm. At greater lengths, line defects may have facilitated formation of a new grain, inversion domain or a phase transition which could change lengthening behaviour. A change in diffusion mechanism in later stages of line defect growth causing deviation from the observed linearity cannot be ruled out by the results found in this project. However, at 500°C, thermal energy is enough to activate rapid vacancy diffusion. Therefore, any effects of pipe diffusion that might be expected at intermediate temperatures are unlikely to dominate and become a rate-controlling diffusion mechanism.

The observation that line defects grow linearly with time is consistent with the following proposed mechanism for line defect growth: vacancies are produced at a steady rate by sputtering of sulphur atoms via continuous electron irradiation (consistent with findings by Komsa [83]). At 500°C, these vacancies can rapidly diffuse and are attracted to compressive strain fields around line defects. Therefore, line defects lengthen at a steady rate based on the sputtering rate of sulphur vacancies.

6.2 Widening of Line Defects

As found in Section 5.1, the large error in width measurement prohibits any quantitative conclusion about the nature of widening. Despite this, it was observed that the rate of line defect widening was not a continuously increasing quantity and behaved in a step-wise manner. This is likely due to the significant amount of energy required to increase the width of the entire line defect compared to lengthening it. When there is enough excess energy due to lattice strain to overcome the energy barrier, the width of the line defect is expected to increase. A proposed energy profile typical of an Arrhenius relationship is shown in Figure 6.2.

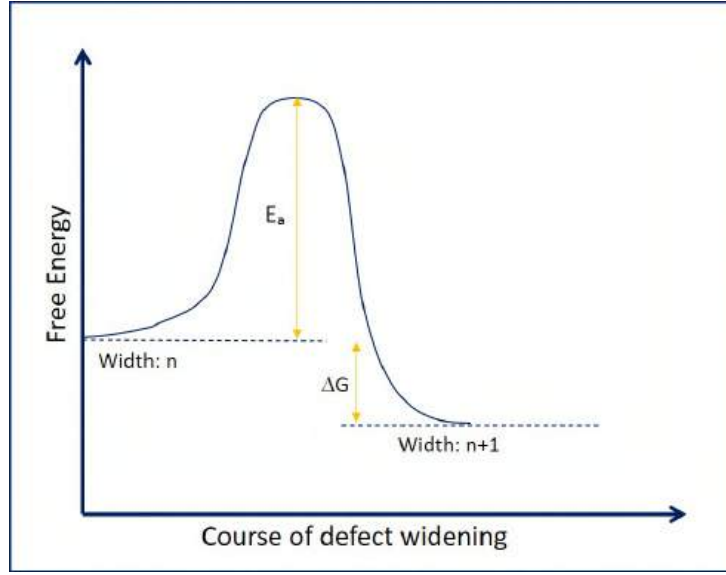


Figure 6.2: A proposed energy profile for widening to explain step-wise growth. ΔG represents the reduction in strain energy as a result of agglomeration of vacancies. E_a is the activation energy required for a widening event to occur.

6.3 Sputtering Cross Section for Sulphur in MoS₂

The experimentally calculated value of sulphur sputtering cross section in Section 5.1.1 is 2.1 (± 0.1) barn and the theoretical value is 0.8 barn [81]. The larger experimental value is consistent with Komsa *et al.*, who measured an experimental value of 1.8 barn [81]. Komsa uses manual labelling from a small dataset with a handful of vacancies to measure this value. The reasonable agreement between Komsa's work and the experimental figures in this study demonstrates the integrity of the CNN's performance, which considers a much larger number of vacancies from many more frames of data. The agreement further supports the conclusion that vacancy generation is the rate controlling factor in line defect growth under the conditions of a crystalline, undamaged lattice. Aside from the possible errors in the CNN (as in Section 5.4.2), other assumptions may explain the discrepancy between the theoretical and experimental values:

- The theoretical value is calculated using the McKinley-Feshbach equation, which requires use of a threshold energy, T_d , calculated with DFT. DFT

calculations are executed at conditions of absolute zero: T_d at 500°C is likely much lower due to increased lattice vibrations from thermal energy.

- The strain fields developed around the line defect are not taken into account in the theoretically calculated value. It is expected that the sputtering cross section is larger in this scenario due to the strain around line defects, which weaken local chemical bonds.

6.4 Observing Strain

Figures 5.6 - 5.7 demonstrate that the CNN is able to detect a displacement and corresponding strain around a line defect from data with low SNR where typical methods used in strain mapping, such as extracting peak intensity positions of atomic columns or Geometric Phase Analysis (GPA), are unhelpful. This highlights the unique ability of the CNN to obtain meaningful insights from lower quality data. The observation of strain is consistent with predictions from Komsa [4] (Figure 5.6 is in reasonable agreement with Figure 3.5) and DFT calculations by Wang *et al.* [41], although a thorough comparison of strain magnitudes has not been carried out.

The maximum strain values found in this work are 10% larger than strain values for dislocations in graphene calculated by Warner *et al.* [84], who found a maximum bond compression or elongation of $\pm 27\%$. This difference in strain could be explained by the lower stiffness of MoS₂ [85].

Huang *et al.* [86] showed that increasing tensile strain acted to linearly decrease the band gap in two-dimensional TMDs. The easier promotion of charge carriers increases metallic behaviour, which is consistent with the metallic nature of line defects. However, the results from this work cannot confirm if the metallic nature of line defects is fully strain-mediated.

6.5 Inversion Domain Detection

Whilst tracking line defect growth, an interesting phenomenon was observed (shown in Figure 6.3). Two line defects at 60° to each other were lengthening. Upon intersecting to form a corner, the line defects disappeared leaving behind a triangular region of a different structure, (shown in Figure 6.3 (d) and 6.4). This structure is metastable as it disappears within 0.125 s. The interaction of non-orthogonal strain fields of the line defects is likely the driving force behind the observed transition.

Initial comparison to literature narrowed the structure down to either an inversion domain (ID), or a phase transformation from 2H to 1T. The latter is a metastable metallic phase of MoS_2 . The conditions under which each structure can favourably form are not yet well-established.

The 2H to 1T phase transition is made energetically feasible by the addition of sulphur vacancies and adsorption of copper. It is then stabilised by dopants [88]. This is not consistent with the conditions presented in the project data, as the sample used was undoped.

IDs are intrinsic defects where the MoS_2 layer changes its orientation through a line defect (as shown in Figure 6.5). The mechanism for formation of the observed structure closely matched that of IDs observed in work by Chen [87] using STEM, which was also done at an elevated temperature, allowing for rapid sulphur vacancy migration. Chen found that reversion to the pristine lattice was possible upon the formation of a pore at the corner of the initial area. Unlike the 1T phase, IDs can easily form in undoped MoS_2 . These behaviours and conditions match what was observed. These similarities have been labelled in Figure 6.3.

Based on its mechanism of formation, it is highly likely that the area observed is an ID. However, several discrepancies point to the need for further investigation. IDs observed by Chen [87] were stable for several minutes despite being obtained at

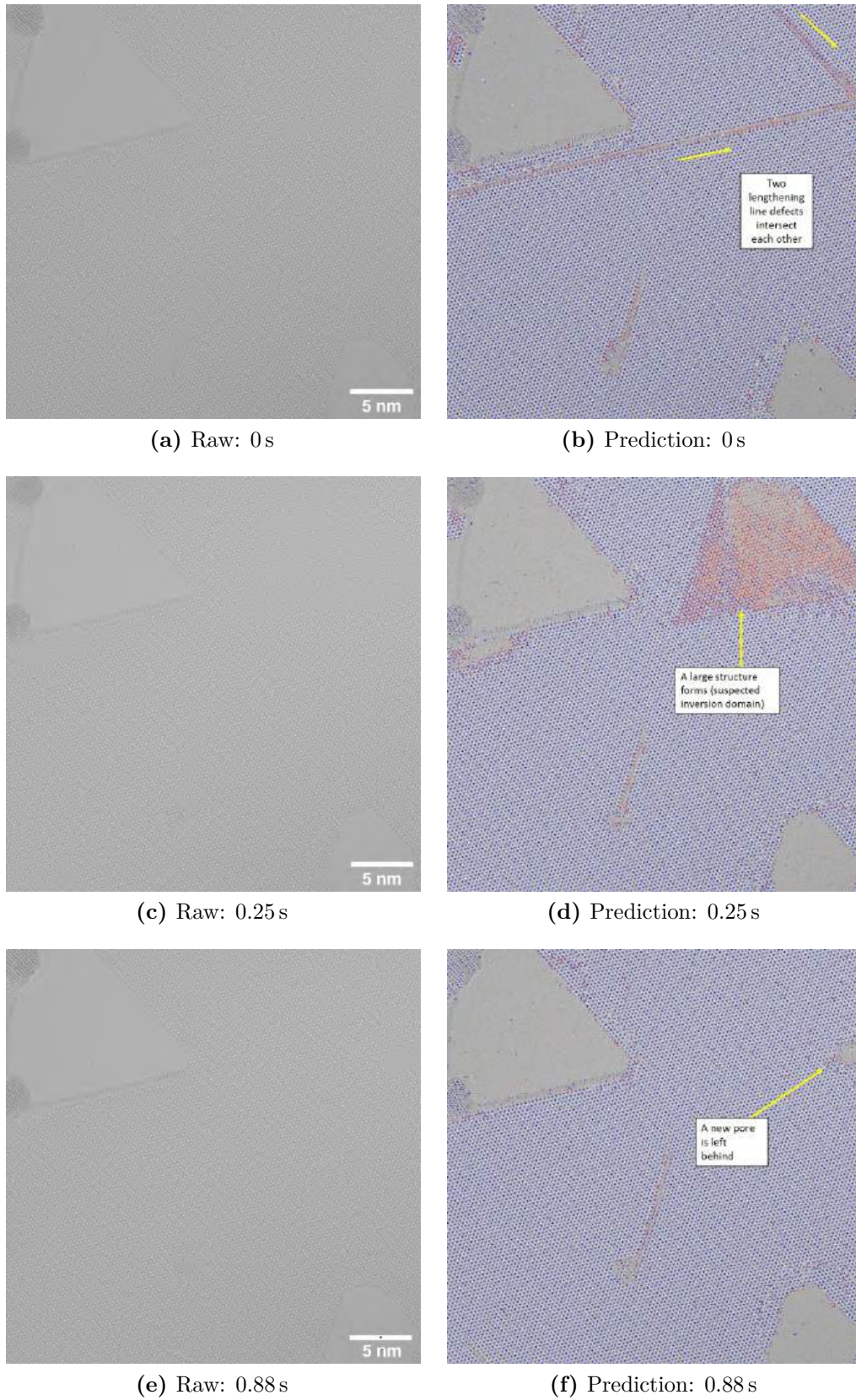


Figure 6.3: Similar behaviour to mechanisms observed by Chen suggest that this is an ID [87].

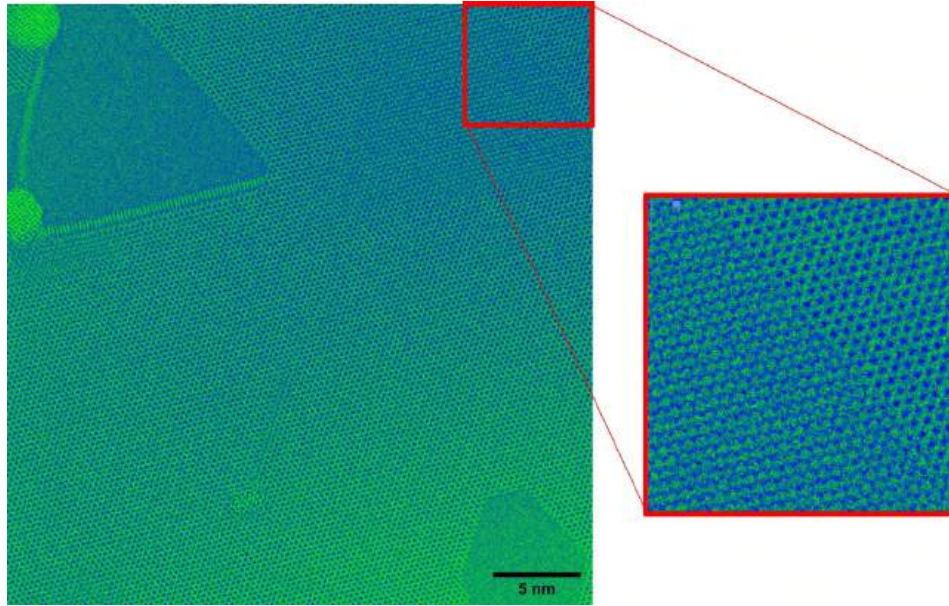


Figure 6.4: False-Colour LUT applied to the raw micrograph to highlight the presence of a triangular area of transformed material.

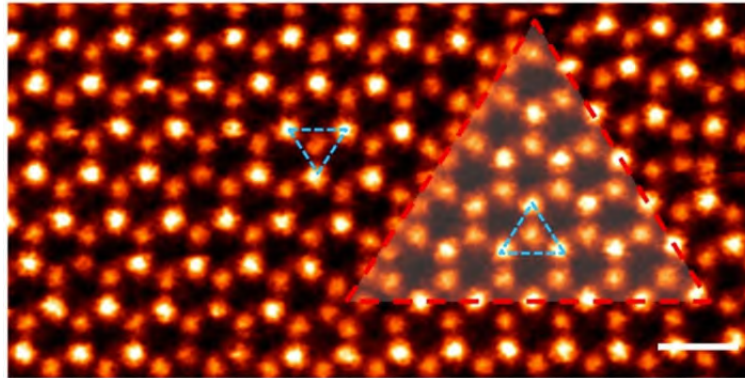


Figure 6.5: STEM image of an inversion domain in MoSe₂ seven atoms across from Lin *et al.* [39] shows a much smaller region than the ID observed in Figure 6.4: possibly the reason for the discrepancy in stability.

a higher temperature of 800°C: 300°C higher than imaging conditions in this work. Work by Lin [39] used STEM to sequentially image the nucleation of IDs which took over 3 s. The comparative instability of the ID in this project may be explained by its abnormally large size. Most IDs observed by Chen [87] were 20 atoms in length whereas this ID is around 40 atoms. A larger area may lead to decreased stability. Unlike this project, neither studies by Lin or Chen used continuous illumination

which may also be crucial to the stability of the ID.

In addition, an atomic contrast shift was observed in the region which may indicate a change in height of atoms. This requires further exploration as a possible vertical change in height may happen simultaneous to the lateral atomic transition. This has not been considered in any studies before.

6.6 Interaction of Line Defects with Pores

In this section, three observed mechanisms involving defect interaction with pores are discussed. Pore formation is energetically favourable because it allows for reduction in strain energy in exchange for an increase in surface energy [38]. Under conditions of electron irradiation, pores are often accompanied by molybdenum clusters because typical electron energies used in the TEM are unable to displace the heavier molybdenum atoms.

6.6.1 Digestion of Line Defect by Pore

The rate of decrease in line defect length shown in Figure 5.3 is $8.6 (\pm 0.3) \text{ nm s}^{-1}$: significantly higher than other line defect growth rates. Sample drift was ruled out by use of a pore also visible in the field of view as reference (Figure 6.6).

Instead, this behaviour might be explained by consideration of the diffusion mechanisms. Similar to a mechanism proposed by Chen *et al.* [38], the line defect from Figure 5.3 is likely being digested by a pore outside the field of view (as shown in Figure 6.7). Sulphur atoms migrate from the pore edge through the fast diffusion channel along the defect line, shortening the line defect and enlargening the pore. In comparison, the growth of a line defect requires diffusion of sulphur vacancies through pristine lattice which has a higher associated migration energy. Therefore, given equal thermal activation, it would be expected that shrinking occurs faster than line defect growth, which would support the results in this work.

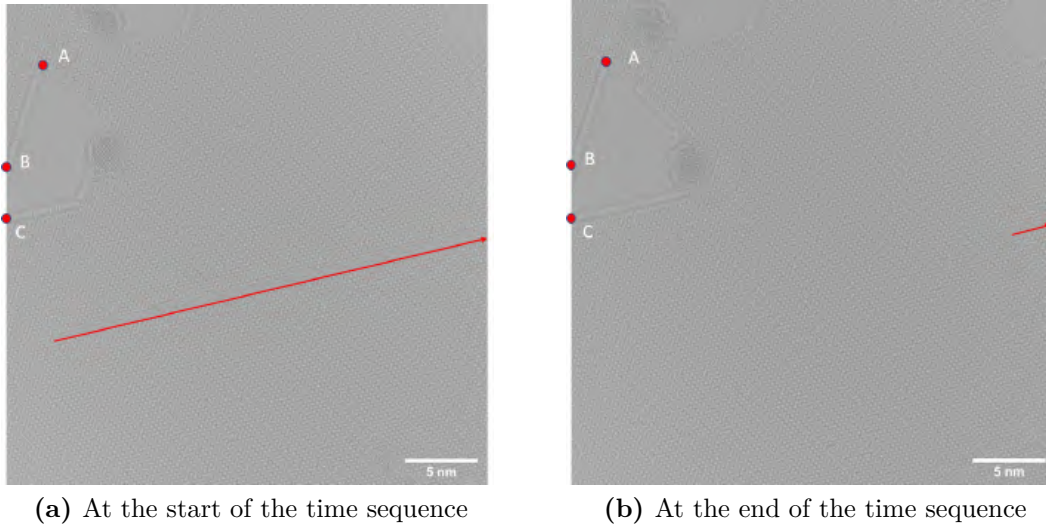


Figure 6.6: Initial coordinates (nm): A(2.54, 4.29), B(0.0, 11.35), C(0.0, 14.79). Final coordinates (nm): A(2.56, 4.32), B(0.0, 11.52), C(0.0, 15.19). The points of reference have not significantly changed, so sample drift is ruled out as an explanation for the apparent shortening of the defect.

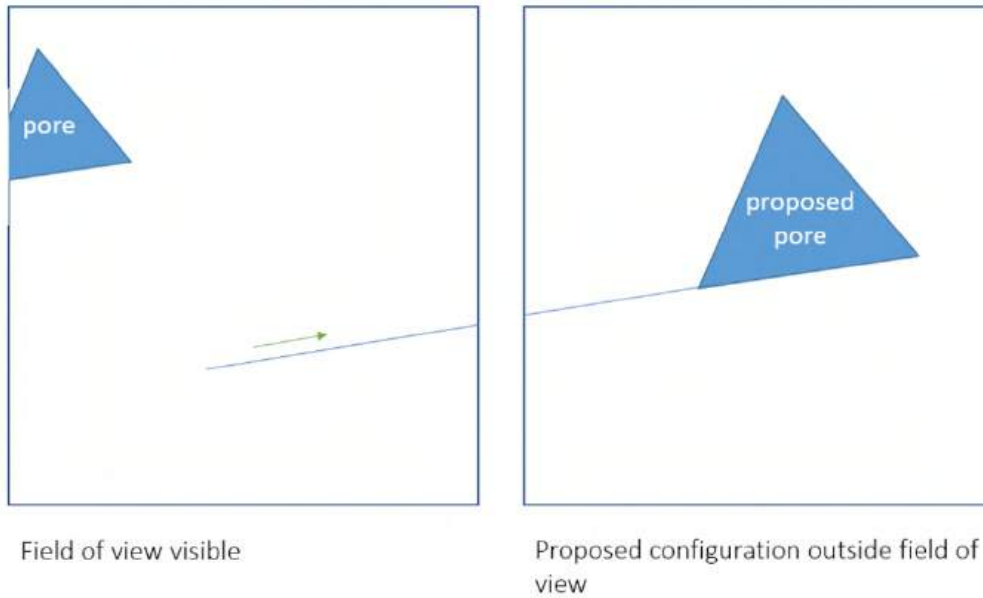


Figure 6.7: A schematic based on Figure 6.6. The 'shrinking' rate of the line defect due to the digestion of line defect by a pore outside the field of view.

6.6.2 Forming MoS Wires at Pore Edges

MoS wires are observed to frequently border pores. Chen [38] observed their formation by gradual absorption of a non-parallel line defect ‘feeding’ into a pore edge. The CNN is able to highlight a new mechanism for MoS wire formation. A line defect parallel to the pore edge migrates towards the pore before widening. It is then absorbed into the pore, leaving behind a MoS wire. This reconstruction is likely driven by the local edge depletion of sulphur resulting from close proximity of the migrating line defect. This allows MoS to be stoichiometrically stable. The formation of the MoS wire is shown in Figure 6.8.

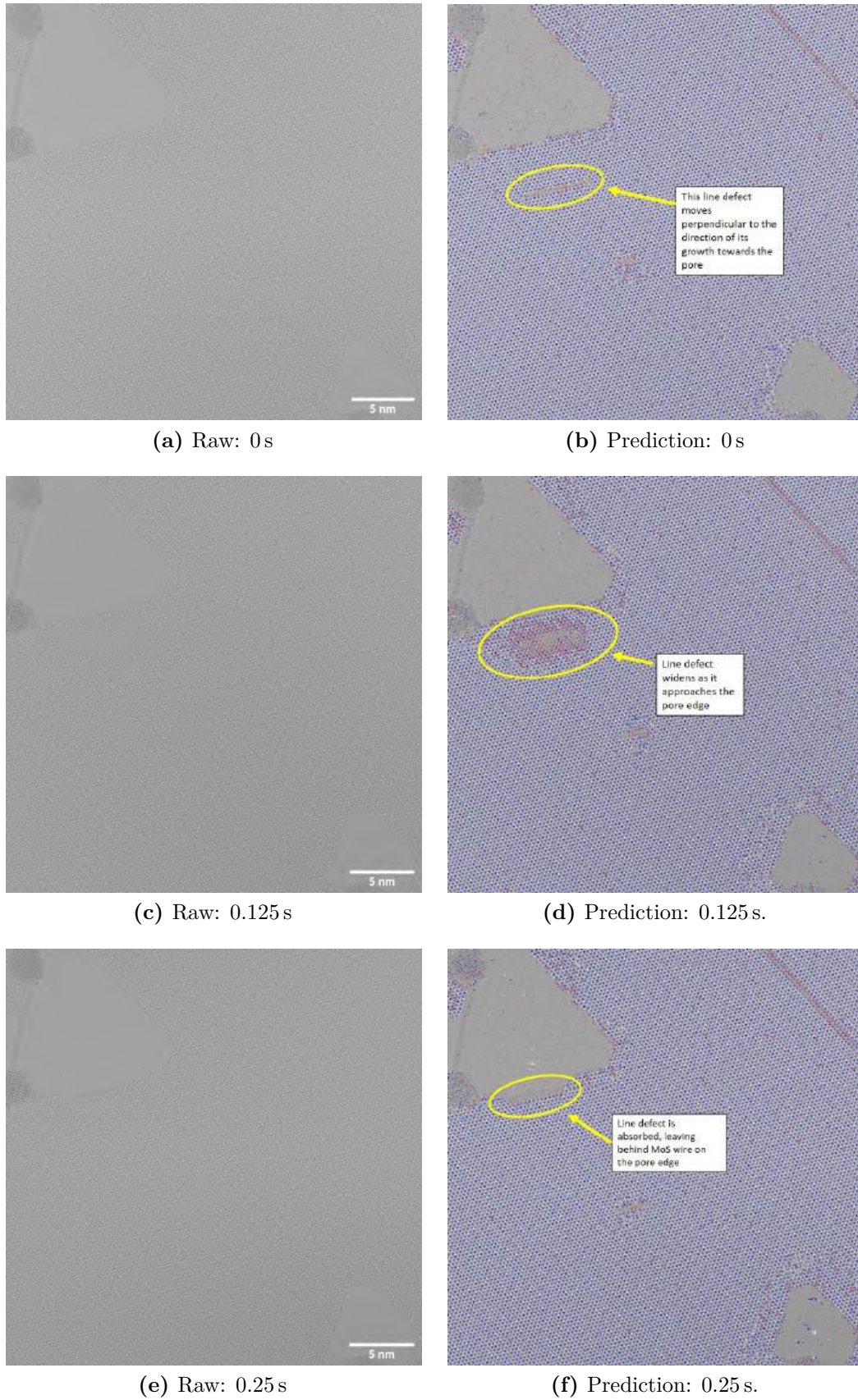


Figure 6.8: Rapid absorption of a line defect to form MoS wires on pore edge.

6.6.3 Molybdenum Clusters at Pore Edges

As a consequence of close analysis of line defect behaviour, other interesting mechanisms were observed: namely the behaviour of Mo clusters. These are much easier to spot by eye than line defects, so the following observations are not extracted by use of the CNN.

One particular molybdenum cluster was observed to have stabilised at the edge of a pore. Further inspection of the area of interest (Figure 6.9) led to the postulation that the cluster underwent an ordering transition. A mechanism to explain this behaviour is proposed: increasing pore size and defect number leads to excessive sulphur depletion eventually leading to the ordering of molybdenum. This would be consistent with observations made by Ryu's work who observe BCC molybdenum clusters at pore edges [89]. However, Wang *et al.* [90] simply refers to these regions as nanocrystalline areas and so further verification of the nature of these molybdenum clusters is required. In addition, the energy required to transition between FCC and BCC is large: a twinning from FCC to HCP could be more likely. However, there is not enough evidence to support either theory from this project.

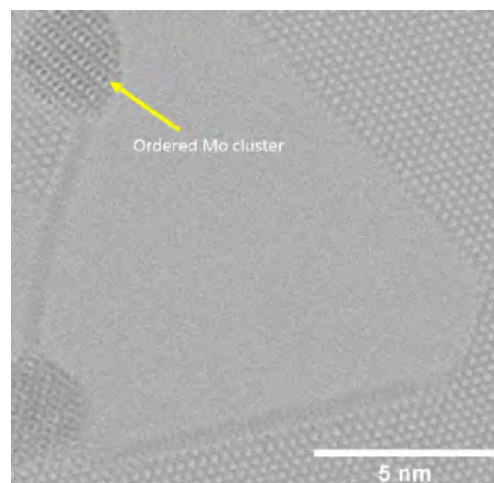


Figure 6.9: Two molybdenum clusters at a pore edge. The top cluster has a greater degree of order but its structure is not determinable from this image.

6.7 Effect of Dose and Dose Rate

Figure 5.10 indicates that the dose rate has no effect on the extent of damage to the material in the range $8539 - 56705 \text{ electrons } \text{\AA}^{-2} \text{ s}^{-1}$. This implies that within this range, the time over which damage is done is not an important factor in the extent of damage that occurs. Therefore, if the same samples at lower fluxes are left for longer until they receive the same accumulated dose, it would be expected that total damage was similar. The effects of dose rate and cumulative dose have been disputed in several studies across a wide range of material systems. Findings from Egerton *et al.* [35] are consistent with the findings from this project: accumulated dose is proportional to the extent of damage, rather than dose rate.

However, the existence of any dose rate effect cannot be ruled out by this piece of work because the dose rates explored may not have been low enough to investigate the existence of a critical dose rate. This phenomena is observed in graphene by Robertson [32] and in CeO_2 by Johnston-Peck [91].

6.8 Effect of Defect Density

Figure 5.8 shows data in which highly damaged lattices did not display any increase in sulphur vacancy generation, which indicates an effect of defect density on the extent of damage produced. This is also consistent with other trends from data which had lower initial defect densities: Figure 5.11 shows that vacancy production slows down with increasing defect density.

A decrease in vacancy production might suggest a decrease in sputtering cross section. However, the sputtering cross section of each atom should not be affected by the number of surrounding defects.

Upon using the CNN to examine the experimental images closely, a model to explain the effects of high defect density is proposed: the decrease in vacancy generation coincides with the intersection of the growing line defects. This intersection partially cancels out the strain fields at line defect tips and therefore stunts line defect growth. Instead, any vacancies formed are more likely to be absorbed into surrounding amorphous regions characteristic of Dataset B, so are not detected by the CNN. Furthermore, the increased number of line defects eventually feed into the amorphous region and set up channels for sulphur vacancy diffusion to these regions. This leads to a perceived decrease in the rate of vacancy generation seen in Figure 5.11 because the methods used purposefully exclude amorphous regions to minimise false positive CNN predictions. In addition, non-parallel line defects eventually intersect, creating new pores which absorb line defects: again leading to a decrease in the rate of detected vacancies.

Alternatively, the behaviour could be due to a self-healing mechanism, similar to self-healing Stone-Wales defects observed in graphene [92]. Sputtered sulphur atoms may have enough thermal energy at the experimental temperature to re-fill any sulphur vacancy sites. The data from this project is not able to confirm this theory: a new experiment varying temperature would be required for conclusive evidence of this mechanism.

The final explanation for this observed behaviour could be due to the failure of the CNN. This behaviour is most prominent in data collected at the lowest dose rates, which would have the lowest SNR. Such high levels of noise in the data could lead to failure of the CNN to accurately label defects: vacancies might be falsely observed everywhere. It is hard to verify this by eye due to high levels of noise.

Chen *et al.* observed [38] that the thermally-enabled rapid migration of sulphur vacancies resulted in longer line defects, whilst low mobility vacancies at room temperature resulted in many shorter defects as shown in Figure 6.10. However, the

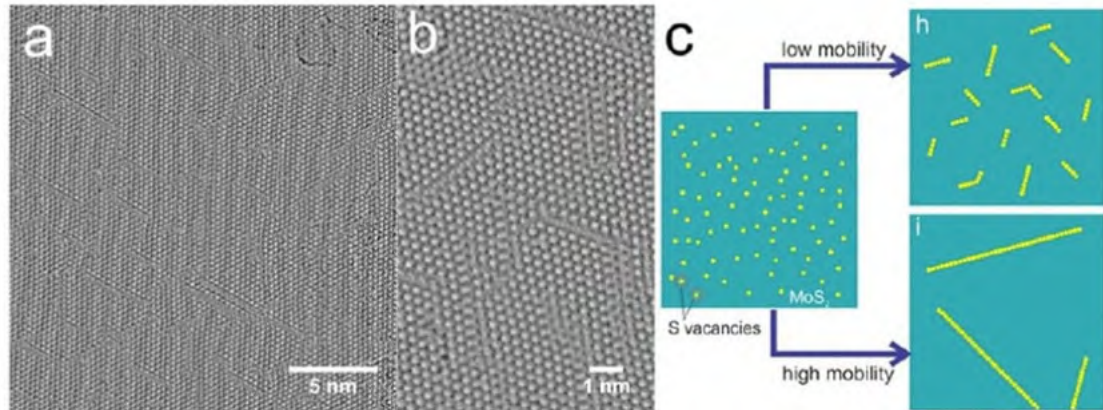


Figure 6.10: High and low sulphur vacancy mobility may not be the only factor controlling the length of line defects grown, unlike what is implied by Chen (figure reproduced from [38]).

results in this work (as shown in Figure 6.11) suggest that temperature is not the only factor controlling the mobility and therefore length distribution of line defects. In Dataset B, many short 5 nm defects were observed despite being at an elevated temperature. This was exclusively observed in areas with minimal pristine lattice available (around 700 nm²), surrounded by amorphous regions. Therefore, the lack of long-range crystallinity appears to have large effects on line defect growth. This is likely because local disorder may encourage the tolerance of greater strain in the lattice, in addition to providing more nucleation points.

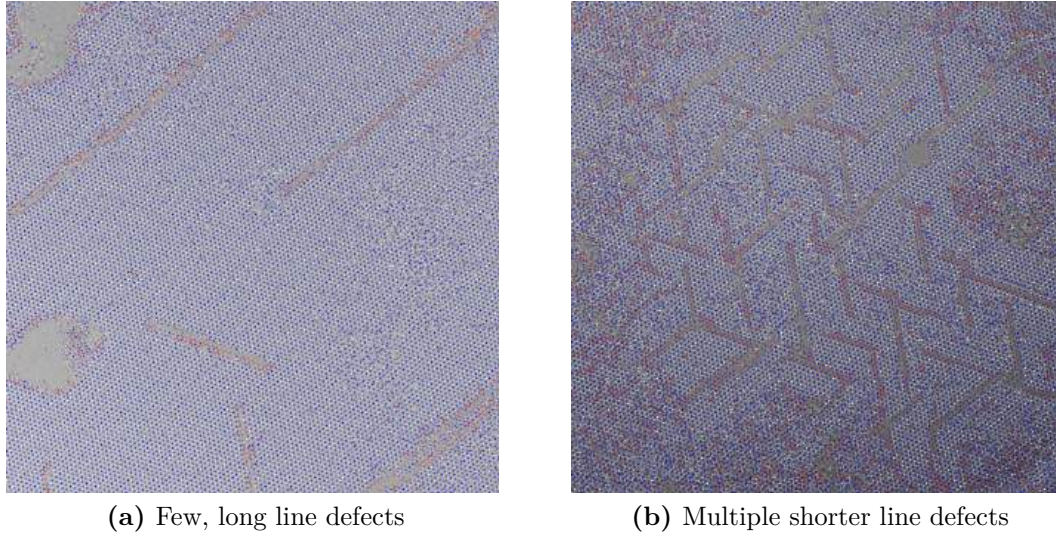


Figure 6.11: Both these line defect structures have grown under high sulphur vacancy mobility.

6.9 Novelty of Method

The novelty of this work comes from the sequential analysis of multiple frames of data, and the development of a line defect tracking methodology. This has enabled visualisation of defect dynamics at a time resolution not previously possible. Previous literature has been able to analyse TMDs without the use of machine learning models but only assess a handful of individual frames of data. Whilst this allows for high exposure times and therefore an image with higher SNR easily labelled by eye, any sequential data considered was of small sample sizes of up to 4 frames. In contrast, the CNN has been able to meaningfully label over 4000 frames to visualise defect dynamics.

The time taken by the CNN to generate predictions for one electron micrograph was 5 seconds. The time taken for a human to manually label the same image was over 25 minutes: 300 times longer. Although the expert human eye may be able to provide a slightly higher degree of confidence, the CNN proved to have a high accuracy in comparison to human labelling and also exhibited the ability to spot features that may have been missed by a human, such as new phases and strain.

6.10 Limitations

There are several areas in this project which could be improved.

1. The likeness of simulated and experimental data could be further improved to train a better performing CNN. In particular, the simplicity of the model of MoS₂ defects which were used to create the simulated training data may have hindered the ability of the CNN to extract more nuanced atomic arrangements. For example, strain around the defects has not been modelled.
2. This project only used one characterisation technique to explore MoS₂: the only experimental data available was in the form of images. The use of the developed methodology in tandem with other techniques, such as ADF-STEM or electron energy loss spectroscopy (EELS), may be able to provide a clearer explanation for behaviour observed.
3. The work-flow has an inherently cyclical nature. The atomic models of line defects are based on assumptions about the defects that have been observed empirically, which lack an accurate statistical characterisation of the defects. Therefore, there is inevitable bias in the training data.

6.11 Summary

The output of the CNN was used to measure the growth of line defects and to quantify how vacancy generation is affected by electron dose and dose rate. In addition to individual defect evolution, the CNN was able to highlight more general defect interactions. The CNN's ability to extrapolate is likely due to the generalisable nature of deep-learning models.

7

Future Work

Future work could be carried out to further refine models describing the observed behaviour of defects in MoS_2 . In particular:

1. Strain mapping of several line defects and the use of *ab initio* anisotropic elasticity theory would be a worthwhile investigation to explore how strain varies as a function of line defect length and width.
2. Varying the temperature of the experiment will explore the possibility that defects may self-heal at higher temperatures, similar to the healing of the Stone-Wales defect in graphene [92].
3. Varying the acceleration voltage of the electrons used in the TEM could further explore the damage mechanism. Graphene displays a critical voltage of 60 kV below which damage is scarce. It would be interesting to see if similar behaviour is displayed by MoS_2 .
4. Varying the dose and dose rate less coarsely and at a larger range will investigate whether dose rate has any effect at a low enough rate. However, a

lower dose rate may require caution due to a decrease in SNR and therefore a less reliable CNN.

5. This project has created a tool in which defect interactions can be easily highlighted. The collection of more data would allow for more frequent observation of defect mechanisms. An in depth statistical analysis on defect dynamics could be carried out to further current understanding.

8

Conclusion

The main aim of this work was to develop a method to extract quantitative insight into defect behaviour in MoS₂ from HRTEM data. A new model for defective MoS₂ was created and implemented in the training of a CNN. This performs to an experimental accuracy of 82%. The CNN was applied to experimental data and a post-prediction method for data analysis was researched, developed, and implemented. This resulted in the creation of line defect tracking software which measures the length of line defects to within 2.6% of a trained human. Applying the developed methods revealed many interesting scientific insights. Notably, it has been shown that the nature of line defect growth is linear (between 5 nm – 60 nm), which suggests that the rate of sulphur sputtering controls growth. A strain field around the line defect was quantified, with maximum bond compression or elongation of $\pm 40\%$ on top of a maximum shear strain of 47%. In addition, the results show that the effect of accumulated dose correlates to the extent of damage up to a defect density of around 4 sulphur vacancies nm⁻² for dose rates above 8539 electrons Å⁻² s⁻¹. No dose rate dependence was found. These results demonstrate the unique ability of machine learning to extract quantifiable insights from low quality HRTEM data.

9

Ethics and Sustainability

Contents

9.1	The Benefits of Using MoS ₂	82
9.2	Industrial Production of MoS ₂	82
9.3	Sustainability of MoS ₂ -based Solar Cells	83
9.4	Project Specific Considerations	84

In this chapter, the positive and negative sustainability and ethical implications of using MoS₂ are examined. Subsequently, the impact of the methods used in this specific project are considered.

9.1 The Benefits of Using MoS₂

The main motivation of this work is to provide an understanding of defect behaviour in monolayer MoS₂ so that its electronic properties can be exploited for the next generation of electronic devices. As mentioned in Chapter 2, this understanding enables the use of MoS₂ in several applications, for example, for use in solar cells and batteries. Aside from these uses, MoS₂ is a promising candidate for a large range of different applications including photodetectors (used in optoelectronic circuits, spectroscopy, and biomedical imaging [93]), and transistors [14]. With such wide scope for application, MoS₂ is a material worthwhile investigating especially due to its potential to have a large impact on sustainability goals in the future.

9.2 Industrial Production of MoS₂

Despite the large number of possible uses of monolayer MoS₂, it is not widely produced in its pure, crystalline form. Therefore, its synthesis does not yet have economies of scale. However, molybdenite (the mineral from which MoS₂ is mined) is not scarce, so MoS₂ has the potential to be much more widely used if refinement processes are developed and scaled. In addition, there is potential for the processing of monolayer MoS₂ to be integrated with existing industrial processes. This is because molybdenite is a by-product of copper mining, which is hugely popular; over 20000 metric tonnes of copper were mined in 2020 [94]. However, ethical concerns in the mining industry cannot be overlooked, with 267 alleged human rights abuses in the past 10 years [95].

Monolayer MoS₂ can be refined from molybdenite via several steps involving crushing, ball-milling, flotation, exfoliation and centrifugation [96]. The MoS₂

formed from this lab-based process currently has a 92% purity. In an industrial context, MoS₂ is produced at 85% purity for use in bulk powder form as a lubricant [97], although this purity is too low for its use in electronic devices. A promising route for cheaper manufacturing of monolayer MoS₂ is with use of scotch tape, using the same micromechanical cleavage technique as in graphene manufacturing [98, 99]. In summary, more downstream development would be required to scale up production of MoS₂ for feasible commercial use.

9.3 Sustainability of MoS₂-based Solar Cells

This subsection focusses on the sustainability of solar cells, which are a specific application of MoS₂. Currently, 95% of solar panels are silicon wafer based [100]. Barriers to widespread production are similar for silicon and MoS₂, which both require carefully controlled and expensive processes to make defect-free materials [101]. Despite this, the energy density of the MoS₂ layer far exceeds that of silicon, which has several implications. Silicon is extracted from quartz: the production of quartz requires heating and therefore greenhouse gas production. Use of MoS₂ will decrease the volume of material required to produce a solar panel with the same power output as a silicon-based panel. In addition, this unlocks the potential for ultrathin, flexible, and transparent solar devices. This would allow for more widespread use in both developed and developing countries. Solar panels are a key enabler for remote communities in developing countries which do not have the infrastructure to connect to the grid and have enormous positive social impact.

The largest sustainability concerns for solar panels arise from their manufacturing and recycling. Solar panel production produces toxic chemicals such as silicon tetrachloride, which leads to the production of harmful air pollutants [102]. Furthermore, many countries lack the infrastructure required to recycle solar panels, with the International Renewable Energy Agency projecting over 80 million tonnes of solar panel waste by 2050 [103].

9.4 Project Specific Considerations

The energy required to train a NN differs by several orders of magnitude, depending on its size, as shown for natural language processing networks in Figure 9.1. The NN architecture used for this purpose is much smaller than those shown in Figure 9.1, with only 2 million parameters. Based on this, it is estimated that energy spent training the NN in this project was less than 5 kWh in total. In addition, the focus of the research is to enhance current scientific understanding of line defect dynamics, rather than to refine the current understanding of NNs. As a result, no unnecessary training was carried out. The majority of the energy expended from activities requiring high computing power is used to cool the machines. Therefore, there are ways that this energy cost could be lowered; for example by building computer centres in colder countries where cooling costs are much lower [104]. Combined with cloud technology, the outsourcing of computing power to remote centres in cooler countries, which are able to source any needed energy renewably, is promising. The energy produced by a set of typical south-facing solar panels in the UK in one day is able to train the NN in this project two times [105]: the benefits of the research far outweigh the costs of NN training.

AI is often the topic of ethical discussions which question how reliable a machine's decision might be. However, the use of a NN in this application is purely designed to aid a human investigation. It is only applicable to a niche scientific context and is not involved in making any major decisions that could directly impact a person's wellbeing. Guidelines for AI published by the European Union categorise different AIs based on their deemed risk: the AI involved with this project falls into their least severe category which will not require any regulation [107].

This project has also demonstrated the feasibility of using machine learning techniques. The workflow that was developed can easily be generalised to process data from other similar materials which might also be of interest. The increased use

	Date of original paper	Energy consumption (kWh)	Carbon footprint (lbs of CO ₂ e)	Cloud compute cost (USD)
Transformer (65M parameters)	Jun, 2017	27	26	\$41-\$140
Transformer (213M parameters)	Jun, 2017	201	192	\$289-\$981
ELMo	Feb, 2018	275	262	\$433-\$1,472
BERT (110M parameters)	Oct, 2018	1,507	1,438	\$3,751-\$12,571
Transformer (213M parameters) w/ neural architecture search	Jan, 2019	656,347	626,155	\$942,973-\$3,201,722
GPT-2	Feb, 2019	-	-	\$12,902-\$43,008

Figure 9.1: A table showing the energy required to train natural language processing NNs with varying numbers of parameters [106].

of computation to process experimental data could increase efficiency of scientific research; having an overall positive impact in the wider materials science community.

10

Project Management

Contents

10.1 Initial Objectives and Subsequent Modifications	87
10.2 Resource Management	89
10.3 Assessing and Mitigating Project Risks	91
10.4 Conclusion	92

10.1 Initial Objectives and Subsequent Modifications

The initial plan for the project (as shown in Figure 10.1) was to develop methods to investigate the behaviour of line defects in MoS_2 using machine learning. The goals of the project crystallised over time as I researched the literature and discussed ideas with Dr. Huang. One of the first priorities of the project was to learn about and reproduce methods used by the previous Part II student. This was crucial to understanding the scope of the project and successfully gauge what tasks would take up the most time. This initial objective involved:

- Conduct a literature review on the subject of defects in MoS_2 and the fundamentals of machine learning.
- Learn to use MULTEM simulation software.
- Learn about CNNs and the use of TensorFlow (the Python framework used to build a neural network).
- Organise the existing code from the previous Part II student so that it is easily reusable.

Any experimental component of the project was eliminated due to the pandemic. All computer-based skills were self-taught. I learnt to use MULTEM by reading the manual and looking at example code included in the software. In addition, TensorFlow is very well documented and many online tutorials helped with familiarisation. I received full access to the work of the previous Part II student in the first week of December 2020 (due to practical challenges locating where the files were stored following the sudden nature of the March 2020 lock-down [108]). I used the time prior to this reading literature. Once I was given access to the files, I was able to rapidly meet my initial objectives. By the end of Michaelmas Term, I was familiar with all prior work and was ready to move the investigation forward. In Hilary, I focussed on delivering the following objectives:

- Develop a method to extract quantitative information from the images generated by the CNN.
- Create a method to evaluate the success of the network.

I had free reign over how best to tackle data analysis. To approach this task, I used the highest quality data to develop my method. The success of using a Hough Transform was a breakthrough after which I spent four weeks confirming this was a viable and generalisable approach. In this time, I developed software to track line defects in my data. By mid-Hilary I had optimised the set-up of my method for large-scale data processing.

When developing the data analysis methods, an agile approach common to software development was used. This worked well and suited attempts to improve the CNN's performance. Midway through Hilary Term, after extensive data analysis, the decision was taken to go back and retrain the neural network to improve data quality downstream. The initial model of MoS₂ was changed to emphasise the existence of multi-width line defects and pores. Simulated data was re-generated. This task took an extra three weeks, but was important to ensure the accuracy of the network was maximised and hence increased the reliability of extracted results. Data analysis continually led to new research opportunities: some of which could be pursued within a sensible time-frame. For example, whilst investigating the degree to which the neural network successfully predicted atomic placing, it became clear that a strain analysis was an unplanned possibility.

In the last week of April 2021, easing pandemic restrictions led to an opportunity to obtain new data for the first time. Given the knowledge of this possibility, I had designed an experiment which would provide data for the investigation of the effect of dose rate on line defect growth. However, the pandemic restricted the synthesis of any new samples for the purpose of this experiment. During data acquisition it was revealed that the sample used was quite damaged. This catalysed



Figure 10.1: Gantt Chart showing the project execution plan

a shift in focus to the behaviour of vacancy production more generally. Analysis of the new data yielded interesting results. From the sample, I discovered an interesting effect caused by defect density: a variable I had not initially considered. Based on this, final objectives were set:

1. Investigate effects of cumulative dose and dose rate.
2. Investigate effects of defect density on the rate of vacancy generation.

10.2 Resource Management

The biggest challenge of this project was to work in an entirely remotely condition away from my supervisors or any members of the group. This removed any opportunity for casual, ad-hoc discussion to bounce off ideas which might have been valuable. I worked independently on a set of experimental data which was collected before the pandemic in March 2020 and passed on to me. In addition, there was limited access to any study space. The library was open only six hours per day from April 2021 when restrictions began to ease. Careful time and resource management

08:00					
	Morning Walk	Morning Walk	Morning Walk	Morning Walk	Morning Walk
09:00	09:00 Write aims and pla...	09:00 Literature Research: MoS2 properties	09:00 Literature Research: multislice calculations	09:00 Review tasks left f...	09:00 Sit-in on Pete Nellist's group meeting: make notes on interestin...
10:00	10:00 Teach myself MULTEM using the manual			10:00 Literature Research: focus on defects in MoS2	
11:00	11:30 Create atomic coo...	11:00 Brainstorm ways to model defects using code in MoS2	11:00 Teach myself how to change MULTEM simulation parame...		11:00 Weekly Check-in with Chen
12:00				12:00 Lunch	
13:00	12:30 Lunch	12:30 Lunch	12:30 Lunch	13:00 Angus' Group Mee...	12:30 Lunch
14:00	13:30 Coding perfect MoS2 lattice	13:30 Coding defective MoS2 lattice: single vacancies	13:30 Analyse experimental images	14:00 Coding defective MoS2 lattice: multiple vacancy lines	13:30 Literature Researc...
15:00					14:30 Upload code written this week to github and organise folders
16:00	15:30 Trial run MULTEM with my coordinates	15:30 Run a minibatch of MULTEM to test my code	15:30 Coding defective MoS2 lattice: single vacancy lines		16:00 Set MULTEM simul...
17:00				16:30 Prepare slides for...	Assess week's pro...
18:00					

Figure 10.2: An example of a weekly plan, taken from December 2020. All events were remotely attended.

was required to maximise my efficiency in these challenging work conditions.

1.5 hours each week were put aside to reporting progress and seeking guidance from Dr. Huang. Meetings with Prof. Kirkland happened twice a term, in which broader advice with regards to project direction was given. The lack of human contact meant that some problems which might have taken a few minutes to solve took several days for me to work out independently. Without the structure of working in a lab, a strict working schedule was implemented and frequent self-review helped me to focus. Online resources and tutorials were also invaluable to my progress. An example weekly plan is shown in Figure 10.2.

The graphical user interface (GUI) to the remote computer suffered from a lag, so a SSH connection was set up such that all coding could be done without the use of the GUI. Having had minimal exposure to MATLAB (which was required for

running MULTEM simulations), their documentation was hugely useful in picking up the basics. Mendeley Reference Manager was used to keep a record of relevant literature and my annotations on each paper. Fortnightly meetings with the group were interesting and useful sessions for me to hear about other areas of research. I also had the opportunity to present my work in March 2021, which was very helpful in highlighting new avenues of interest. I tried to understand the work of all the group members, but having never met them other than in a large virtual meeting, it was difficult to fully make use of this resource and regular communication was hard due to lack of informal contact opportunities.

10.3 Assessing and Mitigating Project Risks

The risks associated with this project can be grouped into four main areas. Active measures were taken to mitigate these risks.

Firstly, all the project work took place via a remote connection to the group computer and was therefore susceptible to the connection crashing. Not being in the lab in person meant any hard restart was not possible. This would suspend access to all data and computing power. Most group members were based at ePSIC (Electron Physical Sciences Imaging Centre) in Harwell and not able to help as the computer was physically based in central Oxford. Regular contact with people on-site allowed me to ask for a manual reset of the computer if necessary. Due to network instability, the remote connection was down for a total of 11 working days between January and April 2021. Regular contact with Kevin Treder, a DPhil student, allowed for swift communication whenever the server crashed. Work on the literature review was carried out in this time.

Secondly, the pandemic restrictions introduced uncertainty with regards to if/when new experimental data could be obtained. This made the project harder

to plan. To mitigate the impact of the lack of new data, the project focussed on developing methods to analyse pre-existing data, rather than the acquisition of new data. No new data was acquired until 18th April, 7 weeks before the end of the project. Knowing that this was a possibility, time was dedicated to writing as much of my thesis as possible before April to allow for in-depth analysis of new data and any possible new investigation in the late stages of the project.

Thirdly, the loss of software would have a high impact on the project. To mitigate this, Github was used to back up all code and manage different versions. Code written can be found at <https://github.com/helenwl/Part2Project>. This clear documentation will hopefully enable straightforward continuation of my work in the group.

Finally, the GPU cluster used to execute all the code was a limited and shared resource used by one other member of the group. In order to avoid clashes, a spreadsheet with a schedule was used to keep track of computing demand. In addition, small-scale dry runs of any large jobs were conducted to prevent wasting of valuable computing power and time. I planned my work such that longer calculations were run over the weekend to maximise efficiency of my working time. A secondary list of additional tasks was kept in case of any unavoidable clashes.

10.4 Conclusion

Considering the circumstances of the pandemic, management of this project was relatively successful and I am pleased with the extent to which the original objectives were met.

11

Health, Safety and Risk Assessment

Despite working with experimental data, the lack of any in-person component in this project meant risk from handling hazardous chemicals or using any complex equipment was minimal. The main risk to health and safety comes from the workstation set-up because all the work is carried out using a digital display. Working from home meant that it was difficult to achieve the same ergonomic stability that using an office chair and desk would allow. However, several measures were taken to ensure best ergonomics given the lack of office equipment in the home environment. For example, a cushion was used for back support and books were used to prop up any display screens such that they met eye level. This minimised poor posture which would lead to back and neck pain. Short breaks away from the screen were taken every hour to minimise eye strain. During writing of the thesis, a copy of the report was printed out each week to minimise screen-time. In addition, a range of exercises recommended by the UK Government's Health and Safety Report were done once a day. These exercises aim to reduce musculo-skeletal discomfort for people doing static work [109].

Aside from risks to physical health, the risk to mental health was large due to the isolated nature of working remotely. Whenever possible, library spaces were used to ensure some degree of social interaction each day and the implementation of a strict working schedule was vital to ensuring a degree of separation between research and free time.

Appendices

A

Appendix

A.1 Creating Model $X_{\text{defective}}$

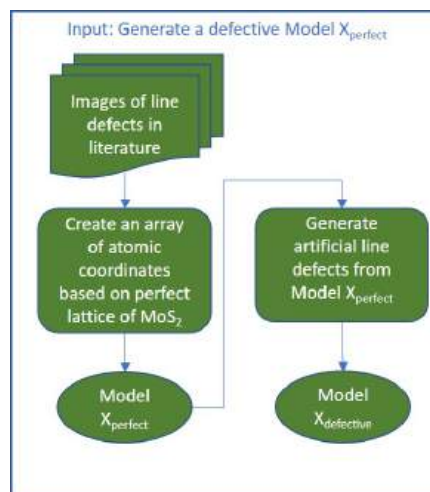


Figure A.1: Summary of steps to generate Model X defective, created by Lear 2020 [24]

A.2 Applying the Convolutional Neural Network to Experimental Data

The experimental image is 4096 pixels x 4096 pixels, which is too large to feed directly into the neural network without the loss of information. Whilst there are neural networks which would be able to process this, they are bulkier and involve more layers which would take more computing power. Therefore, each experimental image was split up into a 3 x 3 grid, and 9 images were individually fed into the network for inference before being stitched back together post-prediction. This slicing is very similar to methods also used by *Groschner et al* [72] to reduce computational demand.

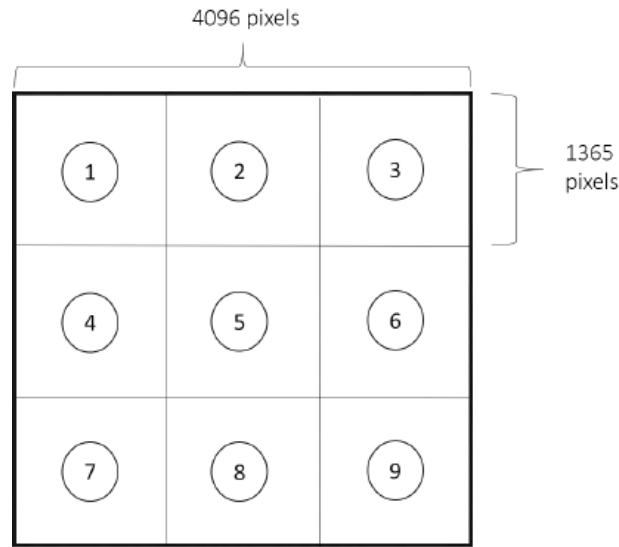


Figure A.2: Feeding experimental data to the CNN without compressing the image required splitting it into 9 smaller images.

B

Appendix

B.1 Calibrating HRTEM images

The length in pixels of one bond length was measured and compared to the theoretical bond-length value. In practice this was done by measuring between 20 atoms (and dividing by 20) in order to minimise the human error. 5 separate measurements were made per image and the average value was taken. The absolute human error on any line measurement was estimated to be ± 20 pixels. Therefore, 1 pixel was found to correspond to 8.18 ± 0.6 pm. Based on this conversion, the error on each human measurement in imageJ is ± 1.6 Å.

This calibration assumes an entirely flat MoS₂ sample. Whilst this is a reasonable assumption to make, any slight tilting in the sample is a source for error in this calibration value. Using trigonometry and assuming a generous maximum tilt of 0.5° , the maximum likely error due to the tilt was calculated to be 3 pm. This is much smaller compared to other errors introduced in the methodology and so is

negligible.

$$\begin{aligned}
 \text{Error due to sample tilt} &= \frac{B - A}{B} \\
 &= 1 - \cos(0.5) \\
 &= 3.8 \times 10^{-3}\%
 \end{aligned}$$

where $B = 3.19 \text{ \AA}$, and $A = B\cos(0.5)$.

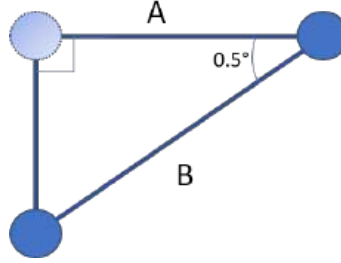


Figure B.1: The error in calibration if the sample was titled is negligible.

B.2 Calculating Dose Rate in Dataset A

The dose rate can be calculated from mean counts values from a micrograph.

The number of electrons per pixel is given by:

$$\text{Electrons per pixel} = \frac{\text{Mean Count}}{\text{Gain}} \quad (\text{B.1})$$

where:

- Gain (constant machine-calibrated value) = 66, i.e. 66 counts is equivalent to one electron
- Mean count = average value of each pixel in the image of interest

For example, for Dataset A, the mean counts value was 1744.

$$\text{Electrons per pixel} = \frac{1744}{66} = 25.6 \quad (\text{B.2})$$

From the calibration of HRTEM images, the scale of each pixel was found to be:

$$1 \text{ pixel length} = 0.08176 \text{ \AA}$$

$$1 \text{ pixel area} = 6.68 \cdot 10^{-3} \text{ \AA}^2 \quad (\text{B.3})$$

$$\begin{aligned} \text{Dose per image} &= \frac{\text{number of electrons per pixel}}{\text{area of one pixel}} \\ &= \frac{25.6 \text{ electrons per pixel}}{6.68 \cdot 10^{-3} \text{ \AA}^2} \\ &= 3939 \text{ electrons \AA}^{-2} \end{aligned}$$

Given that exposure time per frame = 0.125 s, this gives:

$$\text{Flux in Dataset A} = 30715 \text{ electrons \AA}^{-2} \text{s}^{-1}$$

B.3 Calculating the Number of Sulphur Atoms per \AA^2

The number of sulphur atoms per \AA^2 was found in order to calculate the experimental sputtering cross section of sulphur. Figure B.2 shows the arrangement of the S atoms (the Mo atoms are excluded): there are two layers of sulphur atoms directly on top of each other in monolayer MoS_2 . Each sulphur at the unit cell corners represents one third of an atom. The total number of sulphur atoms per unit cell is therefore $\frac{8}{3}$.

Using Pythagoras: $h = \sin(60) \times 3.19 \text{ \AA}$. The total area of the parallelogram shown in Figure B.2 is $3.19 \text{ \AA} \times \sin(60) \times 3.19 \text{ \AA} = 8.81 \text{ \AA}^2$.

Therefore the number of sulphur atoms per \AA^2 is: $\frac{\frac{8}{3} \text{ atoms}}{8.81 \text{ \AA}^2} = 0.3 \text{ atoms}$.

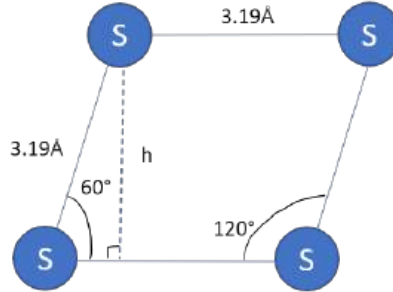


Figure B.2: The unit cell showing only sulphur atoms.

B.4 Statistical Tests

The statistical tests used in this work either reject or accept a null hypothesis based on a p-value. The p-value is the probability of incorrectly rejecting the null hypothesis when it is true.

B.4.1 Grubs Tests

Firstly, the Shapiro-Wilk test was used to ensure that the data was normally distributed. Then Grubs tests (also called the Extreme Studentized Deviate test) were used to identify outliers.

The tests were set up such that for each data point a p-value was returned where:

- H_0 : The value is not an outlier.
- H_1 : The value is an outlier.

The test was conducted at a 95% confidence level such that H_0 is rejected if $p > 0.05$. Line 7 from Table 5.1 returned a p-value of 0.014, so is a statistically significant outlier. The line shown in Figure 5.3 returned a p-value of 0.021, so is also a statistically significant outlier.

B.4.2 χ^2 Test

A χ^2 test was used to determine whether or not there was a statistically significant difference between the performance of a human labeller and the CNN. The test was set up such that:

- H_0 : There is no difference between the values measured by the CNN and the values measured by a human: the observed values should be identical.
- H_1 : There is a difference between the values measured by the CNN and the values measured by a human.

Using the equation:

$$\chi^2 = \sum \frac{(O_i - E_i)^2}{E_i}, \quad (\text{B.4})$$

the p value for a two-tailed test was found to be 0.852. This is well within the bounds of a 95% confidence level (where $p > 0.05$), which confirms that the CNN and manual labelling are not significantly different.

Bibliography

- [1] Sergei V. Kalinin, Andrew R. Lupini, Ondrej Dyck, Stephen Jesse, Maxim Ziatdinov, and Rama K. Vasudevan. Lab on a beam-big data and artificial intelligence in scanning transmission electron microscopy. *MRS Bulletin*, 44:565–575, 7 2019.
- [2] Ian MacLaren, Thomas A. MacGregor, Christopher S. Allen, and Angus I. Kirkland. Detectors-the ongoing revolution in scanning transmission electron microscopy and why this important to material characterization. *APL Materials*, 8:110901, 11 2020.
- [3] Ian J. Johnson, Karen C. Bustillo, Jim Ciston, Eli Dart, Brent R. Draney, Peter Ercius, Erin Fong, Carl R. Grace, John M. Joseph, Jason R. Lee, Andrew M. Minor, Colin Ophus, David E. Skinner, Thorsten Stezelberger, Craig S. Tindall, and Peter Denes. Development of a fast framing detector for electron microscopy. In *2016 IEEE Nuclear Science Symposium, Medical Imaging Conference and Room-Temperature Semiconductor Detector Workshop (NSS/MIC/RTSD)*, pages 1–2, 2016.
- [4] Hannu-Pekka Komsa, Simon Kurasch, Ossi Lehtinen, Ute Kaiser, and Arkady V Krasheninnikov. From point to extended defects in two-dimensional mos 2 : Evolution of atomic structure under electron irradiation. *PHYSICAL REVIEW B*, 88:35301, 2013.
- [5] Masson-Delmotte P. Zhai, H.-O. Pörtner. Summary for policymakers — global warming of 1.5 °c. *Intergovernmental Panel for Climate Change*, 2018.
- [6] Thomas Bowen, Ilya Chernyakhovskiy, and Paul Denholm. Grid-scale battery storage report. Technical report, U.S. National Renewable Energy Laboratory, 2019.
- [7] European Alternative Fuels Observatory. Country detail incentives | norway. Technical report, European Alternative Fuels Observatory, 2020.
- [8] Ping Li, Yibo Zhao, Yongxing Shen, and Shou-Hang Bo. Fracture behavior in battery materials. *J. Phys. Energy*, 2:22002, 2020.
- [9] A L Santhosha, Prasant Kumar Nayak, Kilian Pollok, Falko Langenhorst, and Philipp Adelhelm. Exfoliated mos 2 as electrode for all-solid-state rechargeable lithium-ion batteries. *Journal of Physical Chemistry*, 2019.
- [10] Jutta Heckenkamp and Gerd Jacobs. *MoS2*. Springer Berlin Heidelberg, 2014.
- [11] Tyler Stephenson, Zhi Li, Brian Olsen, and David Mitlin. Lithium ion battery applications of molybdenum disulfide (mos2) nanocomposites. *Energy Environ. Sci.*, 7:209–231, 2014.
- [12] Rana Eckhart, Mohamed El-Ashry, David Hales, Kirsty Hamilton, Peter Rae, and Michael Bariloche. Renewables global status report. Technical report, Renewables Now, 2019.

- [13] Marc Perez and Richard Perez. A fundamental look at supply side energy reserves for the planet. *IEA-SCHP Newsletter*, 62, 2015.
- [14] B. Radisavljevic, A. Radenovic, J. Brivio, V. Giacometti, and A. Kis. Single-layer mos₂ transistors. *Nature Nanotechnology*, 6:147–150, 2011.
- [15] Kin Fai Mak, Changgu Lee, James Hone, Jie Shan, and Tony F. Heinz. Atomically thin mos₂: A new direct-gap semiconductor. *Phys. Rev. Lett.*, 105:136805, 9 2010.
- [16] Marco Bernardi, Maurizia Palummo, and Jeffrey C Grossman. Extraordinary sunlight absorption and one nanometer thick photovoltaics using two-dimensional monolayer materials. *NanoLetters*, 2013.
- [17] Meng Lin Tsai, Sheng Han Su, Jan Kai Chang, Dung Sheng Tsai, Chang Hsiao Chen, Chih I. Wu, Lain Jong Li, Lih Juann Chen, and Jr Hau He. Monolayer mos₂ heterojunction solar cells. *ACS Nano*, 8:8317–8322, 2014.
- [18] Ranbir Singh, Anupam Giri, Monalisa Pal, Kaliannan Thiyagarajan, Junghyeok Kwak, Jae-Joon Lee, Unyong Jeong, and Kilwon Cho. Perovskite solar cells with an mos₂ electron transport layer †. *Journal of Materials Chemistry*, 2019.
- [19] Jiang Pu, Yohei Yomogida, Keng Ku Liu, Lain Jong Li, Yoshihiro Iwasa, and Taishi Takenobu. Highly flexible mos₂ thin-film transistors with ion gel dielectrics. *Nano Letters*, 12:4013–4017, 8 2012.
- [20] Hannu-Pekka Komsa, Jani Kotakoski, Simon Kurasch, Ossi Lehtinen, Ute Kaiser, and Arkady V. Krasheninnikov. Two-dimensional transition metal dichalcogenides under electron irradiation: defect production and doping. *Phys. Rev. Lett* 109, 035503, 2012.
- [21] Wu Zhou, Xiaolong Zou, Sina Najmaei, Zheng Liu, Yumeng Shi, Jing Kong, Jun Lou, Pulickel M. Ajayan, Boris I. Yakobson, and Juan Carlos Idrobo. Intrinsic structural defects in monolayer molybdenum disulfide. *Nano Letters*, 13:2615–2622, 6 2013.
- [22] Earl Kirkland. *Advanced Computing in Electron Microscopy Second Edition*. Springer, springer edition, 2010.
- [23] B. Schönfeld, J. J. Huang, and S. C. Moss. Anisotropic mean-square displacements (MSD) in single-crystals of 2H- and 3R-MoS₂. *Acta Crystallographica Section B*, 39(4):404–407, Aug 1983.
- [24] Brooke Melanie Lear. Scalable hrtem image simulation of molybdenum disulphide monolayers for machine learning dataset generation. Master’s thesis, University of Oxford, 2020.
- [25] Andrey N Enyashin, Maya Bar-Sadan, Lothar Houben, and Gotthard Seifert. Line defects in molybdenum disulfide layers. *Journal of Physical Chemistry*, 2013.
- [26] D. Liu, Y. Guo, L. Fang, and J. Robertson. Sulfur vacancies in monolayer mos₂ and its electrical contacts. *Applied Physics Letters*, 103:183113, 10 2013. describes n-type semiconducting nature of MoS₂ with S vacancies.

- [27] Sefaattin Tongay, Jian Zhou, Can Ataca, Jonathan Liu, Jeong Seuk Kang, Tyler S Matthews, Long You, Jingbo Li, Jeffrey C Grossman, and Junqiao Wu. Broad-range modulation of light emission in two-dimensional semiconductors by molecular physisorption gating. *Nano Letters*, 29:5, 2021.
- [28] Jinhua Hong, Zhixin Hu, Matt Probert, Kun Li, Danhui Lv, Xinan Yang, Lin Gu, Nannan Mao, Qingliang Feng, Liming Xie, Jin Zhang, Dianzhong Wu, Zhiyong Zhang, Chuanhong Jin, Wei Ji, Xixiang Zhang, Jun Yuan, and Ze Zhang. Exploring atomic defects in molybdenum disulphide monolayers. *Nature Communications*, 2015.
- [29] Martin Amani, Der Hsien Lien, Daisuke Kiriya, Jun Xiao, Angelica Azcatl, Jiyoung Noh, Surabhi R. Madhvapathy, Rafik Addou, K. C. Santosh, Madan Dubey, Kyeongjae Cho, Robert M. Wallace, Si Chen Lee, Jr Hau He, Joel W. Ager, Xiang Zhang, Eli Yablonovitch, and Ali Javey. Near-unity photoluminescence quantum yield in mos2. *Science*, 350:1065–1068, 11 2015.
- [30] Gonglan Ye, Yongji Gong, Junhao Lin, Bo Li, Yongmin He, Sokrates T Pantelides, Wu Zhou, Robert Vajtai, and Pulickel M Ajayan. Defects engineered monolayer mos 2 for improved hydrogen evolution reaction. *ACS Nano*, 2016.
- [31] Zuyun He, Ran Zhao, Xiaofei Chen, Huijun Chen, Yunmin Zhu, Huimin Su, Shengxi Huang, Jianming Xue, Junfeng Dai, Shuang Cheng, Meilin Liu, Xinwei Wang, and Yan Chen. Defect engineering in single-layer mos 2 using heavy ion irradiation. *ACS Applied Materials and Interfaces*, 10:42524–42533, 12 2018.
- [32] Alex W Robertson, Christopher S Allen, Yimin A Wu, Kuang He, Jaco Olivier, Jan Neethling, Angus I Kirkland, and Jamie H Warner. Spatial control of defect creation in graphene at the nanoscale. *Nature Communications*, 2012.
- [33] C.B. Carter and D.Williams. *Transmission Electron Microscopy A Textbook for Materials Science*. Springer, 2009.
- [34] Kai Nordlund, Steven J. Zinkle, Andrea E. Sand, Fredric Granberg, Robert S. Averback, Roger E. Stoller, Tomoaki Suzudo, Lorenzo Malerba, Florian Banhart, William J. Weber, Francois Willaime, Sergei L. Dudarev, and David Simeone. Primary radiation damage: A review of current understanding and models. *Journal of Nuclear Materials*, 512:450–479, 12 2018.
- [35] R.F. Egerton, P. Li, and M. Malac. Radiation damage in the tem and sem. *Micron*, 35(6):399–409, 2004.
- [36] Xin Chen, Peter Denninger, Tanja Stimpel-Lindner, Erdmann Spiecker, Georg S. Duesberg, Claudia Backes, Kathrin C. Knirsch, and Andreas Hirsch. Defect engineering of two-dimensional molybdenum disulfide. *Chemistry - A European Journal*, 5 2020.
- [37] Seung Hyun Song, Min Kyu Joo, Michael Neumann, Hyun Kim, and Young Hee Lee. Probing defect dynamics in monolayer mos2 via noise nanospectroscopy. *Nature Communications*, 8:1–6, 12 2017.
- [38] Qu Chen, Huashan Li, Si Zhou, Wenshuo Xu, Jun Chen, Hidetaka Sawada, Christopher S Allen, Angus I Kirkland, Jeffrey C Grossman, and Jamie H Warner. Ultralong 1d vacancy channels for rapid atomic migration during 2d void formation in monolayer mos 2. *ACS Nano*, 2018.

- [39] Junhao Lin, Sokrates T. Pantelides, and Wu Zhou. Vacancy-induced formation and growth of inversion domains in transition-metal dichalcogenide monolayer. *ACS Nano*, 9:5189–5197, 5 2015.
- [40] Anne Marie Z. Tan, Christoph Freysoldt, and Richard G. Hennig. Stability of charged sulfur vacancies in 2d and bulk mos_2 from plane-wave density functional theory with electrostatic corrections. *Phys. Rev. Materials*, 4:064004, Jun 2020.
- [41] Shanshan Wang, Gun Do Lee, Sungwoo Lee, Euijoon Yoon, and Jamie H. Warner. Detailed atomic reconstruction of extended line defects in monolayer mos_2 . *ACS Nano*, 10:5419–5430, 5 2016.
- [42] David J. Smith. *High Resolution Transmission Electron Microscopy*, pages 427–453. Springer US, 2005.
- [43] M Knoll and E Ruska. Das elektronenmikroskop. *Zeitschrift fur Physik*, 78, pages 318–339, 1932.
- [44] JEOL. *Transmission Electron Microscope (TEM) / Introduction to JEOL Products / JEOL Ltd.*
- [45] Brent Fultz and James M. Howe. *High-Resolution STEM Imaging: Transmission Electron Microscopy and Diffractometry of Materials*. Springer Berlin Heidelberg, 2008.
- [46] Angus I. Kirkland, Shery L.Y. Chang, and John L. Hutchison. *Atomic Resolution Transmission Electron Microscopy: Springer Handbook of Microscopy*. Springer, 2019.
- [47] O. Scherzer. Uber einige fehler von elektronenlinsen. *Z. Physik* 101, pages 593–603, 1936.
- [48] C Kisielowski, B Freitag, M Bischoff, and H Van Lin. Detection of single atoms and buried defects in three dimensions by aberration-corrected electron microscope with 0.5-Å information limit. *Microscopy and Microanalysis*, 2008.
- [49] Peter Nellist. Lecture 2: Conventional microscopes, microstructural characterisation course of materials for undergraduates, oxford university, 2018.
- [50] K. Ishizuka and N. Uyeda. A new theoretical and practical approach to the multislice method. *Acta Crystallographica Section A*, 33:740–749, 1977.
- [51] J. M. Cowley and A. F. Moodie. The scattering of electrons by atoms and crystals. i. a new theoretical approach. *Acta Crystallographica*, 10:609–619, 1957.
- [52] P. Goodman and A. F. Moodie. Numerical evaluations of n-beam wave functions in electron scattering by the multi-slice method. *Acta Crystallographica Section A*, 30(2):280–290, 1974.
- [53] I. Lobato and D. Van Dyck. Multem: A new multislice program to perform accurate and fast electron diffraction and imaging simulations using graphics processing units with cuda. *Ultramicroscopy*, 156:9–17, 2015.
- [54] I.Lobato, S.Van Aert, and J.Verbeeck. Progress and new advances in simulating electron microscopy datasets using multem. *Ultramicroscopy*, 168:17–27, 2016.

- [55] Yougui Liao. Practical electron microscopy and database. *An Online Book*, 2006.
- [56] Ian Goodfellow, Yoshua Bengio, and Aaron Courville. *Deep Learning*. MIT Press, 2016.
- [57] Stuart Russell and Peter Norvig. *Artificial Intelligence: A Modern Approach*. Prentice Hall Press, USA, 3rd edition, 2009.
- [58] Wolfgang Ertel. *Undergraduate Topics in Computer Science Introduction to Artificial Intelligence*. Springer Books, 2017.
- [59] Yu Liu. Feature extraction and image recognition with convolutional neural networks. *Journal of Physics: Conference Series*, 1087:062032, 09 2018.
- [60] Stanford Univeristy Fei Fei Li. *Convolutional Neural Networks: CS231n Convolutional Neural Networks for Visual Recognition*, accessed 13/06/2020. <https://cs231n.github.io/convolutional-networks/>.
- [61] Rokas Balsys. *Convolutional Neural Networks (CNN) explained*, accessed 09/06/2020. <https://pylessons.com/CNN-tutorial-introduction/>.
- [62] Karen Simonyan and Andrew Zisserman. Very deep convolutional networks for large-scale image recognition. *arXiv*, abs/1409.1556, 2014.
- [63] Alex Krizhevsky, Ilya Sutskever, and Geoffrey E. Hinton. Imagenet classification with deep convolutional neural networks. *Commun. ACM*, 60(6):84–90, 2012.
- [64] Shervin Minaee, Yuri Boykov, Fatih Murat Porikli, Antonio J. Plaza, Nasser Kehtarnavaz, and Demetri Terzopoulos. Image segmentation using deep learning: A survey. *ArXiv*, abs/2001.05566, 2020.
- [65] Md. Zahangir Alom, Tarek Taha, Chris Yakopcic, Stefan Westberg, Paheding Sidike, Mst Nasrin, Mahmudul Hasan, Brian Essen, Abdul Awwal, and Vijayan Asari. A state-of-the-art survey on deep learning theory and architectures. *Electronics*, 8:292, 03 2019.
- [66] Kurt Hornik, Maxwell Stinchcombe, and Halbert White. Multilayer feedforward networks are universal approximators. *Neural Networks*, 2(5):359 – 366, 1989.
- [67] Jacob Madsen, Pei Liu, Jens Kling, Jakob Birkedal Wagner, Thomas Willum Hansen, Ole Winther, and Jakob Schiotz. A deep learning approach to identify local structures in atomic-resolution transmission electron microscopy images. *Advanced Theory and Simulations*, 1, 2018.
- [68] Olaf Ronneberger, Philipp Fischer, and Thomas Brox. U-net: Convolutional networks for biomedical image segmentation. *Medical Image Computing and Computer-Assisted Intervention*, 9351, 2015.
- [69] Mohammad Hadi Modarres, Rossella Aversa, Stefano Cozzini, Regina Ciano, Angelo Leto, and Giuseppe Piero Brandino. Neural network for nanoscience scanning electron microscope image recognition. *Scientific Reports*, 7, 2017.

- [70] Maxim Ziatdinov, Ondrej Dyck, Artem Maksov, Xufan Li, Xiahan Sang, Kai Xiao, Raymond R. Unocic, Rama Vasudevan, Stephen Jesse, and Sergei V. Kalinin. Deep learning of atomically resolved scanning transmission electron microscopy images: Chemical identification and tracking local transformations. *ACS Nano*, 11:12742–12752, 12 2017.
- [71] Yu Saito, Kento Shin, Kei Terayama, Shaan Desai, Masaru Onga, Yuji Nakagawa, Yuki M. Itahashi, Yoshihiro Iwasa, Makoto Yamada, and Koji Tsuda. Deep-learning-based quality filtering of mechanically exfoliated 2d crystals. *npj Computational Materials*, 5:1–6, 12 2019.
- [72] Catherine K. Groschner, Christina Choi, and Mary C. Scott. Machine learning pipeline for segmentation and defect identification from high-resolution transmission electron microscopy data. *Microscopy and Microanalysis*, page 1–8, 2021.
- [73] Xiaoyang Zhu, Zuoheng Zhang, Yu Mao, Yan Li, Xiao Huang, and Ning Gu. Applying deep learning in automatic and rapid measurement of lattice spacings in hrtem images. *Sci China Mater*, pages 2365–2370, 2020.
- [74] Jakob Schiotz, Jacob Madsen, Bjarke J. G. Ostergaard, Anders S. Dreisig, Pei Liu, Stig Helveg, Ole Winther, Jens Kling, Jakob Birkedal Wagner, and Thomas Willum Hansen. Using neural networks to identify atoms in hrtem images. *Microscopy and Microanalysis*, 25:216–217, 2019.
- [75] Martín Abadi, Ashish Agarwal, Paul Barham, Eugene Brevdo, and Zhifeng Chen. TensorFlow: Large-scale machine learning on heterogeneous systems, 2015. Software available from tensorflow.org.
- [76] Richard O. Duda and Peter E. Hart. Use of the hough transformation to detect lines and curves in pictures. *Communications of the ACM*, 15:11–15, 1 1972.
- [77] Pilar Bachiller-Burgos, Luis J. Manso, and Pablo Bustos. A variant of the hough transform for the combined detection of corners, segments, and polylines. *Eurasip Journal on Image and Video Processing*, 2017:32, 12 2017.
- [78] Renliang Yuan, Jiong Zhang, and Jian Min Zuo. Lattice strain mapping using circular hough transform for electron diffraction disk detection. *Ultra-microscopy*, 207:112837, 12 2019.
- [79] G Elizabeth Rani, R Murugeswari, and N Rajini. Edge detection in scanning electron microscope (sem) images using various algorithms. In *2020 4th International Conference on Intelligent Computing and Control Systems (ICICCS)*, pages 401–405, 2020.
- [80] J.P. Jakubovics. Treatment of experimental errors: Oxford materials science part ii course handbook. Technical report, University of Oxford, 2019.
- [81] Hannu-Pekka Komsa, Jani Kotakoski, Simon Kurasch, Ossi Lehtinen, Ute Kaiser, and Arkady V. Krashenninnikov. Two-dimensional transition metal dichalcogenides under electron irradiation: Defect production and doping. *Phys. Rev. Lett.*, 109:035503, Jul 2012.
- [82] Tom Ellaby, Aakash Varambhia, Xiaonan Luo, Ludovic Briquet, Misbah Sarwar, Dogan Ozkaya, David Thompsett, Peter D Nellist, and Chris-Kriton Skylaris. Strain effects in core-shell ptco nanoparticles: a comparison of experimental observations and computational modelling. *Phys. Chem. Chem. Phys.*, 22:24784, 2020.

- [83] Hannu-Pekka Komsa and Arkady V. Krashennnikov. Native defects in bulk and monolayer MoS₂ from first principles. *Physical Review B - Condensed Matter and Materials Physics*, 2015.
- [84] Jamie H. Warner, Elena Roxana Margine, Masaki Mukai, Alexander W. Robertson, Feliciano Giustino, and Angus I. Kirkland. Dislocation-driven deformations in graphene. *Science*, 337:209–212, 7 2012.
- [85] Jin-Wu Jiang. Graphene versus mos 2 : A short review. *Front. Phys*, 10:106801, 2015.
- [86] Le Huang, Zhanghui Chen, and Jingbo Li. Effects of strain on the band gap and effective mass in two-dimensional monolayer gax (x = s, se, te). *RSC Adv.*, 2015.
- [87] Jun Chen, Si Zhou, Yi Wen, Gyeong Hee Ryu, Christopher Allen, Yang Lu, Angus I. Kirkland, and Jamie H. Warner. In situ high temperature atomic level dynamics of large inversion domain formations in monolayer mos2. *Nanoscale*, 11:1901–1913, 1 2019.
- [88] Qiu Jin, Ning Liu, Biaohua Chen, and Donghai Mei. Mechanisms of semiconducting 2h to metallic 1t phase transition in two-dimensional mos 2 nanosheets. *Journal of Physical Chemistry C*, 122:28215–28224, 12 2018.
- [89] Gyeong Hee Ryu, Jongyeong Lee, Na Yeon Kim, Yeongdong Lee, Youngchan Kim, Moon J. Kim, Changgu Lee, and Zonghoon Lee. Line-defect mediated formation of hole and mo clusters in monolayer molybdenum disulfide. *2D Materials*, 3, 1 2016.
- [90] Shanshan Wang, Huashan Li, Hidetaka Sawada, Christopher S. Allen, Angus I. Kirkland, Jeffrey C. Grossman, and Jamie H. Warner. Atomic structure and formation mechanism of sub-nanometer pores in 2d monolayer mos2. *Nanoscale*, 9:6417–6426, 5 2017.
- [91] Aaron C. Johnston-Peck, Joseph S. DuChene, Alan D. Roberts, Wei David Wei, and Andrew A. Herzing. Dose-rate-dependent damage of cerium dioxide in the scanning transmission electron microscope. *Ultramicroscopy*, 170:1–9, 11 2016.
- [92] Chong Wang and Yi-Hong Ding. Catalytically healing the stone-wales defects in graphene by carbon adatoms. *Journal of Materials Chemistry A*, 2012.
- [93] Oriol Lopez-Sanchez, Dominik Lembke, Metin Kayci, Aleksandra Radenovic, and Andras Kis. Ultrasensitive photodetectors based on monolayer mos. *Nature Nanotechnology*, 8:497–501, 6 2013.
- [94] US Geological Survey. Mineral commodity summaries. Technical report, US Geological Survey, 2021.
- [95] Business and Human Rights Investment Trackers. Transition minerals.
- [96] Qiaobao Zhang, Huixin Chen, Yunhua Xu, Wei Sun, and Xiaobo Ji. Size-tunable natural mineral-molybdenite for lithium-ion batteries toward: Enhanced storage capacity and quicken ions transferring. *Frontiers in Chemistry*, 1:389, 2018.
- [97] Alexander Sutulov and Tsin Chun. Molybdenum processing, 2018.

- [98] K. S. Novoselov, D. Jiang, F. Schedin, T. J. Booth, V. V. Khotkevich, S. V. Morozov, and A. K. Geim. Two-dimensional atomic crystals. *Proceedings of the National Academy of Sciences of the United States of America*, 102:10451–10453, 7 2005.
- [99] Dai-Ming Tang, Dmitry G Kvashnin, Sina Najmaei, Yoshio Bando, Koji Kimoto, Pekka Koskinen, Pulickel M Ajayan, Boris I Yakobson, Pavel B Sorokin, Jun Lou, and Dmitri Golberg. Nanomechanical cleavage of molybdenum disulphide atomic layers. *Nature Communications*, 2014.
- [100] Fraunhofer Institute. Photovoltaics report. Technical report, Fraunhofer Institute for Solar Energy Systems, 2020.
- [101] Antonio Di Bartolomeo. Graphene schottky diodes: An experimental review of the rectifying graphene/semiconductor heterojunction. *Physics Reports*, 606:1–58, 1 2016.
- [102] Amy Galland. Best practices in photovoltaics report. Technical report, Centre for Life Cycle Analysis.
- [103] International Renewable Energy Agency. End-of-life management: Solar photovoltaic panels, 2016.
- [104] Data centre cooling technologies and best practices | digital realty.
- [105] Centre for Alternative Technology. Photovoltaic solar panels, 2021.
- [106] Emma Strubell, Ananya Ganesh, and Andrew McCallum. Energy and policy considerations for deep learning in NLP. In *Proceedings of the 57th Annual Meeting of the Association for Computational Linguistics*, pages 3645–3650, Florence, Italy, July 2019. Association for Computational Linguistics.
- [107] Eu press release: Europe fit for the digital age: Artificial intelligence, 4 2021.
- [108] Boris Johnson. Prime minister’s statement on coronavirus (covid-19): 23 march 2020 - gov.uk, 2020.
- [109] Health and Safety Executive Report. *Health and Safety Executive Exercises to reduce musculoskeletal discomfort for people doing a range of static and repetitive work*, 2011.